

2 min



N79-13503

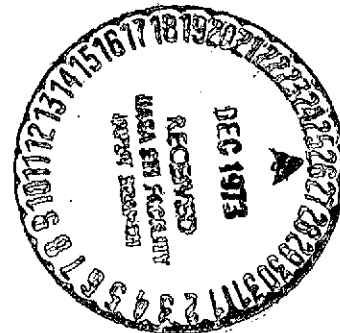
(NASA-CR-134532) HOLLOW CATHODE  
RESTARTABLE 15 CM DIAMETER ION THRUSTER  
Annual Report, 1 Dec. 1972 - 1 Dec.  
1973 (Colorado State Univ.) ~~104~~ p HC  
\$7.25

Unclas  
23706  
CSCL 21C G3/28

HOLLOW CATHODE RESTARTABLE  
15 CM DIAMETER ION THRUSTER

PREPARED FOR  
LEWIS RESEARCH CENTER  
NATIONAL AERONAUTICS AND SPACE ADMINISTRATION

GRANT NGR-06-002-112



Annual Report

December 1973

Paul J. Wilbur  
Department of Mechanical Engineering  
Colorado State University  
Fort Collins, Colorado

1. Report No. NASA CR-134532		2. Government Accession No.		3. Recipient's Catalog No.	
4. Title and Subtitle Hollow Cathode Restartable 15 cm Diameter Ion Thruster				5. Report Date December 1973	
				6. Performing Organization Code	
7. Author(s) Paul J. Wilbur				8. Performing Organization Report No.	
9. Performing Organization Name and Address Department of Mechanical Engineering Colorado State University Fort Collins, Colorado 80521				10. Work Unit No.	
				11. Contract or Grant No. NGR-06-002-112	
12. Sponsoring Agency Name and Address National Aeronautics and Space Administration Washington, D. C. 20546				13. Type of Report and Period Covered Contractor Report Dec. 1, 1972 - Dec. 1, 1973	
				14. Sponsoring Agency Code	
15. Supplementary Notes Grant Monitor, William Kerslake Spacecraft Technology Div. NASA Lewis Research Center Cleveland, Ohio 44135					
16. Abstract The effects of substituting high perveance dished grids for low perveance flat ones on performance variables and plasma properties within a 15 cm modified SERT II thruster are discussed. Results suggest good performance may be achieved as an ion thruster is throttled if the screen grid transparency is decreased with propellant flow rate. Thruster startup tests, which employ a pulsed high voltage tickler electrode between the keeper and the cathode to initiate the discharge, are described. High startup reliability at cathode tip temperatures of about 500°C without excessive component wear over 2000 startup cycles is demonstrated. Testing of a single cusp magnetic field concept of discharge plasma containment is discussed. A theory which explains the observed behavior of the device is presented and proposed thruster modifications and future testing plans are discussed. The theory of Penning ionization of mercury atoms is discussed and supporting experimental data are presented which suggest this is not a viable method to produce mercury ions for a thruster. A theoretical model describing the production of doubly ionized mercury in thrusters is presented. Results show the bulk of these ions are produced via a two step reaction and that both Maxwellian and primary electron ionizations contribute significantly. Experimental mercury flow measurement results obtained with a thermal flow meter in the feed line to a thruster are described.					
17. Key Words (Suggested by Author(s)) Electrostatic Thruster			18. Distribution Statement Unclassified - Unlimited		
19. Security Classif. (of this report) Unclassified		20. Security Classif. (of this page) Unclassified		21. No. of Pages 100	22. Price* \$3.00

\* For sale by the National Technical Information Service, Springfield, Virginia 22151

## TABLE OF CONTENTS

Title	Page
Abstract . . . . .	i
15 cm Thruster Performance Testing. . . . .	1
Apparatus . . . . .	1
Performance . . . . .	1
Plasma Property Contours . . . . .	5
Conclusion . . . . .	12
Pulsed Ignition Startup Studies . . . . .	13
Introduction . . . . .	13
Apparatus . . . . .	13
Repetitive Startup Cycle Test Results . . . . .	16
Rapid Startup Study . . . . .	24
Conclusion . . . . .	26
Single Cusp Magnetic Field Thruster . . . . .	27
Introduction . . . . .	27
Apparatus . . . . .	30
Anode Configuration Experiments . . . . .	35
Throttling Experiments . . . . .	39
Variable Magnetic Baffle Effects . . . . .	43
Cathode Flow Rate Effects . . . . .	43
Performance Comparison with SERT II Discharge Chamber. . . . .	47
Discharge Chamber Theory . . . . .	49
Ion Beam Profile Theory . . . . .	53
The Effect of Double Ions on Performance Data . . . . .	53
The Effects of Reducing the Thruster Length . . . . .	57
Conclusion . . . . .	57
The Penning Ionization Mechanism in an Electron- Bombardment Ion Thruster . . . . .	59
Introduction . . . . .	59
Theory . . . . .	59
Experiment . . . . .	66
Conclusion . . . . .	67

Title	Page
Double Ion Production in Mercury Electron- Bombardment Thrusters . . . . .	69
Introduction . . . . .	69
Theory . . . . .	69
Results . . . . .	72
Comparison with Experimental Results . . . . .	75
Thermal Flow Meter . . . . .	79
Introduction . . . . .	79
Theory of Operation . . . . .	79
Experimental Performance . . . . .	83
Appendix A - Ion Velocities toward Boundaries for Plasmas Containing Doubly Charged Ions . . . . .	89
References . . . . .	93
Distribution List . . . . .	96

## 15 CM THRUSTER PERFORMANCE TESTING

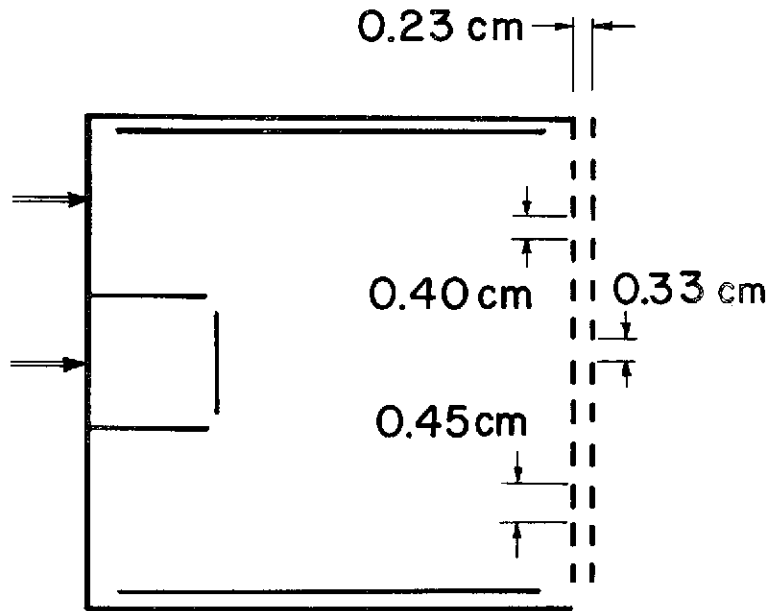
### Apparatus

A SERT II thruster<sup>1</sup> was modified to include independent main and hollow cathode flow control and measurement systems, electromagnets, a solid disc baffle, and a cathode with a 0.05 cm dia. orifice. A larger cathode orifice than the one used on SERT II (0.015 cm dia.) was required to facilitate sustained operations at the higher beam current conditions expected in these tests. Power supplies and Langmuir probes used in the testing are described in Reference 2. Tests were conducted on the thruster described above with both standard flat grids and dished grids over a range of total flow rate conditions to facilitate performance comparisons. The two grid sets used in the tests are characterized by the dimensions shown in Figure 1. The dished grids, which are both 0.046 cm thick, are seen to have 0.20 cm dia. apertures in both the accel and screen grids on 0.25 cm centers, to be separated by 0.079 cm and to be dished out 0.5 cm at their centers. The flat grid spacing on the other hand is 0.23 cm and the holes in the 0.15 cm thick accel grid are slightly smaller than those in the .074 cm thick screen grid. The open area fractions for the screen grids are comparable. In spite of the greater voltages applied to the flat grids, their greater separation and hence lesser perveance effects an overriding reduction in the Childs' law beam current density to 32% of that calculated for the dished grids. The effective ion acceleration distance used in this calculation of Childs' law current densities is that suggested by Rawlin<sup>3</sup> for 30 cm dished grids. Since the beam current at the nominal operating condition decreased from 650 ma for the dished grids to 240 ma for the flat ones (a ratio of 38%) the Rawlin expression appears to be valid for this smaller thruster too.

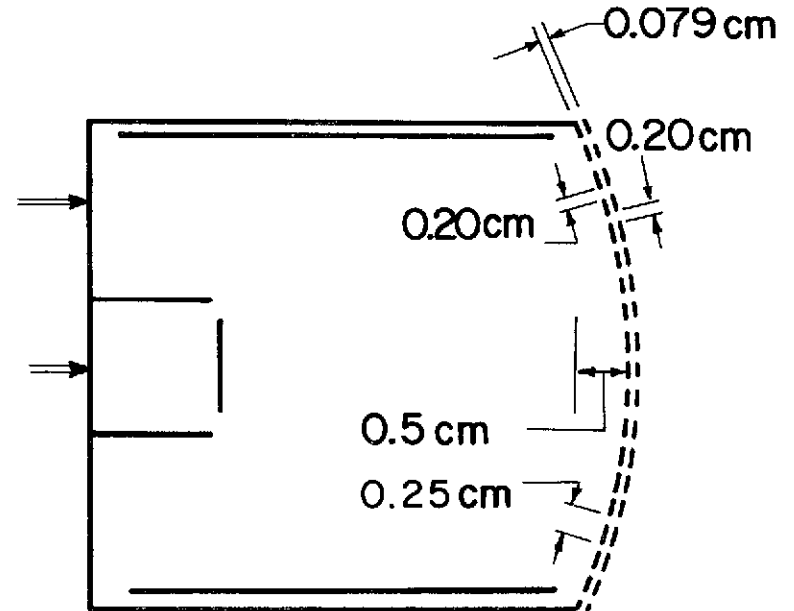
### Performance

The discharge losses (including keeper discharge losses) for the two grid systems are presented as a function of propellant utilization

THRUSTER GRID CONFIGURATIONS  
FIGURE 1



**FLAT GRIDS**  
71 % Open Area  
 $V_+ = 3000 \text{ v}$   
 $V_- = -1500 \text{ v}$

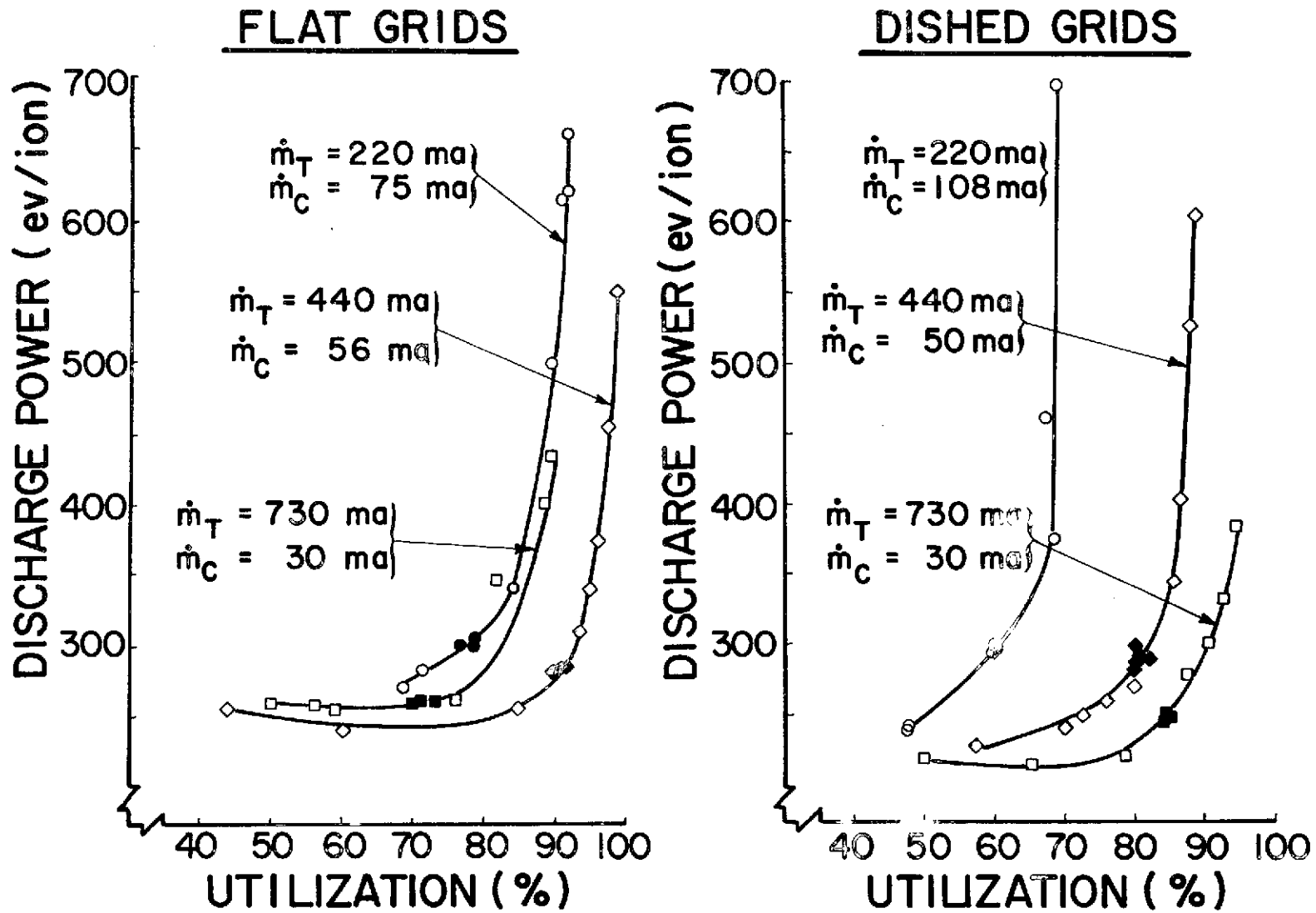


**DISHED GRIDS**  
67 % Open Area  
 $V_+ = 1000 \text{ v}$   
 $V_- = -500 \text{ v}$

efficiency in Figure 2 over a total mercury flow rate ( $\dot{m}_T$ ) range from 220 ma to 730 ma equivalent. The cathode flow rates ( $\dot{m}_C$ ), also indicated on this figure, were selected to produce an arc voltage in the range 36-37 v (designated by the solid symbols) near the knee of each performance curve. The data of Figure 2 obtained with the high perveance, dished grids show that the thruster exhibits a decrease in maximum utilization as the total flow rate is throttled from 730 ma through 440 ma to 220 ma as Kaufman's model for maximum utilization<sup>4</sup> predicts. With the flat grids however the maximum utilization is greatest at the 440 ma total flow condition. A decrease in maximum utilization was observed with the flat grids as the flow rate was increased above about 440 ma several times, and it became so severe in some instances that beam current actually decreased as flow rate was increased at essentially constant arc voltage and current conditions. Comparison of the data at 440 ma total flow for the two grid systems indicates flat grids yield superior performance at this lesser flow rate. This leads one to the conclusion that optimum thruster performance over a throttling range can be achieved by reducing the grid system transparency as flow rate is reduced. The transparency of a grid system is primarily a function of the screen grid open area fraction and the shape and location of the thruster plasma-beam plasma interface<sup>5</sup>, which are determined in turn by the effective ion acceleration distance. The screen grid open area fraction is not significantly different between the two grid sets, but the screen grid thickness and grid separation distance have been changed and they alter the effective ion acceleration distance. This suggests optimum thruster performance might be achieved by varying grid separation as the thruster is throttled, although tests have not been performed where grid separation alone is varied to achieve this optimum condition. The range of throttling suggested by the two sets of curves in Figure 2 is from a 175 ma beam current (80% utilization and 300 ev/ion) to 630 ma beam current (85% utilization and 250 ev/ion) - a 3.5 to 1 throttling range.

The ion beam profiles measured with a Faraday probe swept through the beam at a location 5 cm downstream of the accel grid are shown in

15 cm THRUSTER PERFORMANCE  
 FIGURE 2



Figures 3, 4 and 5. Integration of the current density profiles shown over the beam cross sectional area yields beam currents which agrees with the measured beam currents to within 5%. The parameter shown with each curve is the ratio of average to maximum beam current density appropriate to that curve shown. Since an  $\epsilon$  near unity is desirable, Figure 3 suggests the flat grids yield the better ion beam profile at the high flow rate. The parameter  $\epsilon$  is less for the dished grids because of the significant current densities at radii beyond 8 cm. This is a result of poor focus of some of the dished grid beamlets, due to grid hole misalignments - a condition that has since been corrected by redesign of the grids to compensate for the inherent misalignment which occurs when grids are dished.

Comparison of Figures 3, 4 and 5 suggests the ion beam profile becomes more peaked as the thruster is throttled and that this effect is most pronounced in the flat grid system. The tendency toward a more peaked profile as the thruster is throttled is considered to be due to the increased fraction of the propellant flow that is introduced through the cathode as it is throttled. This tends to cause an increase in neutral density near the center of the discharge chamber, hence greater ionization on the centerline and the more peaked profile.

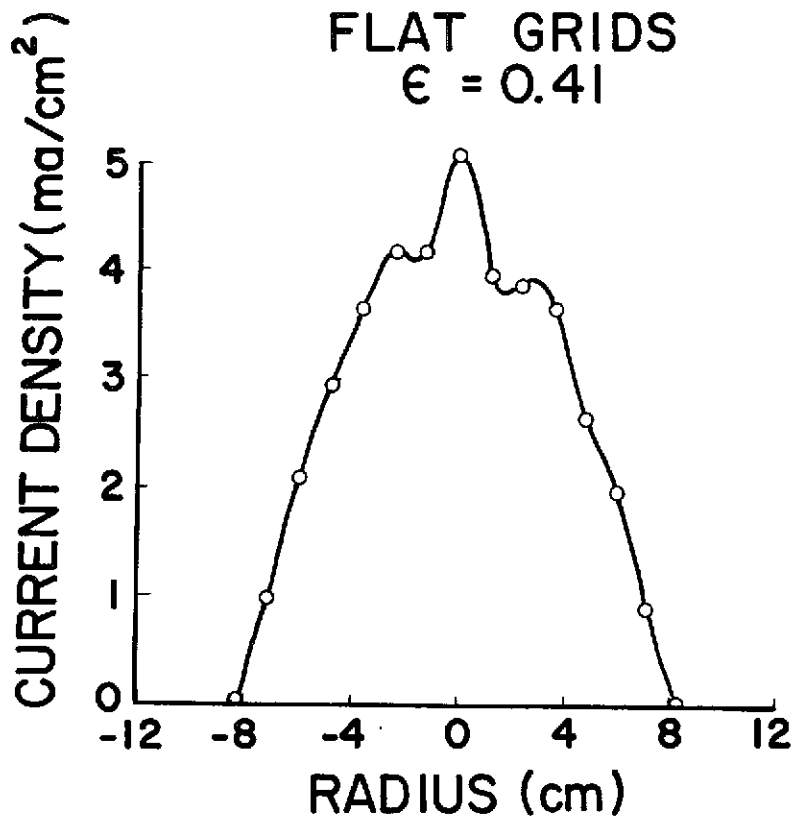
#### Plasma Property Contours

Figures 6, 7 and 8 present the electron temperature, plasma potential and primary and Maxwellian electron densities within the thruster over the range of flow rates investigated and at the 36-37 v operating conditions identified by the solid symbols on Figure 2. Each contour shows the variation of the indicated property on the surface of a plane passing from the thruster centerline to the anode over the length of the thruster. The cathode pole piece is identified by the line parallel to the thruster axis at the rear of each plot. The forwardmost line perpendicular to the thruster axis represents the plane of the anode pole piece. Measurements were made with a moveable Langmuir probe and the recording system

# ION BEAM PROFILES

$$\dot{m}_T = 730 \text{ ma}$$

FLAT GRIDS  
 $\epsilon = 0.41$



DISHED GRIDS  
 $\epsilon = 0.37$

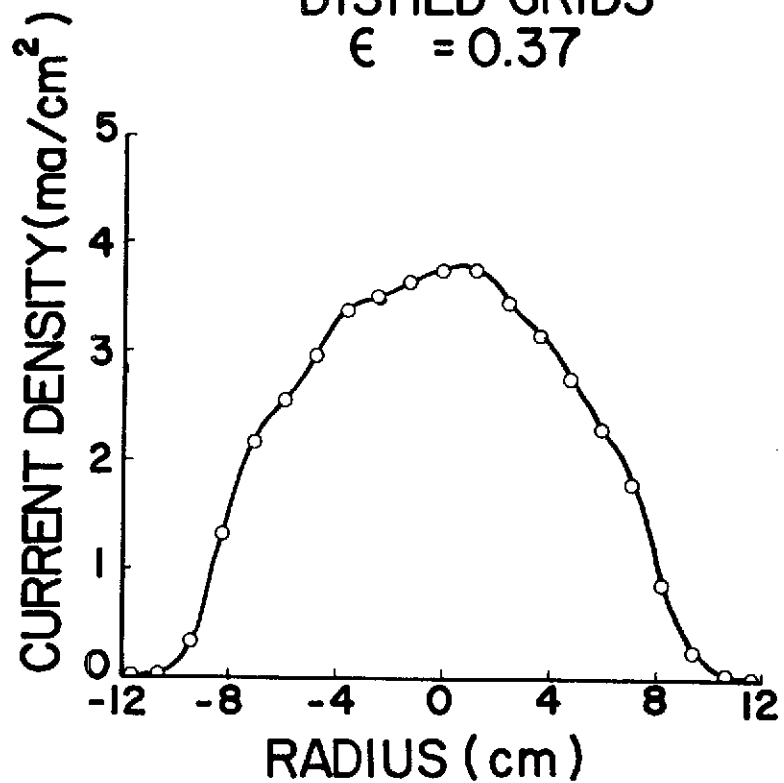
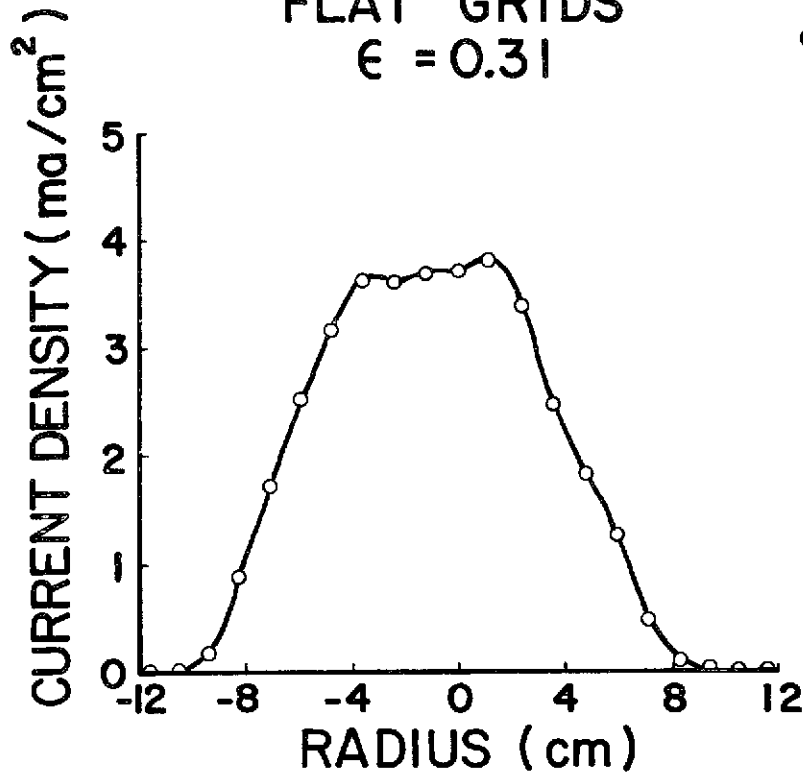


FIGURE 3  
HIGH FLOW RATE ION BEAM PROFILES

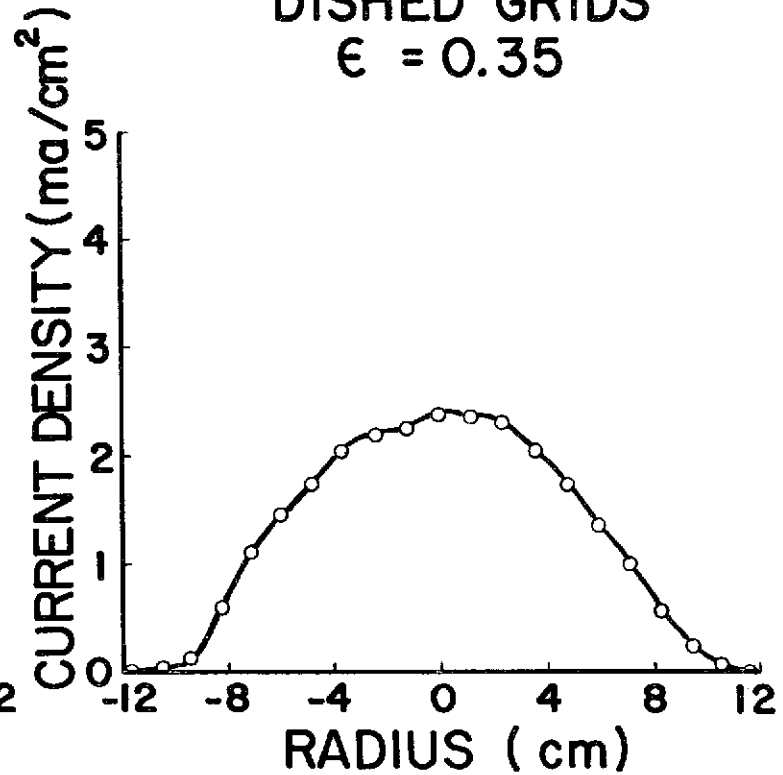
# ION BEAM PROFILES

$$\dot{m}_T = 440 \text{ ma}$$

FLAT GRIDS  
 $\epsilon = 0.31$



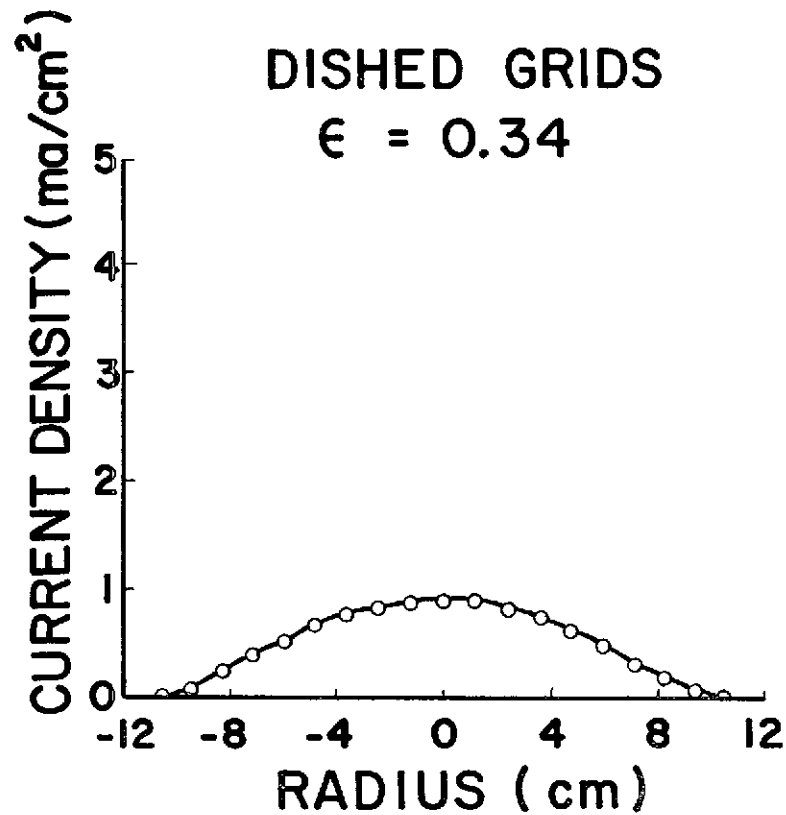
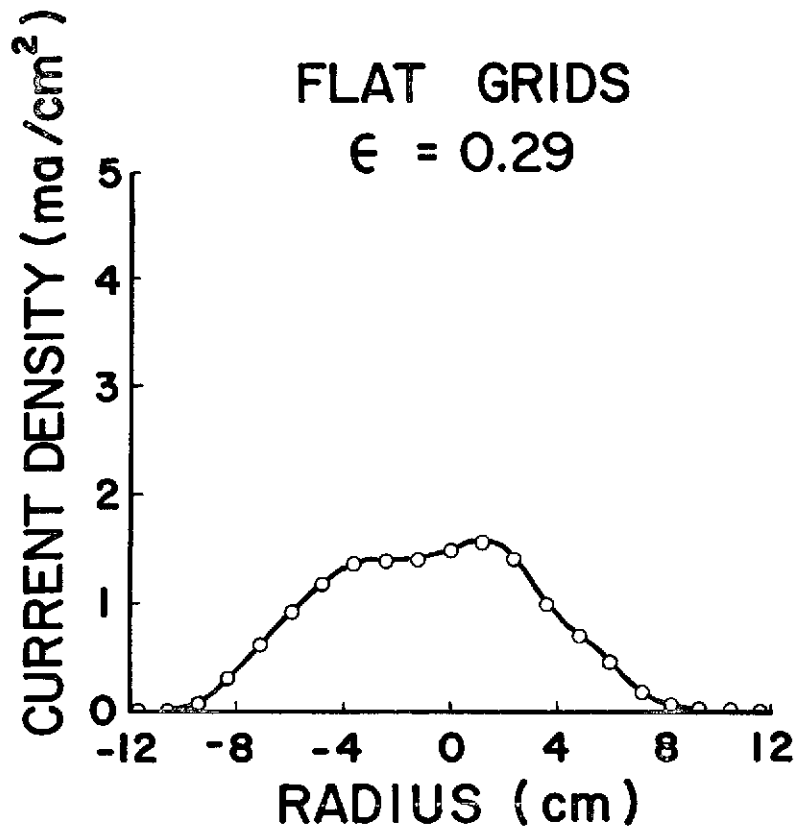
DISHED GRIDS  
 $\epsilon = 0.35$



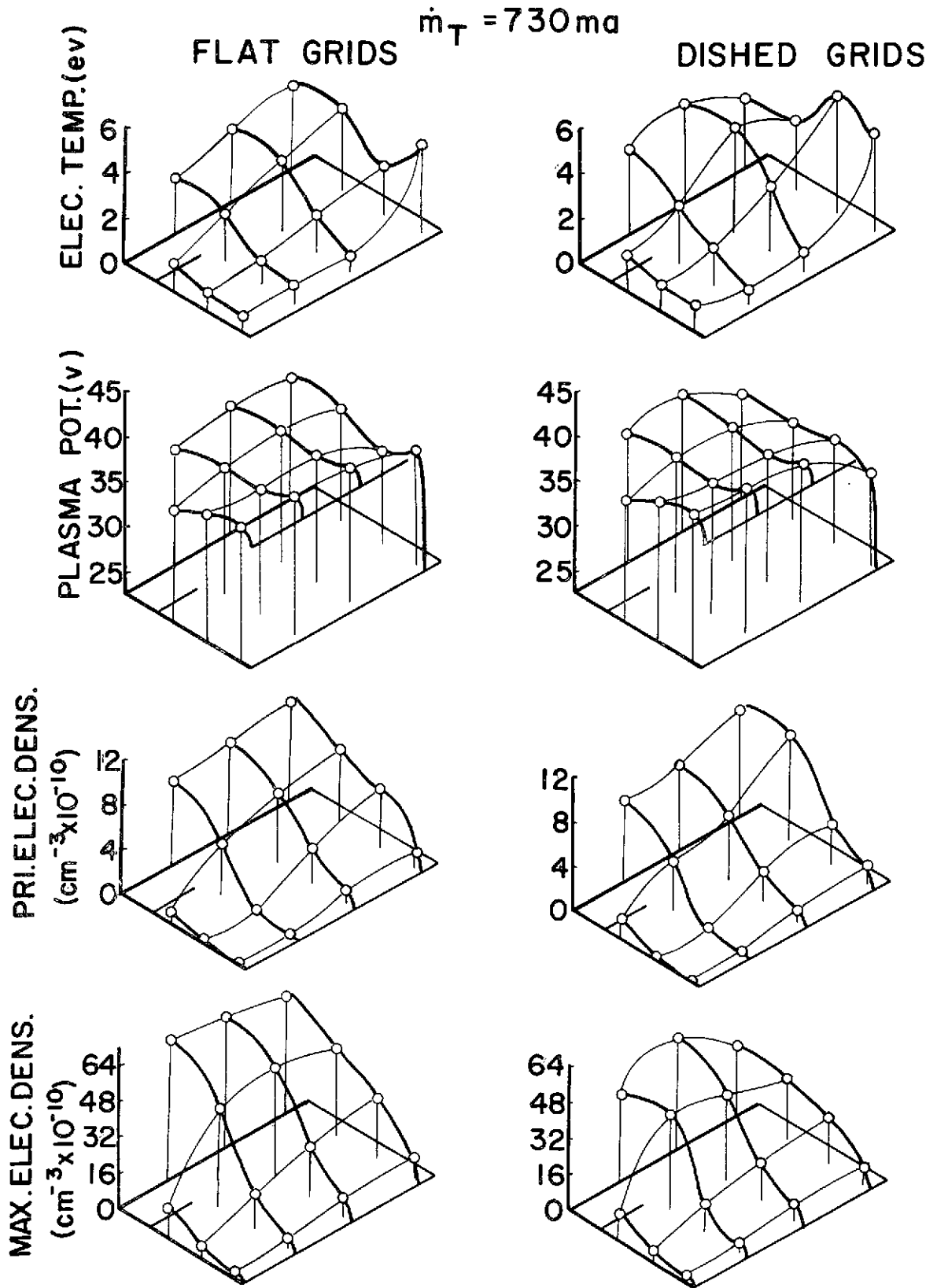
INTERMEDIATE FLOW RATE ION BEAM PROFILES  
FIGURE 4

# ION BEAM PROFILES

$$\dot{m}_T = 220 \text{ ma}$$



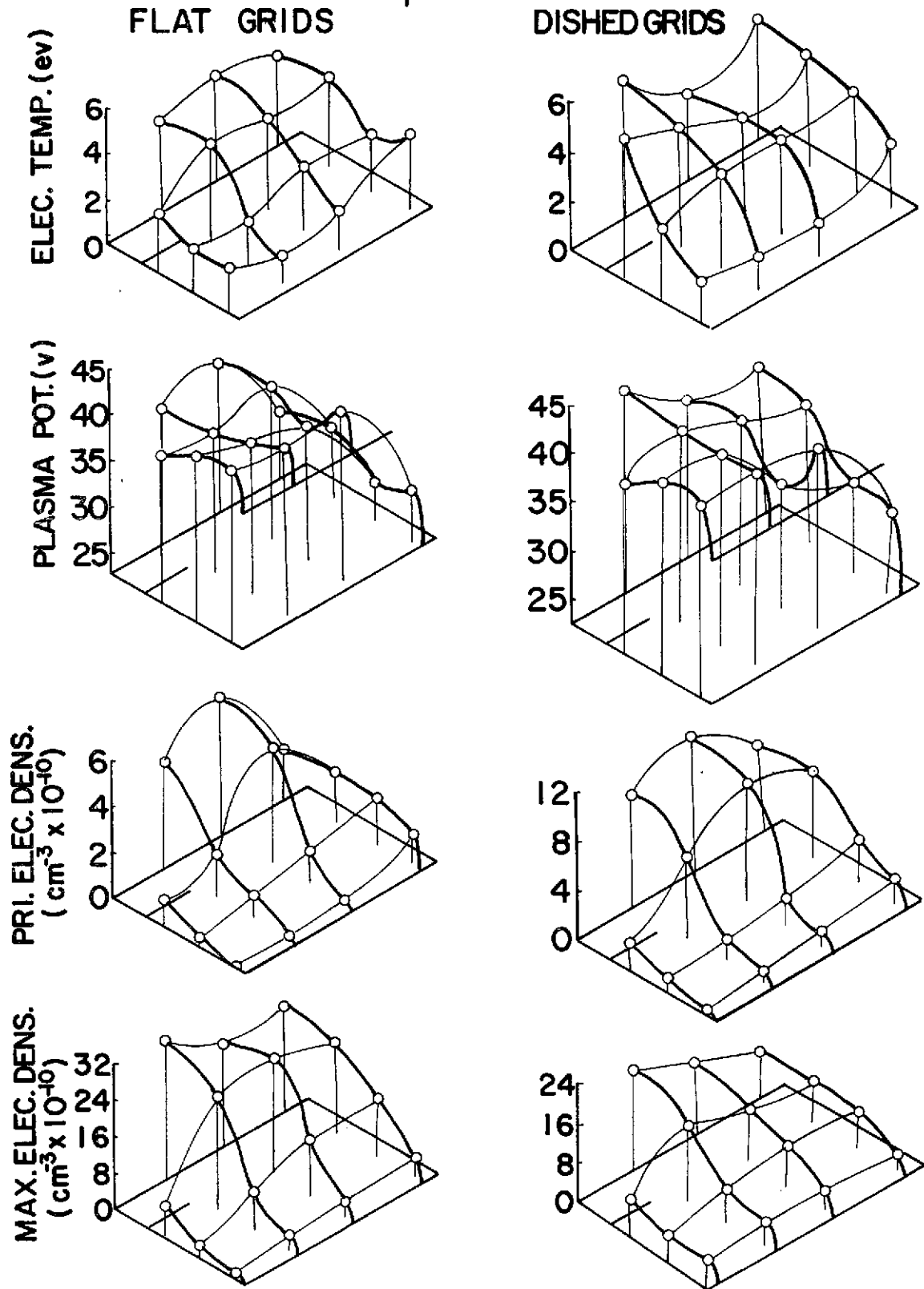
LOW FLOW RATE ION BEAM PROFILES  
FIGURE 5



HIGH FLOW RATE PLASMA PROPERTY CONTOUR

FIGURE 6

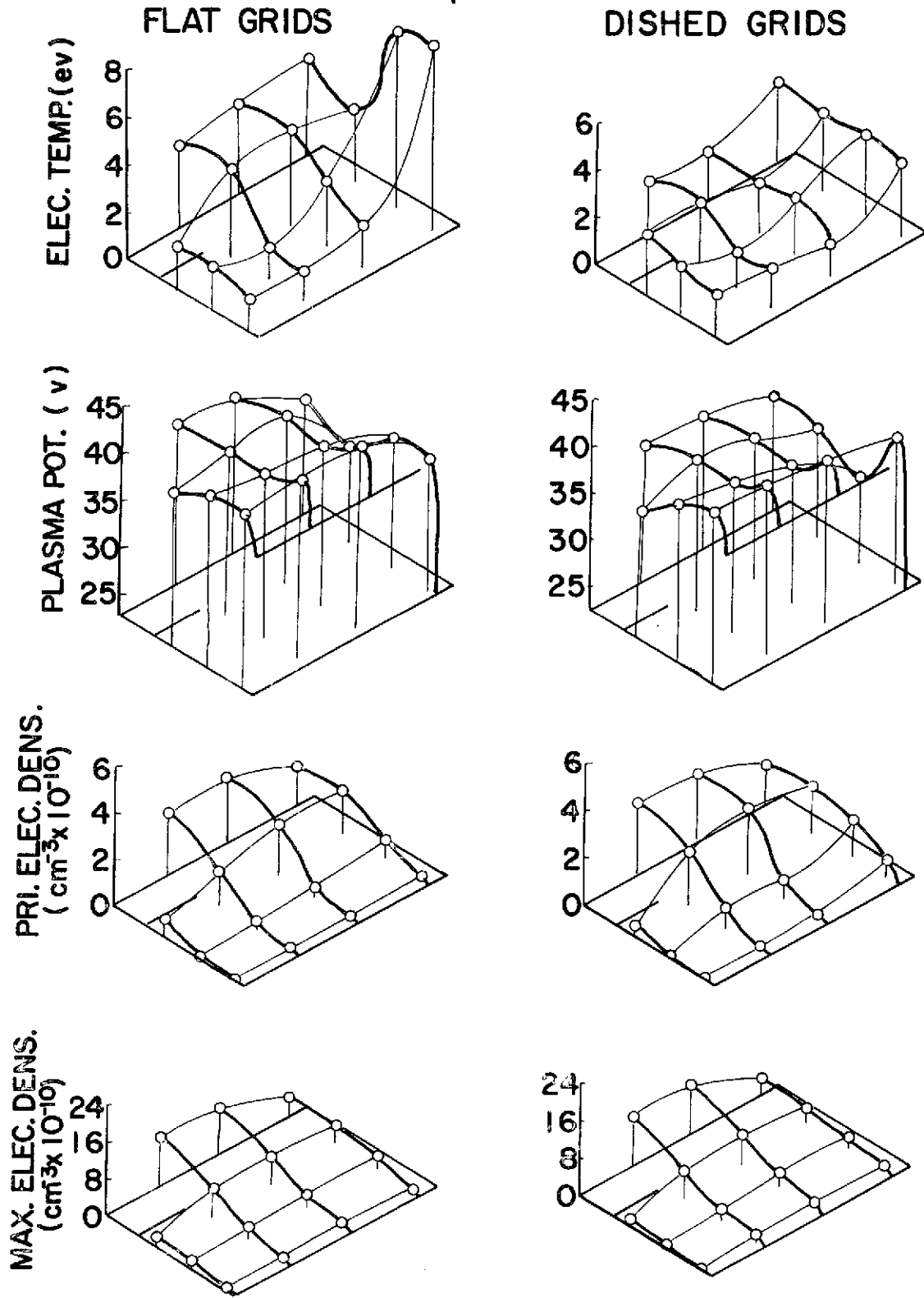
$\dot{m}_T = 440 \text{ ma}$



INTERMEDIATE FLOW RATE PLASMA PROPERTY CONTOUR

FIGURE 7

$\dot{m}_T = 220 \text{ ma}$



LOW FLOW RATE PLASMA PROPERTY CONTOUR

FIGURE 8

described in Reference 6. The raw data were analyzed using the method of Strickfaden and Geiler<sup>7</sup>.

Comparison of the data of Figures 6, 7 and 8 suggests the following:

1. Substitution of higher perveance dished grids for flat grids results in:
  - a. a reduction in Maxwellian electron density. This reduction was greatest at the 440 ma and least at the 220 ma flow conditions and most pronounced at each flow condition near the screen grid,
  - b. an increase in primary electron density. The increase was again greatest at the 440 ma flow condition and most pronounced at each flow near the screen grid, and
  - c. no variation in plasma potential or Maxwellian electron temperature that is considered significant.
2. Throttling the flow into the thruster results in:
  - a. a proportionate decrease in Maxwellian and primary electron densities throughout the discharge chamber.
  - b. a more pronounced plasma potential ridge at the anode, and
  - c. an increase in electron temperature near the screen grid which becomes significant at the lowest flows considered.

### Conclusions

Installation of high perveance dished grids makes it possible to operate a 15 cm diameter SERT II-type thruster at an ion beam current over 600 ma at 85% utilization and 250 ev/ion discharge power with a 1000 v net accelerating voltage. When the flow rate is throttled to obtain a 130 ma ion beam with the dished grids, propellant utilization and discharge power change to 60% and 300 ev/ion respectively. This degradation in performance with throttling can be reduced if the screen grid transparency is reduced with flow rate. Additional testing is required to determine if this variation in grid transparency can be achieved through variations in grid separation alone.

## PULSED IGNITION STARTUP STUDIES

### Introduction

Appreciable cost or weight savings can be achieved in synchronous orbit satellite systems if ion thrusters are used to produce the associated North-South stationkeeping requirement instead of a chemical propellant thruster<sup>8</sup>. For a typical synchronous communication satellite having a mass of 700 kg, the 46 m/sec annual North-South stationkeeping velocity increment can be met by a mercury ion thruster operating at a 600 ma beam current level and 1000 volt thruster potential on a duty cycle of 230 hours per year. Assuming 60% overall electrical efficiency, the thruster could satisfy this requirement by operating for 230 one hour intervals from a 1 kilowatt-hour battery which could be charged continuously from a small solar array (~ 30 watt output). For such a thruster system to perform effectively however it must be capable of repeated startup which is both rapid and reliable and be able to produce a 600 ma ion beam at 1000 volts thruster potential with acceptable propellant utilization and electrical efficiencies. Electron bombardment ion thruster startup has required resistance heating of the hollow cathode tip to a sufficiently high temperature to permit spontaneous ignition of the keeper discharge. This mode of startup is frequently unreliable because the cathode tip temperatures and the times which are required to start the discharge tend to vary with the history of the cathode. Application of a high voltage discharge system developed by Wintucky<sup>9</sup> to ignite the keeper discharge is proposed as a means of correcting this reliability deficiency.

### Apparatus

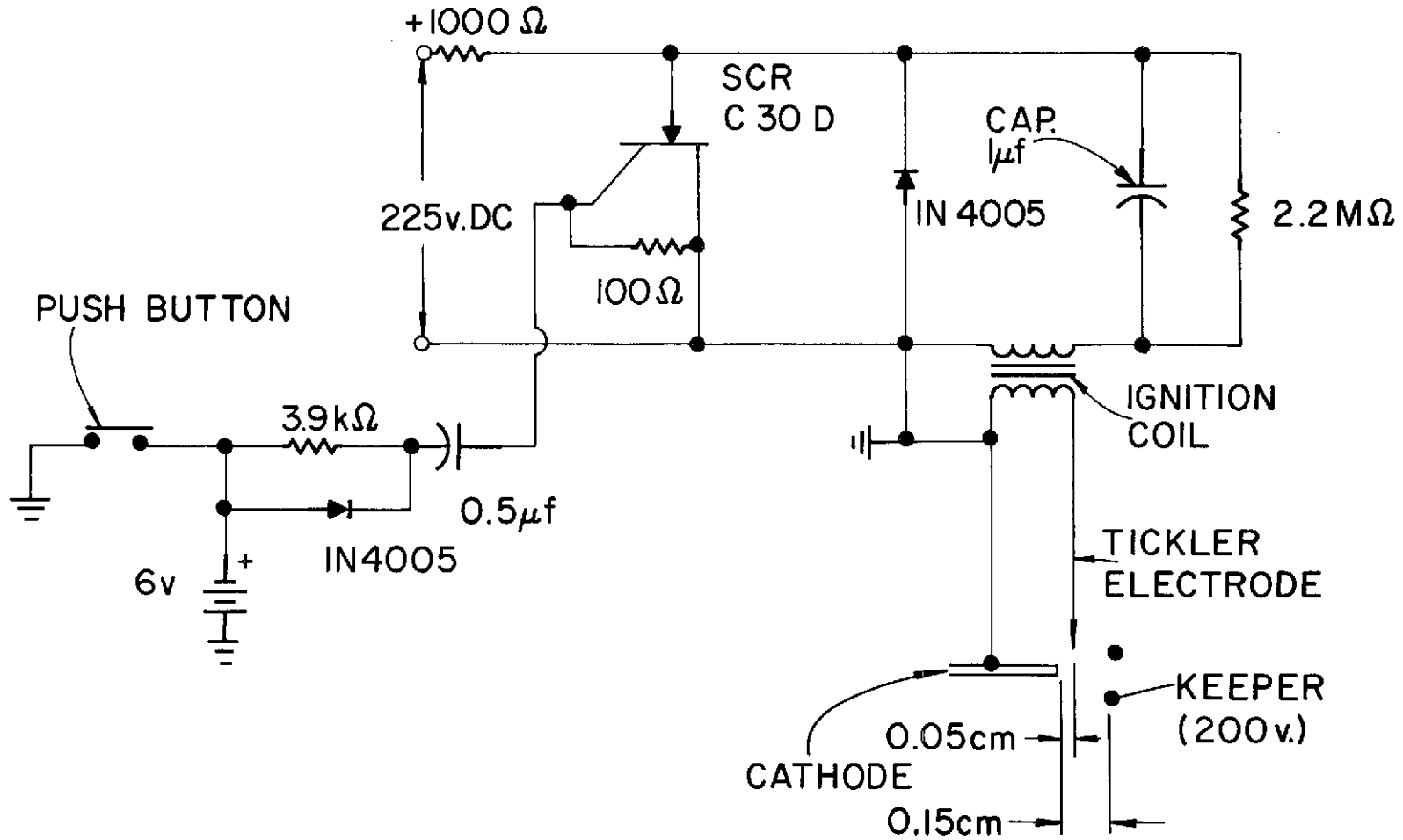
The 15 cm modified SERT II thruster with dished grids, shown in Figure 1 and discussed previously, can produce the 600 ma ion beam current at 1000 v net accelerating potential necessary to execute the North-South stationkeeping mission, and it has been used for this series of tests. The high voltage ignition system developed by Wintucky<sup>9</sup> and

used in these tests to demonstrate a rapid, reliable startup capability is shown in Figure 9. This system utilizes a 1  $\mu$ f capacitor which discharges through the secondary winding of a standard 12 v automobile ignition coil to produce a high voltage pulse. This pulse is applied to a tickler electrode located between the cathode and keeper electrodes across which the discharge is to be ignited. Actuation of the pulse occurs when the push button circuit is closed thereby triggering the silicon controlled rectifier (SCR) C30D shown in Figure 9.

Oscillographs of the potential difference between the tickler and the cathode show the tickler potential rises to voltages in the range 5000 v to 10,000 v in 10 to 30  $\mu$ sec before breakdown occurs between these electrodes. Oscillographs also show multiple breakdown-extinction cycles may occur after a single actuation of the circuit and that up to several milliseconds may expire between the time of actuation and the time when keeper currents in the range of tenths of an ampere begin to flow.

The tickler, a 1 mm diameter, 1% thoriated tungsten welding electrode with its tip ground to a sharp point, was installed perpendicular to the cathode axis. The axis of the tickler was located 0.05 cm from the face of the cathode tip on the basis of preliminary experiments by Wintucky. With the tickler in this location no change in thruster performance (as shown in Figure 2) was observed. The discharge capacitor charging voltage (225 v.d.c.) was selected on the basis of preliminary studies on a cathode-keeper assembly which showed this voltage was sufficient to effect repeatable discharge between the tickler and cathode at normal cathode flow rates. The keeper potential of 200 v was determined to be sufficient to effect a keeper discharge after the tickler electrode had been triggered. A similar preliminary study of the effect of cathode tip temperature on keeper discharge ignition probability showed a high probability that the keeper discharge would be an arc discharge above cathode temperatures around 400°C. Below 400°C keeper discharge ignitions which did occur resulted in a keeper-cathode glow discharge which did not result in sufficient cathode heating to bring up the cathode

SPARK IGNITION SYSTEM CIRCUIT  
FIGURE 9



temperature to the point where a transition to an arc discharge could occur.

The only change in the circuitry shown in Figure 9 from that suggested by Wintucky is the addition of the 1000  $\Omega$  resistor shown in the power line supplying the discharge capacitor. This resistor was found to be necessary to limit the rate at which the discharge capacitor was recharged after the SCR had been tripped. Without the resistor the capacitor would frequently not discharge completely for a sufficiently long period of time to allow the SCR to reset and in this condition the SCR represented a permanent short circuit across the power supply.

Testing of the system under conditions where breakdown did not occur at the tickler electrode resulted in high voltage breakdown through the bakelite between the primary and secondary terminals on the ignition coil and demonstrated the lowest resistance to high voltage breakdown at this point in the system.

#### Repetitive Startup Cycle Test Results

In order to demonstrate the suitability of the thruster and ignition system for repeated startup-shutdown cycle operation, two tests were conducted. The first one involved establishing all mercury flow conditions and the neutralizer discharge and then performing 1000 startup and shutdown cycles of the main discharge. The second series of tests involved establishing all flow rate conditions and then performing 1000 cycles of neutralizer followed by main discharge startup with subsequent termination of both discharges.

The main cathode used in these tests was first installed in the thruster several months before the tests mentioned above. The cathode insert had been dipped in chemical R-500 before cathode installation and no additional R-500 was added after this initial coating. The cathode had been operated for about 130 hours at the time the first test sequence began. The neutralizer cathode is a standard SERT II model; it had been operated for over 250 hours and had not been supplied with R-500 beyond

that applied at the time of fabrication for the SERT II flight program.

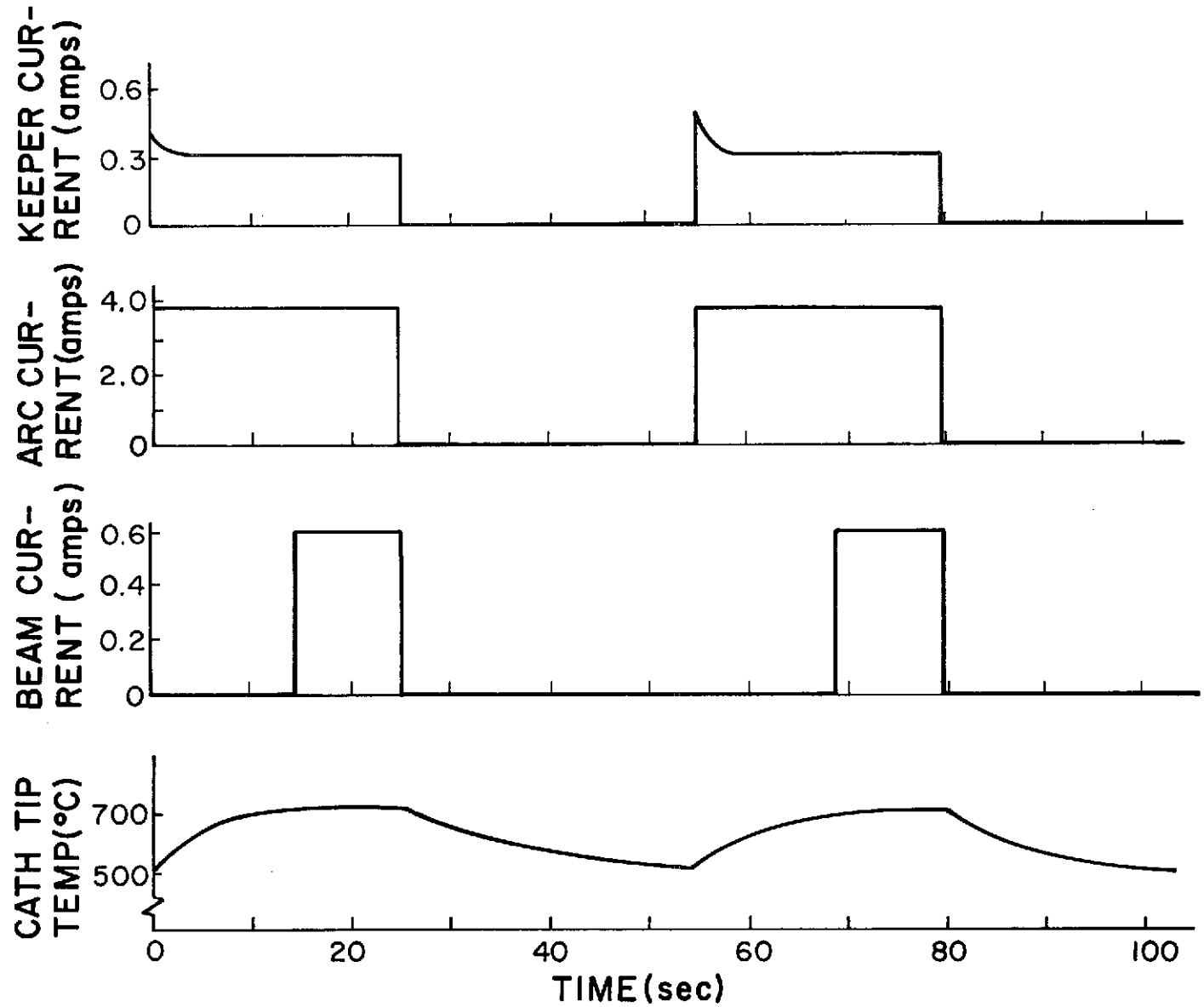
In conducting the first series of tests the main, cathode and neutralizer flow rates were established at 700 ma, 30 ma and ~20 ma respectively, and the neutralizer keeper discharge was established at a current of 0.2 amps. A main keeper voltage was then established at 200 v and the arc power supply was set to limit the arc current at about 3.9 amps once the arc discharge started. The cathode tip temperature was next raised to 500°C, a value selected as sufficiently far above the necessary temperature for startup (400°C) to assure a high startup reliability. The spark ignition system was actuated next, the keeper and arc discharges both established themselves and the keeper current was then adjusted to 0.3 amps. The high voltage was turned on next to establish a beam current; and the beam current, arc voltage, arc current, keeper voltage and cathode tip temperature were recorded. The high voltage, keeper and arc power supplies were subsequently turned off and when the cathode tip had cooled to 500°C, the spark ignition system was actuated again and the sequence was repeated until 1000 cycles had been completed. Two typical startup-shutdown cycles showing the times required to complete each portion of the cycle are presented as Figure 10. It shows that the typical cycle was completed in less than one minute. This test sequence demonstrated the startup probabilities shown below:

Frequency of startup on first actuation	-	99.0%
Frequency of startup on second actuation	-	0.8%
Frequency of startup on third actuation	-	0.2%

The second startup test sequence required the installation of a switch which facilitated connection of the high voltage output lines of the spark ignition system to either the main tickler or a neutralizer tickler. The neutralizer tickler was constructed and oriented perpendicular to the neutralizer cathode axis in the same way as the main tickler. The test sequence required establishment of the main, cathode and neutralizer flows at the same values used for the startup test sequence described previously. The neutralizer and main keeper potentials

FIGURE 10

THRUSTER STARTUP-SHUTDOWN TEST SEQUENCE (TYPICAL)



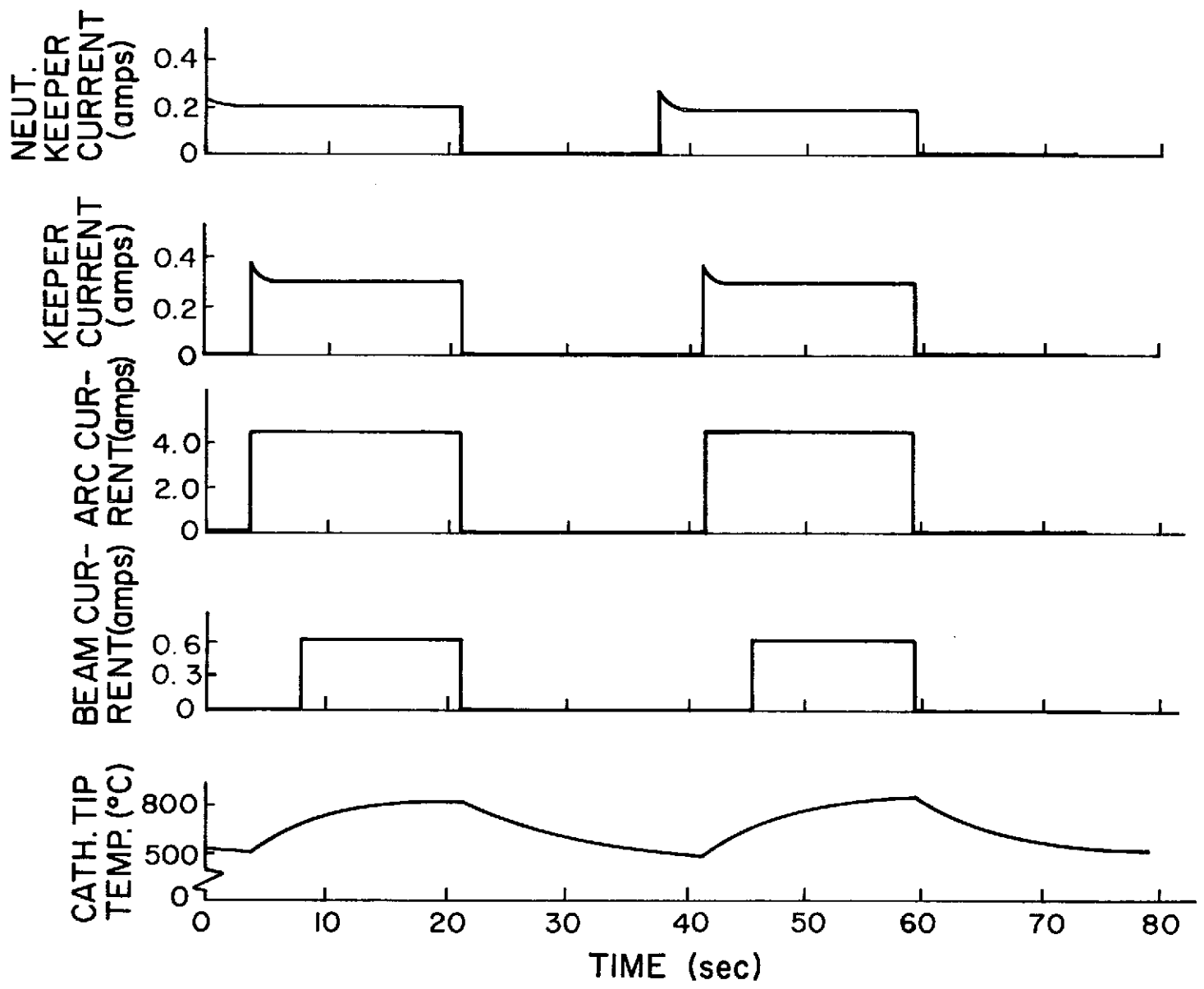
were both raised to 200 volts, the neutralizer cathode was heated to a temperature corresponding to a 1.9 amp current through the tip heater and the main cathode temperature was raised to 500°C. The arc power supply was adjusted to limit the arc current to about 4.1 amps. The subsequent events, shown in Figure 11, included initiation of the neutralizer discharge using spark ignition, adjustment of neutralizer keeper current to 0.2 a, spark initiation of the main keeper and arc discharges, adjustment of the main keeper current to a 0.3 a, and application of the high voltages to the thruster grids. After data had been recorded, the high voltage, arc, keeper and neutralizer keeper power supplies were turned off and the main cathode was allowed to cool to near 500°C before the startup sequence was repeated. One thousand such cycles were executed to complete the entire test. The frequency of discharge initiation as a function of number of actuations of the spark ignition system is as follows:

	Neutralizer Discharge	Main Discharge
Frequency of startup on first actuation	84.7%	95.0%
Frequency of startup on second actuation	5.6%	3.1%
Frequency of startup with three to five actuations	4.4%	1.3%
Frequency of startup where more than five actuations were required	5.3%	0.6%

When more than five spark ignition actuations were required to start the discharge a component or operator malfunction could generally be identified. This malfunctions included: 1) improper positioning of the switch used to connect the appropriate tickler to the ignition coil output, 2) low cathode tip temperature or flow rate, and most frequently 3) failure of the SCR (Figure 9) to reset following the previous ignition. This failure of the SCR was a result of improper design, and it was corrected by the installation of a 1000  $\Omega$  resistor in the line from the power supply used to charge the discharge capacitor.

NEUTRALIZER/THRUSTER STARTUP-SHUTDOWN TEST SEQUENCE (TYPICAL)

FIGURE 11



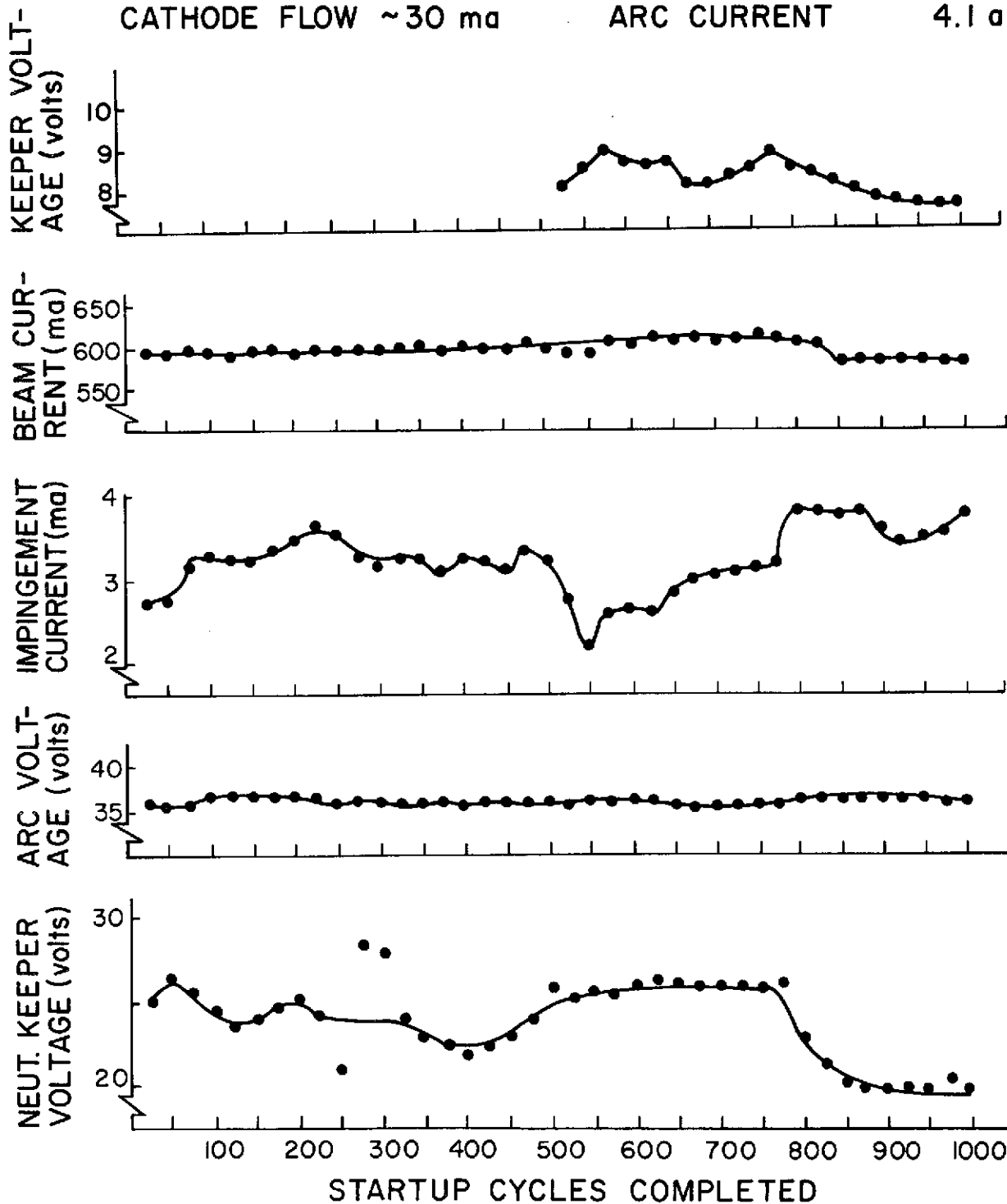
The variations in neutralizer keeper voltage, keeper voltage, impingement current, beam current and arc voltage during this test are shown in Figure 12 as a function of the number of startup cycles executed. These data show some variations in impingement current, keeper voltage, neutralizer keeper voltage and beam current. The variations are considered to be due to corresponding variations in flow rates which were observed to vary as much as  $\pm 15$  ma for main flow rates and  $\pm 5$  ma for cathode flow rates during the test.

Figure 13 shows the condition of the cathodes at the beginning and conclusion of each of the tests in addition to a photograph of the main cathode tickler at the conclusion of the first 1000 startups. To facilitate comparison all cathodes are oriented the same way in each photograph. Comparison of Figures 13a and 13b reveals some main cathode wear at the edge of the orifice plate (identified on Figure 13b). This wear appears at the point where the tickler passed over the orifice plate, and it appears to have occurred near the point where the ball of metal formed on the tickler (Figure 13d). For the second 1000 startup cycles of the main cathode no additional wear is observed, however, and the tickler which was replaced for this test appeared to be unchanged over the duration of the test.

The neutralizer cathode shown in Figures 13e and 13f before and after the test also shows no significant wear. As can be seen however the texture of the orifice plate surface does appear to be different. This apparent difference is caused by a coating of R-500 which was placed on the cathode face after the test series but before the photograph of Figure 13f was taken. The neutralizer tickler showed no significant wear after 1000 cycles.

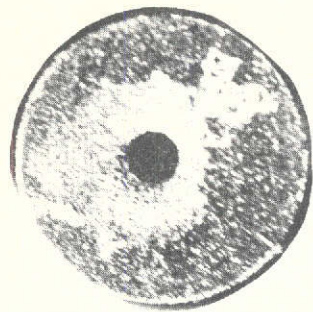
A comparison of the data on startup reliability of the main cathode for the two tests suggests the main cathode was more difficult to start during the second thousand tests. After the second thousand cycles both cathodes were sent out to be photographed and when they were returned neither could be started. Both cathodes were subsequently coated with

HIGH VOLTAGE +1kv, -0.5kv    NEUT. KEEPER CURR. 0.2 a  
TOTAL FLOW ~730 ma    KEEPER CURRENT 0.3 a  
CATHODE FLOW ~30 ma    ARC CURRENT 4.1 a

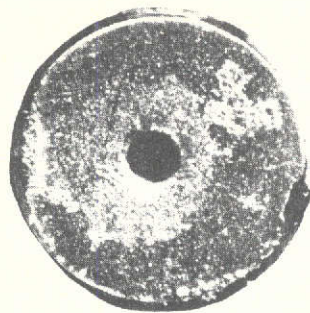


EFFECT OF INTEGRATED STARTUP CYCLES ON THRUSTER PARAMETERS

FIGURE 12

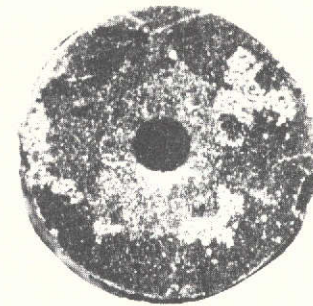


13a.) BEFORE TEST



13b.) AFTER 1000 STARTUP CYCLES

EROSION WHERE TICKLER PASSED OVER CATHODE

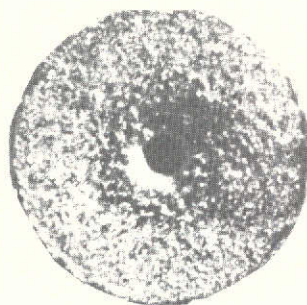


13 c.) AFTER 2000 STARTUP CYCLES

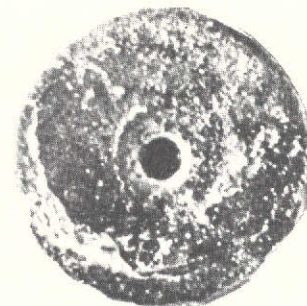
MAIN CATHODE



13d.) MAIN CATHODE TICKLER AFTER 1000 STARTUP CYCLES



13e.) BEFORE TEST



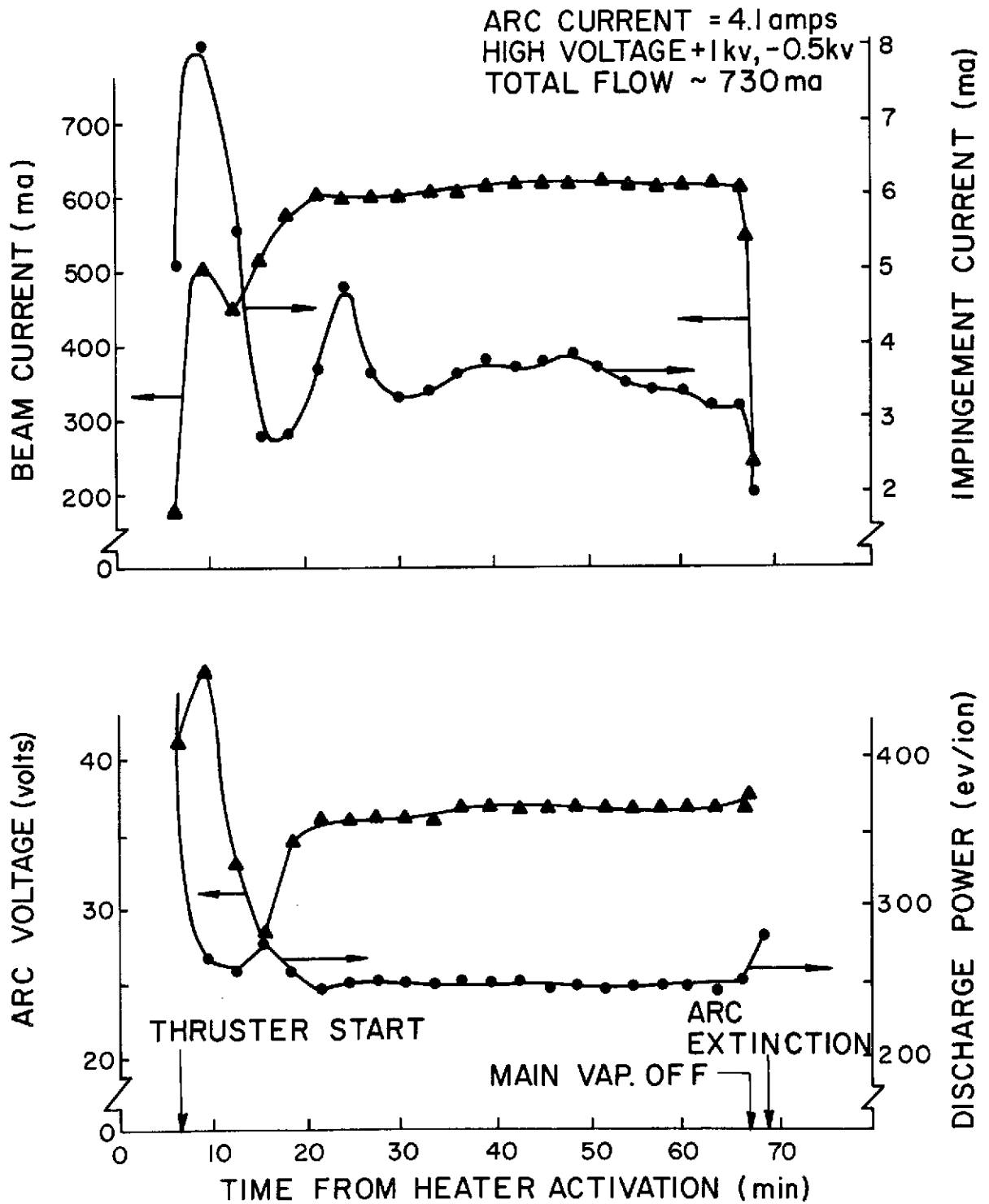
13 f.) AFTER 1000 STARTUP CYCLES

NEUTRALIZER CATHODE

R-500 and they restarted readily. It was after this that the final neutralizer photograph was found to be out of focus and it was rephotographed to obtain Figure 13f. It is believed that exposure to the aromatic chemical vapors in the photographic laboratory where the cathodes were stored for about a week while they were waiting to be photographed after each test series caused a degradation in startup reliability.

#### Rapid Startup Study

In order to prevent excessive propellant loss during a short thruster operating cycle it is necessary to be able to achieve rapid startup and shutdown of the system. Shutdown is not considered a particularly severe problem because the thruster can continue to operate and produce thrust after the vaporizers have been shutdown and until the flow rates drop to rather low values. Startup on the other hand requires a substantial flow rate to facilitate ignition, and propellant is lost during the time period when this flow is being established. Figure 14 shows results of a preliminary study indicating the variation in thruster parameters which might be expected during a 68 minute period in which the thruster was started and operated for an hour. Although the thruster flow rates were probably high enough for startup after 4 minutes of this test had past, two additional minutes were required to raise the cathode tip temperature because of an insufficiently high current setting on the tip heater. It is noted that within about three minutes after startup the thruster is operating at acceptable conditions, but it is not until 12 minutes after startup, when flow rates reach more nearly correct values, that performance parameters settle to their steady state values. Flow rates were controlled manually during this test, and it is anticipated that an automatic control system possibly coupled with higher power heaters capable of raising vaporizer and cathode temperatures more rapidly will facilitate very substantial gains in this area. Additional testing to determine propellant utilization over the complete startup-operation-shutdown cycle is required.



THRUSTER PARAMETER VARIATIONS DURING TRANSIENT OPERATING CYCLE

FIGURE 14

### Conclusion

A 15 cm mercury ion thruster operating with dished grids is capable of producing a 600 ma ion beam at a specific impulse of 2690 seconds and a beam ion cost of 250 ev/ion. Rapid, reliable ignition of the neutralizer and main discharges can be achieved using a spark ignition system. Use of this ignition system over some thousand cycles results in no significant degradation of the thruster components. Installation of the tickler electrode results in no increase in beam ion cost or decrease in propellant utilization efficiency. Additional attention is needed in the area of rapidly acting vaporizers and a control system capable of bringing flow rates to near the desired values in a time period of the order of one minute.

## SINGLE CUSP MAGNETIC FIELD THRUSTER

(J. R. Beattie)

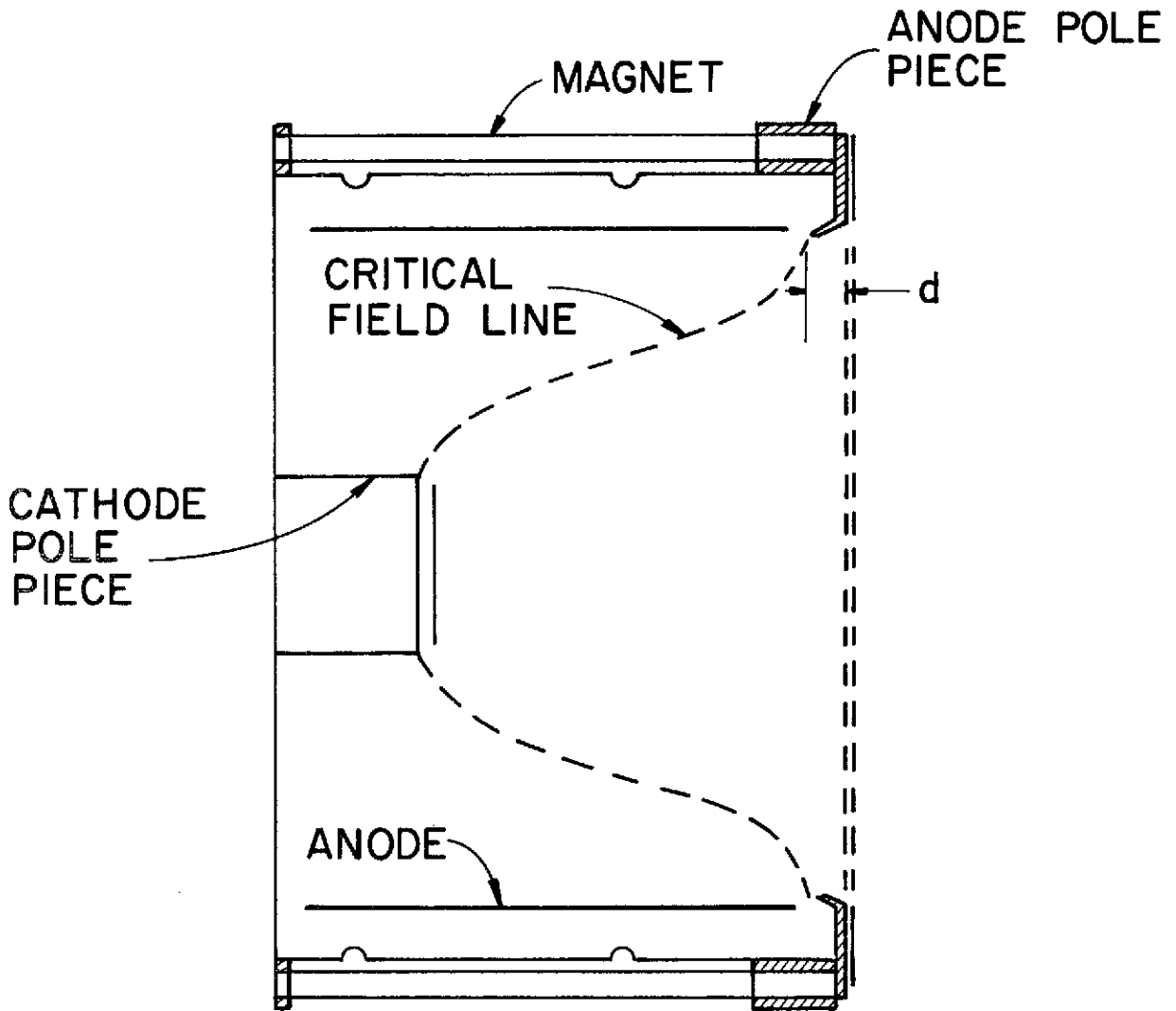
### Introduction

A major factor which determines the lifetime of an electrostatic ion thruster accelerator grid is the material erosion which occurs as a result of ion-neutral charge exchange reactions. This charge exchange reaction rate is dependent on the local ion and neutral number densities, and it is desirable to produce a uniform density profile for both the ions and neutrals in the vicinity of the accelerator grid to effect a uniform erosion rate. As a result then of the ion beam uniformity the time integrated thrust for a given grid lifetime is maximized.

A comparison of the ion density profile existing near the screen grid and the beam current density existing near the accelerator grid of a Kaufman thruster was conducted by Wilbur<sup>10</sup> and revealed that a good correlation exists between these profiles (correlation coefficient of 0.945). This high correlation suggests that a uniform ion density profile near the screen grid should result in a uniform current density in the ion beam.

The only thruster discharge chamber modifications which have resulted in a significant improvement in the uniformity of the ion beam current density profile have been related to the magnetic field configuration existing in the discharge chamber. The most significant improvement reported in the literature was achieved by the radial field thruster<sup>11</sup>. In this thruster the flatness parameter  $\epsilon$  (defined as the ratio of average to maximum beam current density) was increased from a value of about 0.4 for the SERT II thruster to 0.67. The increase in the flatness parameter is apparently due to a uniform radial plasma density which is found to exist in the radial field thruster.

Figure 15 presents the critical magnetic field line<sup>12</sup> geometry which exists in a SERT II-type divergent field thruster. It is apparent from this figure that there should be less ionization occurring at the



SERT II MAGNETIC FIELD GEOMETRY

FIGURE 15

outer radii of the discharge chamber. This occurs not only because of the lower electron densities and energies observed there, but also because of the reduced residence time of a neutral mercury atom in the ionizing region between the critical field line and the extraction grids. Using the residence time approach, one can argue that a properly shaped magnetic field would insure that the residence time for a neutral atom in the primary electron region (between the critical field line and the grids) should be much larger than the time between ionizing collisions. If  $\tau_n$  denotes the neutral residence time and  $\nu_c$  denotes the primary electron-neutral atom ionizing collision frequency, the design criterion can be expressed as

$$\tau_n \gg \frac{1}{\nu_c} \quad (1)$$

The residence time is related to the distance  $d$  between the critical field line and the extraction grid and the average neutral particle speed  $\bar{V}_0$  by the relation

$$\tau_n = \frac{d}{\bar{V}_0} \quad (2)$$

The collision frequency is related to the plasma properties by the relation

$$\nu_c = n_0 \sigma_0^+ V_p \quad (3)$$

where  $n_0$  is the neutral particle number density,  $\sigma_0^+$  is the electron-atom ionization cross section, and  $V_p$  is the speed of the primary electron. Using these expressions for  $\tau_n$  and  $\nu_c$  the residence time design criterion can be related to a minimum distance which should exist between the primary field line and the extraction grid. That is

$$d \gg \lambda_0^+ \frac{\bar{V}_0}{V_p} \quad (4)$$

where  $\lambda_0^+ = 1/n_0 \sigma_0^+$  is the mean free path for ionization of a neutral atom by a primary electron. Representative values of these parameters near

the walls of a SERT II thruster are:  $n_0 = 10^{18} \text{ m}^{-3}$ ,  $\bar{V}_0 = 230 \text{ m/sec}$ ,  $V_p = 3 \times 10^6 \text{ m/sec}$  (25 ev), and  $\sigma_0^+ = 2.4 \times 10^{-20} \text{ m}^2$ . Using these values the residence time criterion becomes

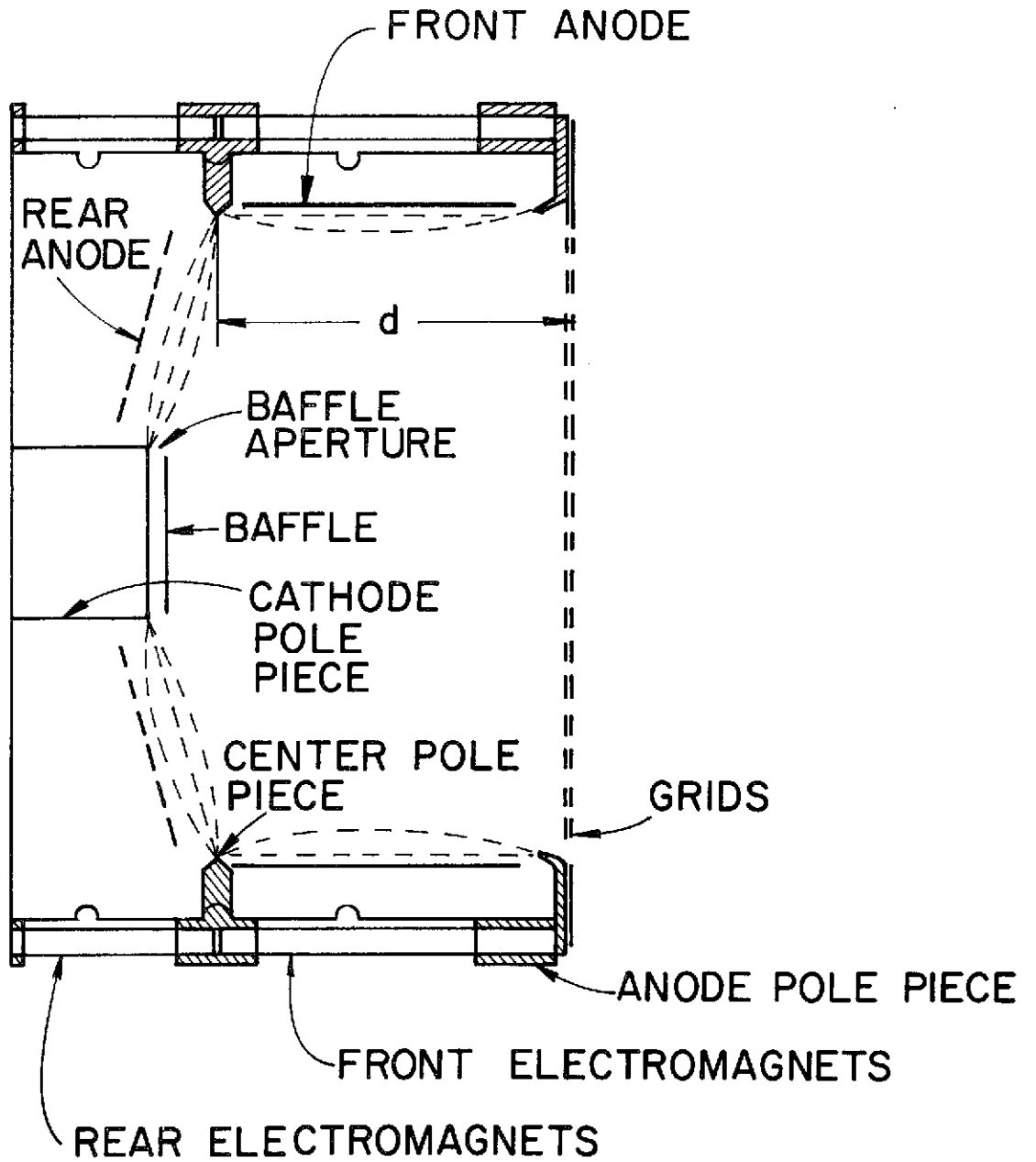
$$d \gg 3.2 \text{ mm} .$$

In order to insure a near 100% probability for neutral ionization at the outer radius of the thruster, the value of  $d$  should be at least an order of magnitude greater than the minimum value given above. That is,  $d$  should be approximately 32 mm. Since the value of  $d$  is estimated to be 7.6 mm for the SERT II thruster, the probability for ionization of a neutral in this region will be significantly reduced.

One method of increasing the distance  $d$  is by the addition of a cusped field electromagnet and anode as suggested in Figure 16. On the basis of the increased neutral residence time at the outer radii of the discharge chamber, a more uniform plasma density in the vicinity of the grids would be expected to exist with the cusped field configuration. This would then result in a more uniform ion beam profile as well as a reduction in neutral propellant loss at the outer radii of the thruster and hence a higher propellant utilization efficiency. An additional advantage of this type of field configuration is improved plasma confinement due to the predominantly axial magnetic field existing in the region adjacent to the anode. This improvement in plasma confinement should be accompanied by a reduction in discharge power losses plus a reduction in radial plasma density gradients provided the magnetic field is confined to the plasma region in close proximity to the anode.

### Apparatus

In an attempt to increase the residence time for neutrals at the outer radii of the discharge chamber, the magnetic field modification illustrated in Figure 16 was incorporated into a SERT II thruster. The major changes to the SERT II configuration consisted of the addition of the center magnet pole piece, a reduction in anode length, and the installation of the porous screen rear anode. Additional modifications



CUSPED MAGNETIC FIELD THRUSTER

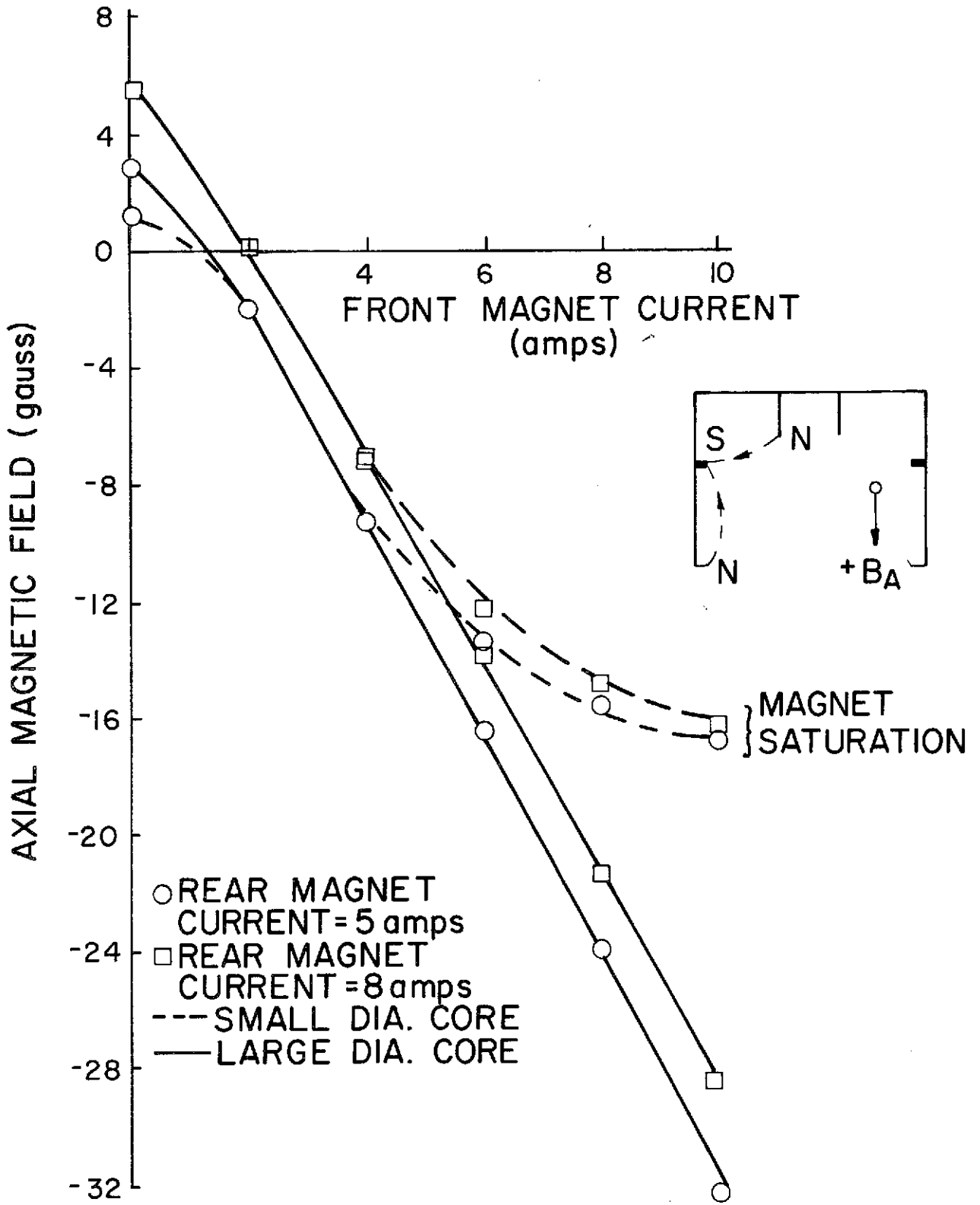
FIGURE 16

included the replacement of the SERT II permanent magnets with electromagnets and, during the course of the experiments, the installation of a variable magnetic baffle and a high perveance dished grid system. The SERT II propellant feed system was replaced by separate main and hollow cathode vaporizers; a modification which permitted individual control of main and cathode propellant flow rates. A hollow cathode with a 0.05 cm diameter orifice was also installed to facilitate sustained thruster operation at the high ion beam currents anticipated with the dished grids. Flat grids were maintained at +3 kv and -1.5 kv and dished grids were maintained at +1 kv and -0.5 kv during operation. A Faraday cup probe was installed 5 cm downstream of the accelerator grid to permit measurement of the ion beam current density profile. In addition, moveable Langmuir probes<sup>2</sup> were installed in the main and cathode discharge regions to obtain plasma diagnostic data.

All data presented in this section were obtained at a keeper current of 0.3 a. The 37 volt arc voltage operating condition is designated on performance curves presented herein by solid symbols. Discharge power calculations include keeper discharge losses in addition to the arc power losses.

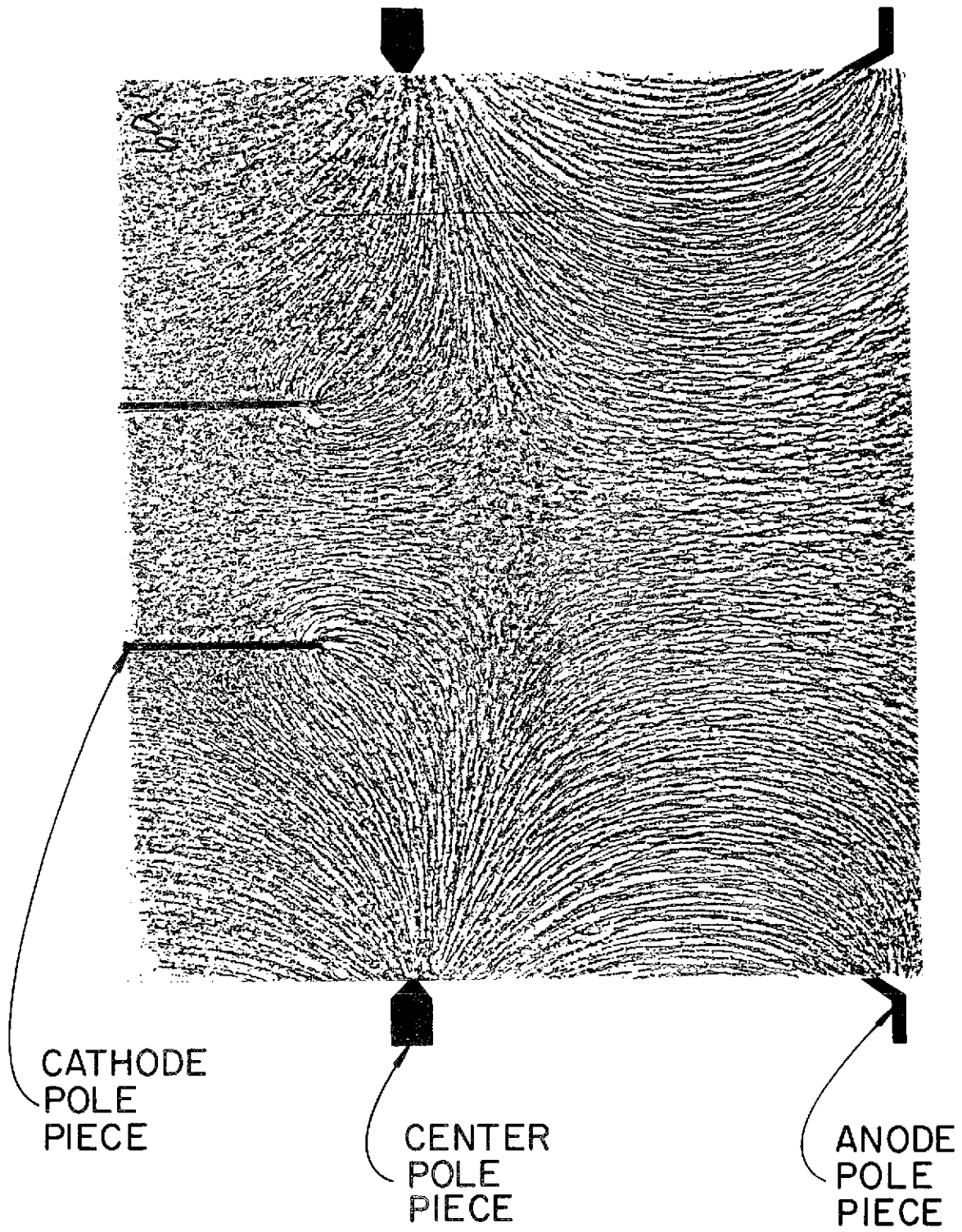
Early in the test program it was observed that the electromagnets, illustrated in Figure 16, were saturating at a relatively low value of magnetic field strength. Subsequently the electromagnets were redesigned to increase the cross sectional area of their iron core from 0.174 cm<sup>2</sup> to 0.658 cm<sup>2</sup> so higher magnetic field strengths could be achieved in the discharge chamber. Typical magnetic field measurements taken at one point in the discharge chamber with both sets of electromagnets operating are presented in Figure 17. These data indicate that at a front magnet current of 10 A the magnetic field strength was doubled by the use of larger diameter electromagnets and no evidence of saturation was present.

An iron filings map of the magnetic field existing in the discharge chamber is presented in Figure 18. Magnetic field strength measurements



MAGNETIC FIELD MEASUREMENTS

FIGURE 17



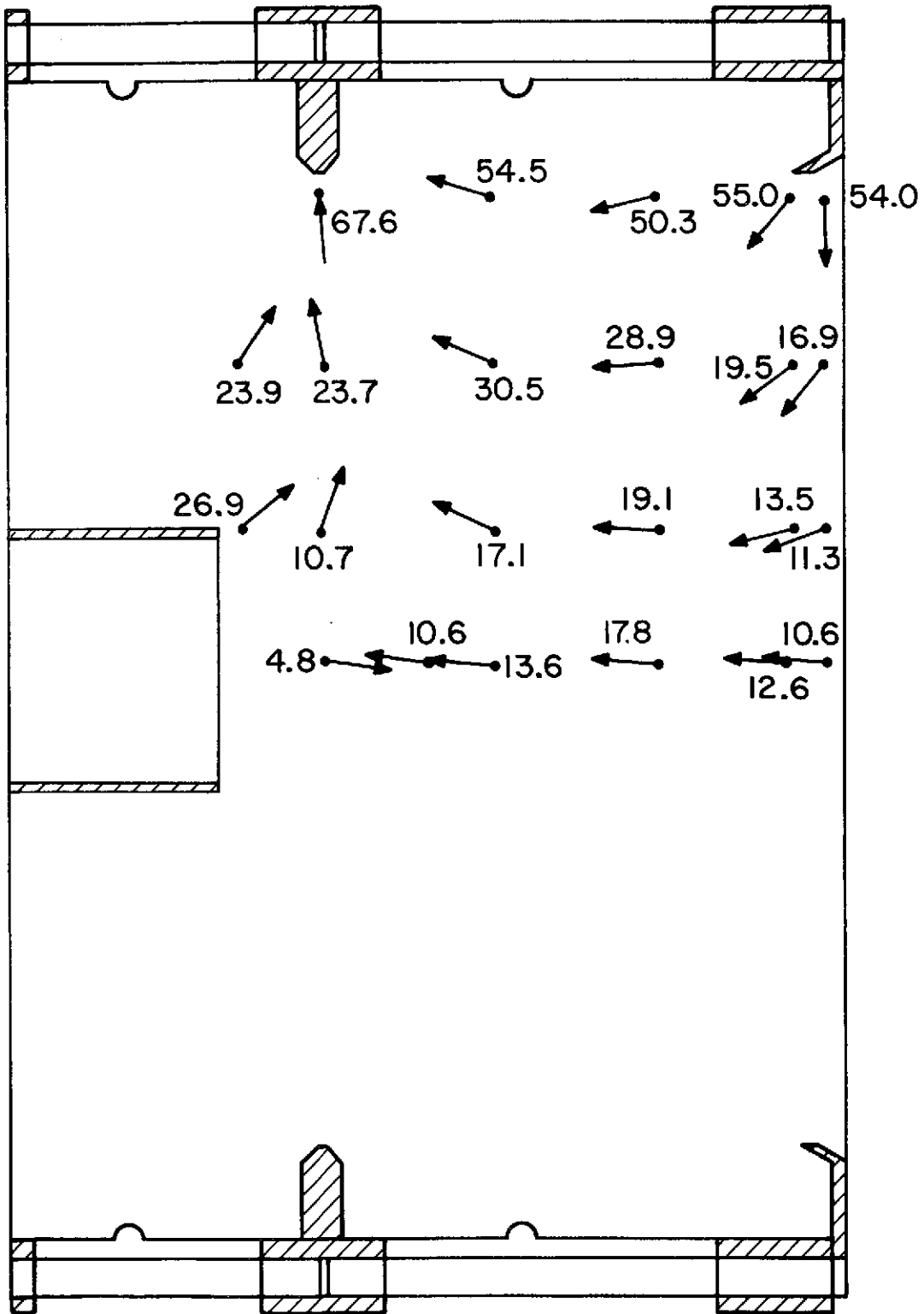
IRON FILINGS MAGNETIC FIELD MAP

FIGURE 18

were made at various locations in the discharge chamber for magnet currents typical of optimum thruster operation. The results of these measurements are illustrated in Figure 19, which shows the magnitude (in Gauss) as well as the direction of the magnetic field. The data presented in both of these figures were obtained without the magnetic baffle energized.

### Anode Configuration Experiments

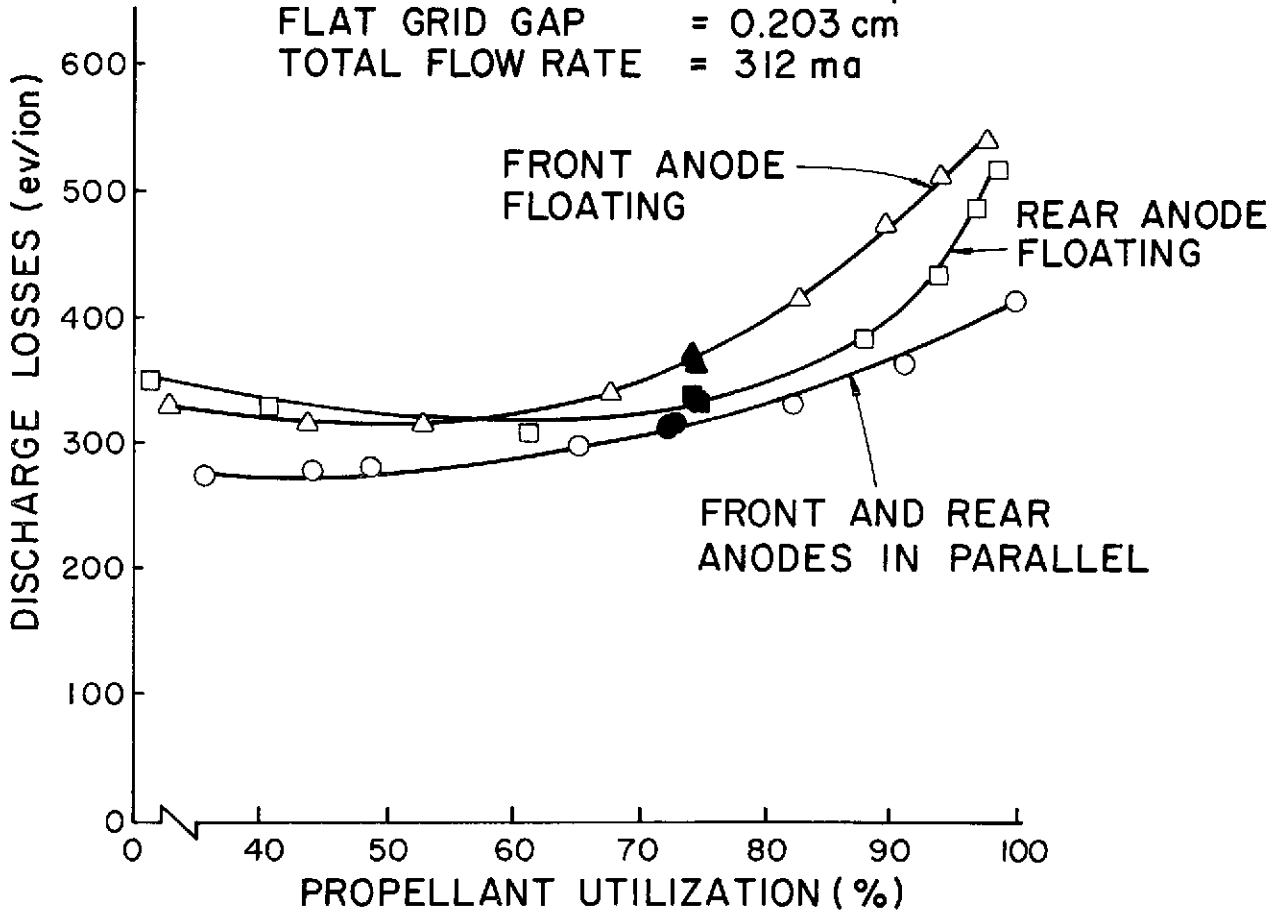
One of the first investigations conducted on the cusped magnetic field (CMF) thruster was to determine the optimum anode configuration. Figure 20 presents performance data obtained at a 312 ma total flow rate with flat SERT II grids. Data are presented for the front and rear anodes connected electrically in parallel, for the rear anode at floating potential, and for the front anode at floating potential. These data indicate that the best thruster performance is achieved with the parallel anode configuration. Also, the qualitative effect of drawing current to the rear anode is to reduce significantly the slope of the performance curve at high propellant utilization efficiencies. The fraction of the arc current drawn to the rear anode also determines the ease with which 100% propellant utilization is approached. The suspiciously high utilization indicated in these figures is considered to be a characteristic of the CMF thruster design rather than errors in flow rate measurements and will be discussed in more detail in a later section of this report. Figure 21 presents additional performance data obtained at a high total flow rate and with uncompensated high permeance dished grids rather than the flat grids used for the data of Figure 20. Data are presented for the parallel anode configuration and also for the rear anode at thruster body potential. Again it is apparent that the effect of drawing current to the rear anode is to reduce the slope of the performance curve at high utilization as well as to reduce the baseline discharge losses. That the achievement of high propellant utilization is associated with the rear anode is clearly demonstrated by the fact that a propellant utilization of over 100% was easily obtained with the parallel anode configuration.



MAGNETIC FIELD MAGNITUDE AND DIRECTION

FIGURE 19

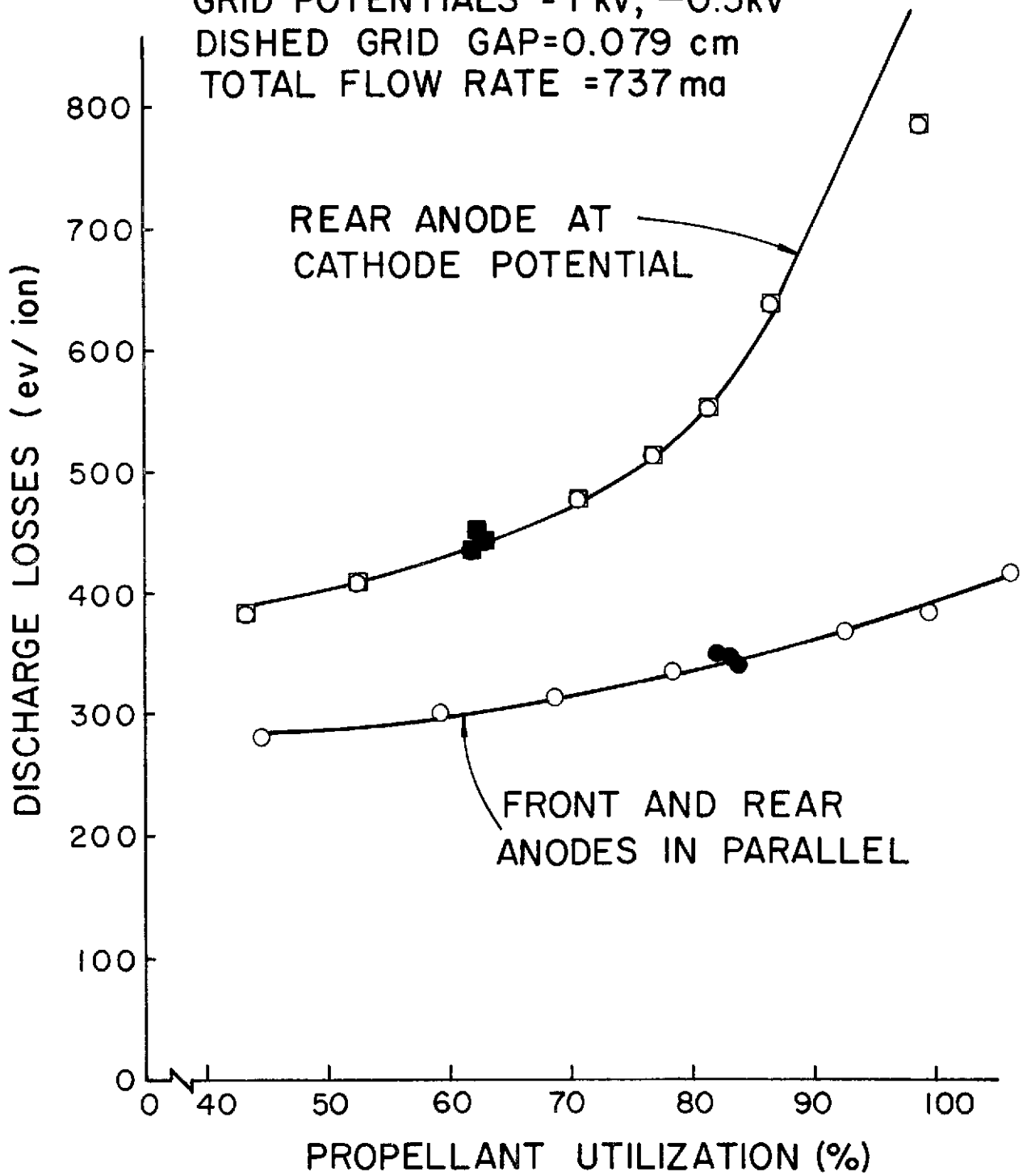
GRID POTENTIALS = 3 kv, -1.5 kv  
FRONT MAGNET CURRENT = 7 amps  
REAR MAGNET CURRENT = 8 amps  
FLAT GRID GAP = 0.203 cm  
TOTAL FLOW RATE = 312 ma



EFFECT OF ANODE CONFIGURATION ON PERFORMANCE - FLAT GRIDS

FIGURE 20

GRID POTENTIALS = 1 kv, -0.5kv  
DISHED GRID GAP=0.079 cm  
TOTAL FLOW RATE =737 ma



EFFECT OF ANODE CONFIGURATION ON PERFORMANCE - DISHED GRIDS

FIGURE 21

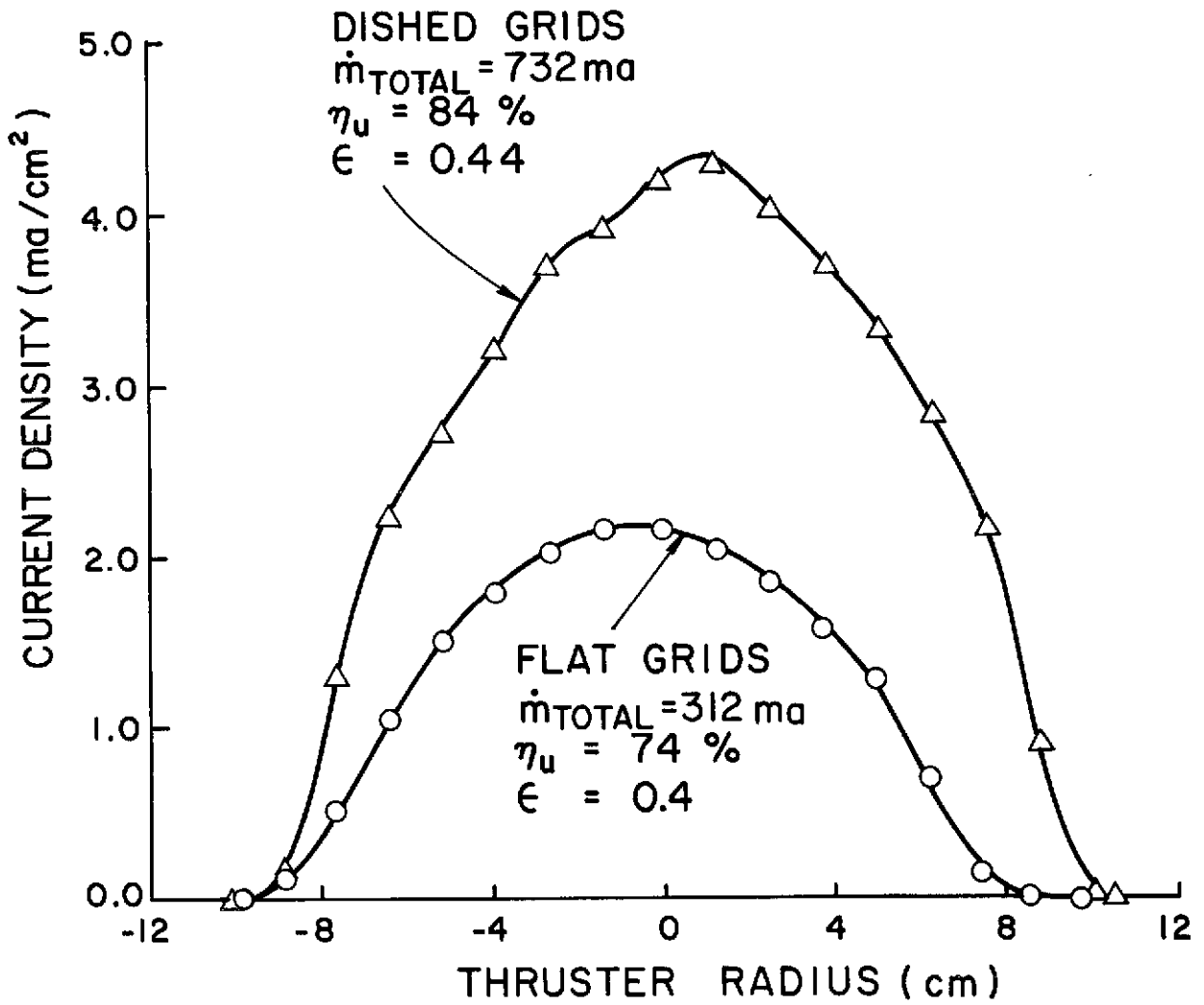
Comparing the parallel anode data at the low total flow (flat grids) with that for the high total flow (dished grids) indicates that essentially the same performance is achieved in either case. This tends to support the conclusion reached in Reference 13 and the first section of this report that optimum thruster performance over a throttling range can be achieved by reducing the grid system transparency as flow rate is reduced.

It was found that the parallel anode configuration resulted in the flattest ion beam profile. A comparison of measured ion beam profiles for this configuration at high and low total flow rates is presented in Figure 22. Comparison of these data with those of Figures 3 and 4 in the first section of the report suggests a slightly flatter ion beam profile for the CMF thruster.

#### Throttling Experiments

The effects of varying the total propellant flow rate into the discharge chamber are illustrated in Figure 23. These data were obtained with dished grids at a +1.0 Kv screen grid potential and a -0.5 Kv accelerator grid potential. The cathode flow rate was in the range 80 to 110 ma. As the figure indicates, the baseline discharge losses are not significantly affected by the total flow rate. However, it is evident that the effect of increasing the total propellant flow is to flatten out the performance curve and to facilitate operation at propellant utilization efficiencies in excess of 100%.

The effect of total propellant flow rate on discharge losses evaluated at 37 v arc voltage and 85% propellant utilization efficiency is illustrated in Figure 24. This curve suggests that the discharge losses for these conditions are minimized when the total propellant flow rate is in the 550 to 700 ma range. Flow rates in excess of 765 ma were found to result in unstable thruster operation.



ION BEAM CURRENT DENSITY PROFILE

FIGURE 22

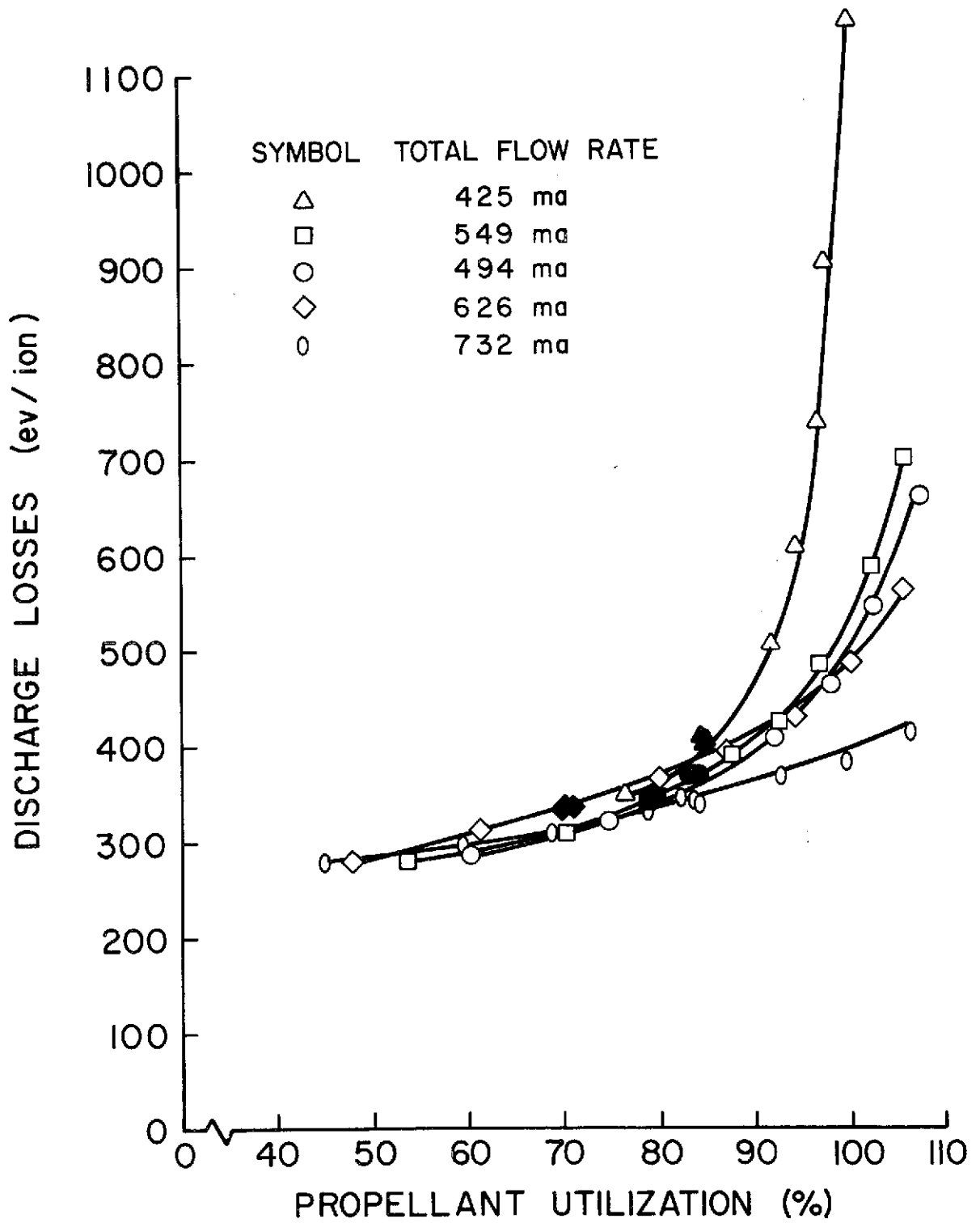
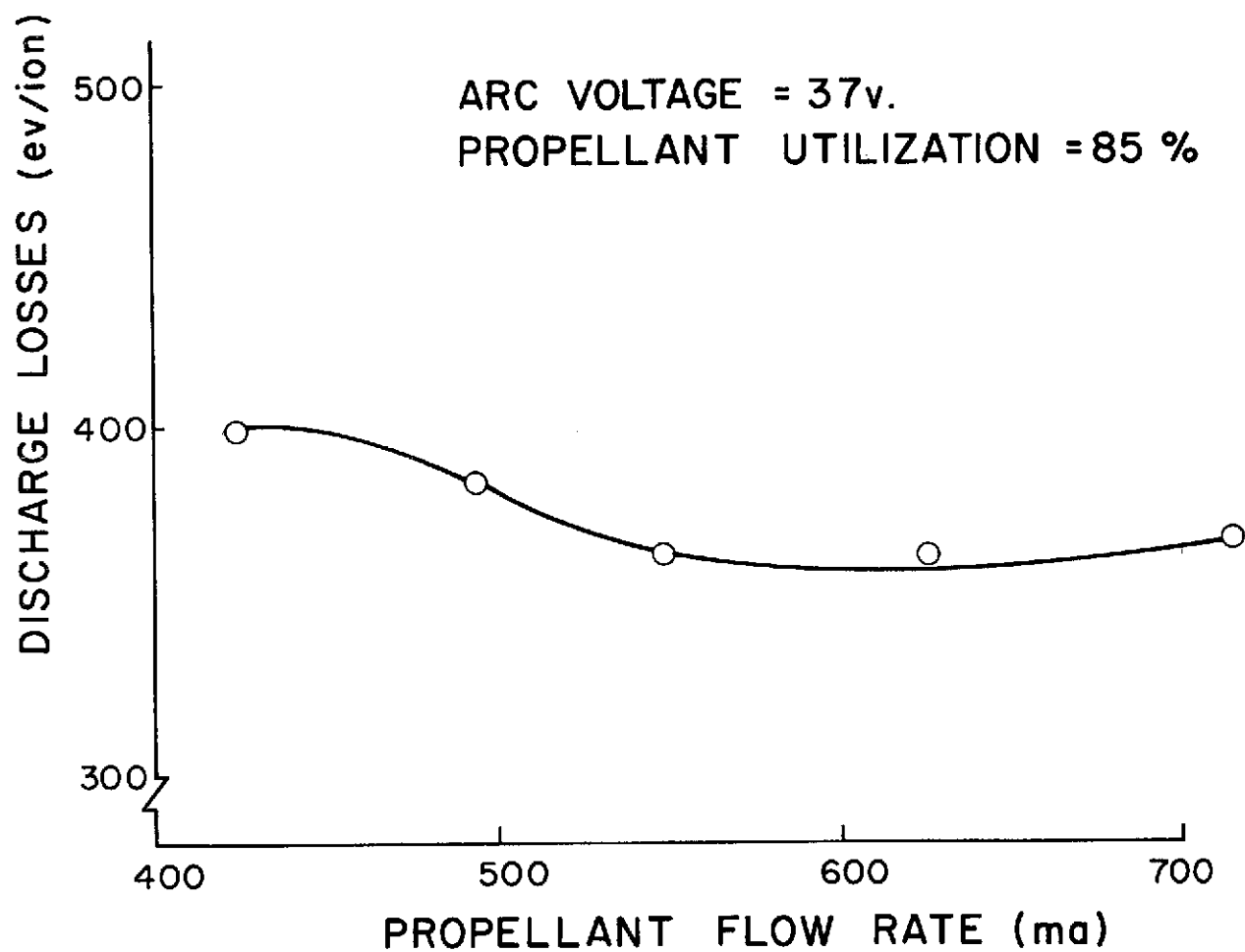


FIGURE 23



EFFECT OF TOTAL PROPELLANT FLOW RATE ON DISCHARGE LOSSES

FIGURE 24

### Variable Magnetic Baffle Effects

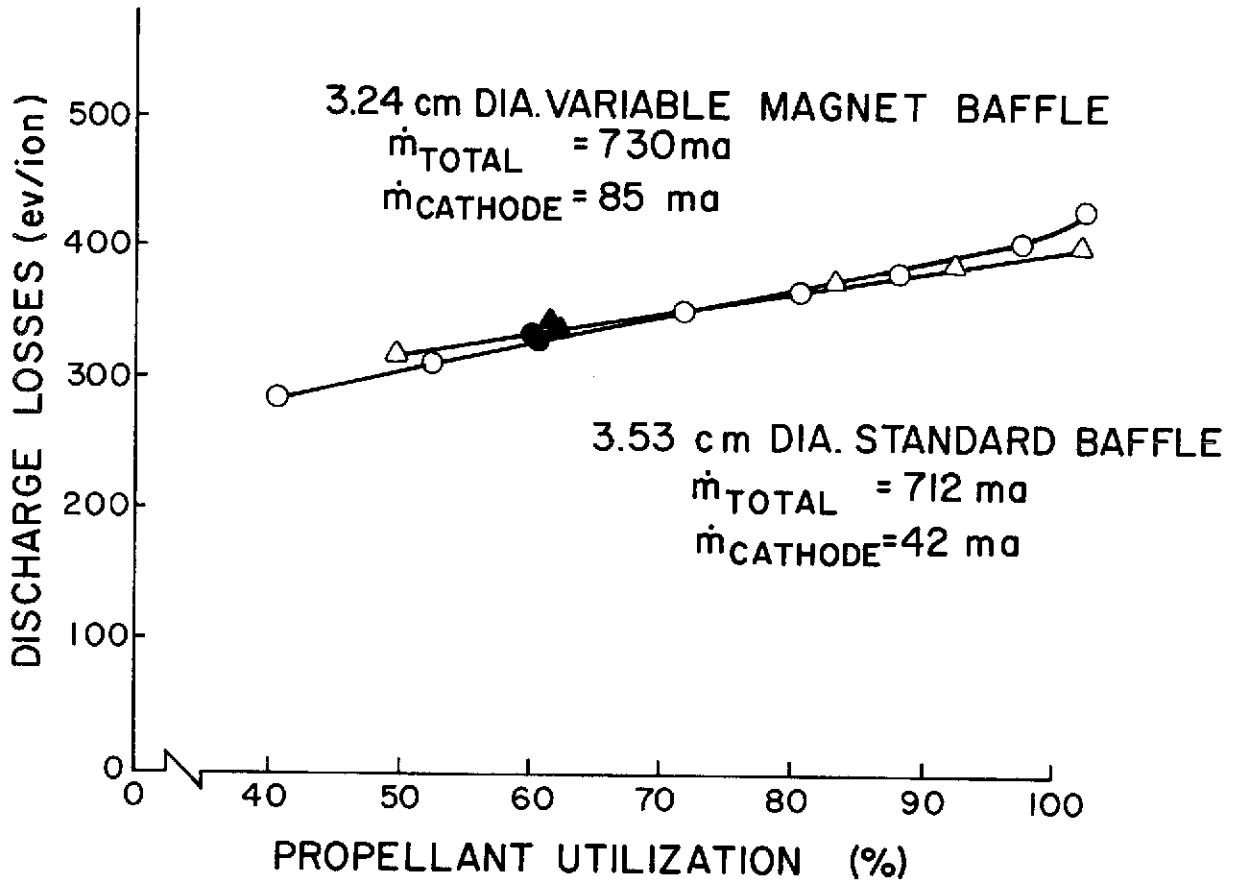
A 3.24 cm diameter variable magnetic baffle<sup>14</sup> was installed in the CMF thruster to facilitate experimental evaluation of various thruster operating conditions. The addition of the variable magnetic baffle permitted the direct control of the impedance to electron flow across the baffle aperture.

Figure 25 presents a performance comparison between the variable magnetic baffle and a 3.53 cm diameter non-magnetic baffle. This larger baffle had been used earlier in the program to achieve a 37 v arc voltage at a reasonable cathode flow rate. The figure indicates that the performance was essentially unchanged by the addition of the magnetic baffle.

The variable magnetic baffle also permits the acquisition of performance data over a range of propellant utilization at a constant arc voltage. This is accomplished simply by varying the baffle magnet current to maintain a fixed arc voltage as the arc current is varied. Figure 26 illustrates the effects on performance of maintaining a constant 37 v arc voltage throughout the propellant utilization range. These data indicate a significant difference in the discharge power losses for the variable and fixed arc voltage mode of data acquisition. A similar comparison at the higher total flow rates does not reveal much difference in discharge losses. This is due to the fact that at the higher total flow conditions the arc voltage does not vary significantly over a wide range of propellant utilization.

### Cathode Flow Rate Effects

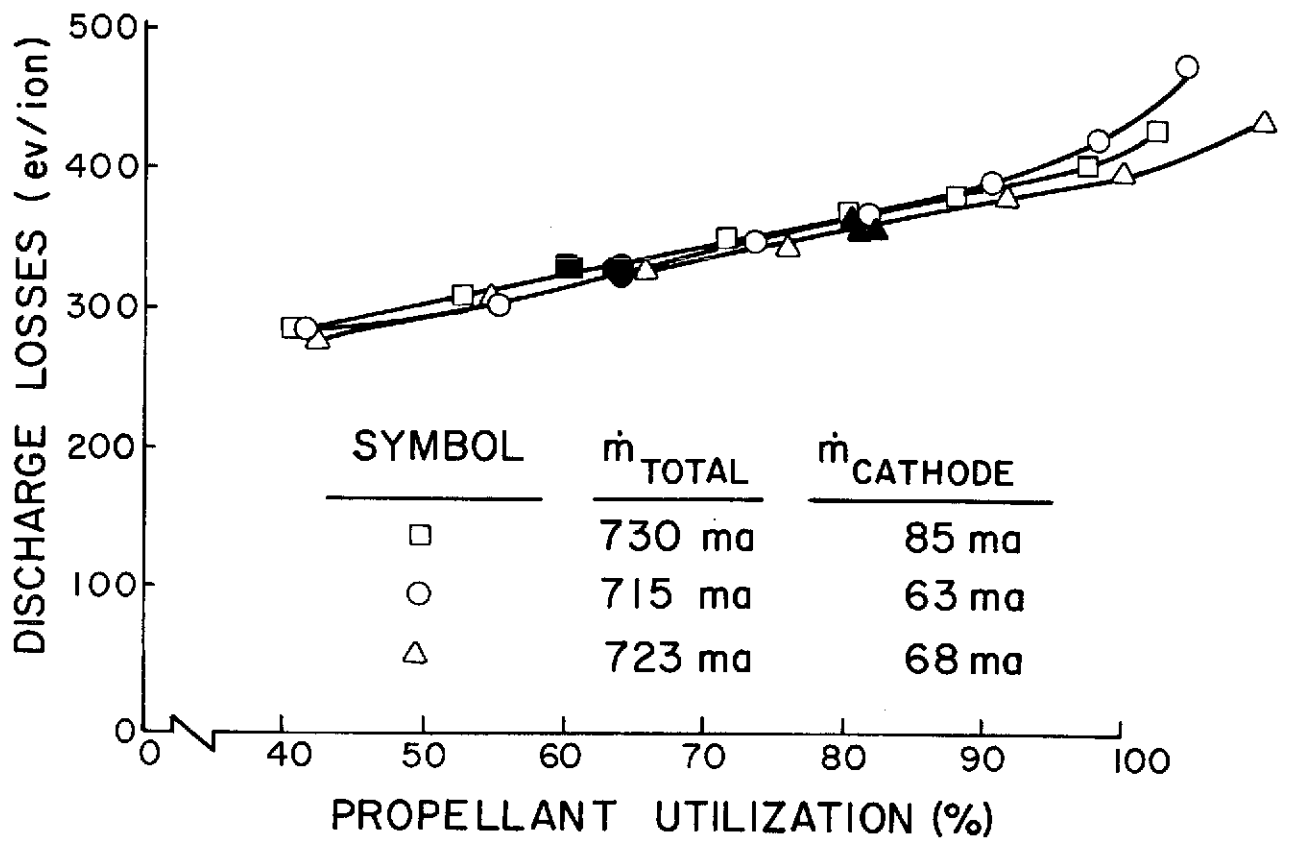
Figure 27 presents performance data obtained at various cathode flow rates and with magnet currents which resulted in minimum discharge power losses. These data and those of Figure 25 as well as some data obtained without the magnetic baffle and not presented here indicate that thruster performance is relatively insensitive to cathode flow rate over a wide range of propellant utilization. It has been observed



PERFORMANCE COMPARISON OF THE VARIABLE MAGNETIC BAFFLE AND THE NON-MAGNETIC STANDARD BAFFLE

FIGURE 25





EFFECT OF CATHODE FLOW RATE ON THRUSTER PERFORMANCE

FIGURE 27

that thruster operation becomes somewhat unstable at very low cathode flow rates (~18 ma) and also at very high flow rates (>110 ma). Based on these observations it is concluded that a reasonable cathode flow rate range over which thruster performance doesn't vary greatly is 30 to 100 ma.

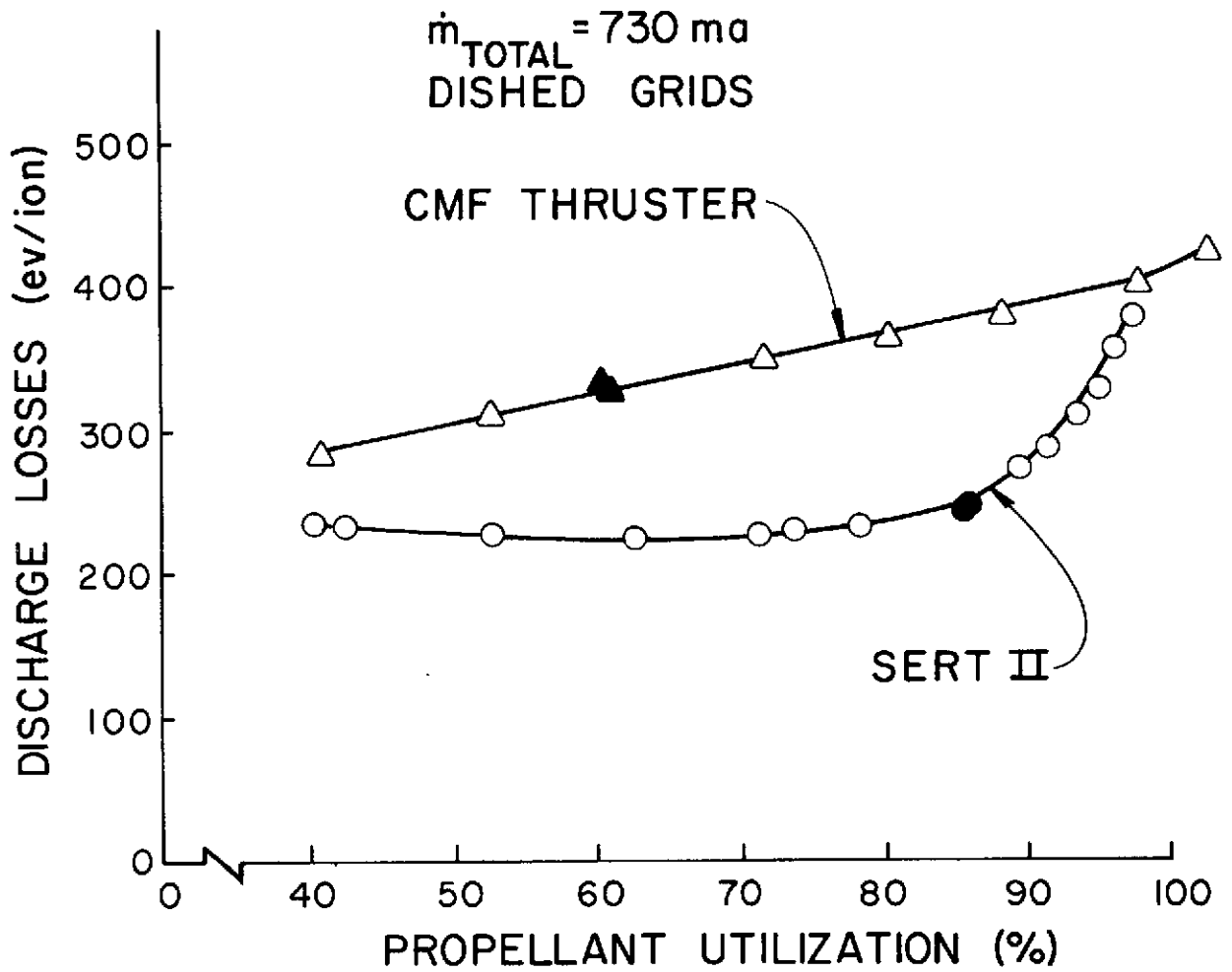
#### Performance Comparison with SERT II Discharge Chamber

A performance comparison of the C.S.U. modified SERT II and CMF thrusters (both equipped with dished grids) is presented in Figure 28. These data indicate that the baseline discharge losses of the CMF thruster exceed those of SERT II by about 100 ev/ion at 60% utilization. In an attempt to understand the reason for increased losses in the CMF thruster a comparison of the measured plasma properties for both thrusters was made. The plasma properties obtained from Langmuir probe data were averaged along the thruster centerlines and the results are presented in Table I. These data indicate that at essentially the same flow rate and arc power the ion beam produced by the CMF thruster was

Table I. Comparison of CMF and SERT II Plasma Properties

	CMF Thruster	SERT II Thruster
Total flow rate	730 ma	734 ma
Cathode flow rate	85 ma	34 ma
Arc current	3.9 A	4.32 A
Arc voltage	37 v	36 v
Beam current	449 ma	632 ma
Primary electron density	$6.7 \times 10^{10} \text{ cm}^{-3}$	$8.1 \times 10^{10} \text{ cm}^{-3}$
Maxwellian electron density	$34 \times 10^{10} \text{ cm}^{-3}$	$40 \times 10^{10} \text{ cm}^{-3}$
Maxwellian electron temperature	2.2 ev	3.7 ev
Primary electron energy	16 ev	27 ev
Plasma potential	38.7 v	36.3 v

only about 70% of the SERT II value. The reason for the significantly lower propellant utilization is apparent when one compares the electron



PERFORMANCE COMPARISON OF THE CMF AND SERT II THRUSTERS

FIGURE 28

densities and energies existing in the two thrusters. From the data in the table it can be seen that the CMF thruster primary electron energy and Maxwellian electron temperature are about 60% of the SERT II values. Also, the electron densities are only about 85% of those observed in the SERT II thruster.

Another striking dissimilarity in the two curves presented in Figure 28 is the lack of a "knee" in the performance data presented for the CMF thruster. The lack of the "knee" and the apparent propellant utilization of over 100% are thought to be intimately related and will be discussed in greater detail in the next section.

### Discharge Chamber Theory

When operating the CMF thruster it was found that the electromagnet currents which resulted in minimum discharge losses forced about 70 to 80% of the arc current to the rear anode. The somewhat unusual performance characteristics of the thruster are thought to be due to this large rear anode current fraction.

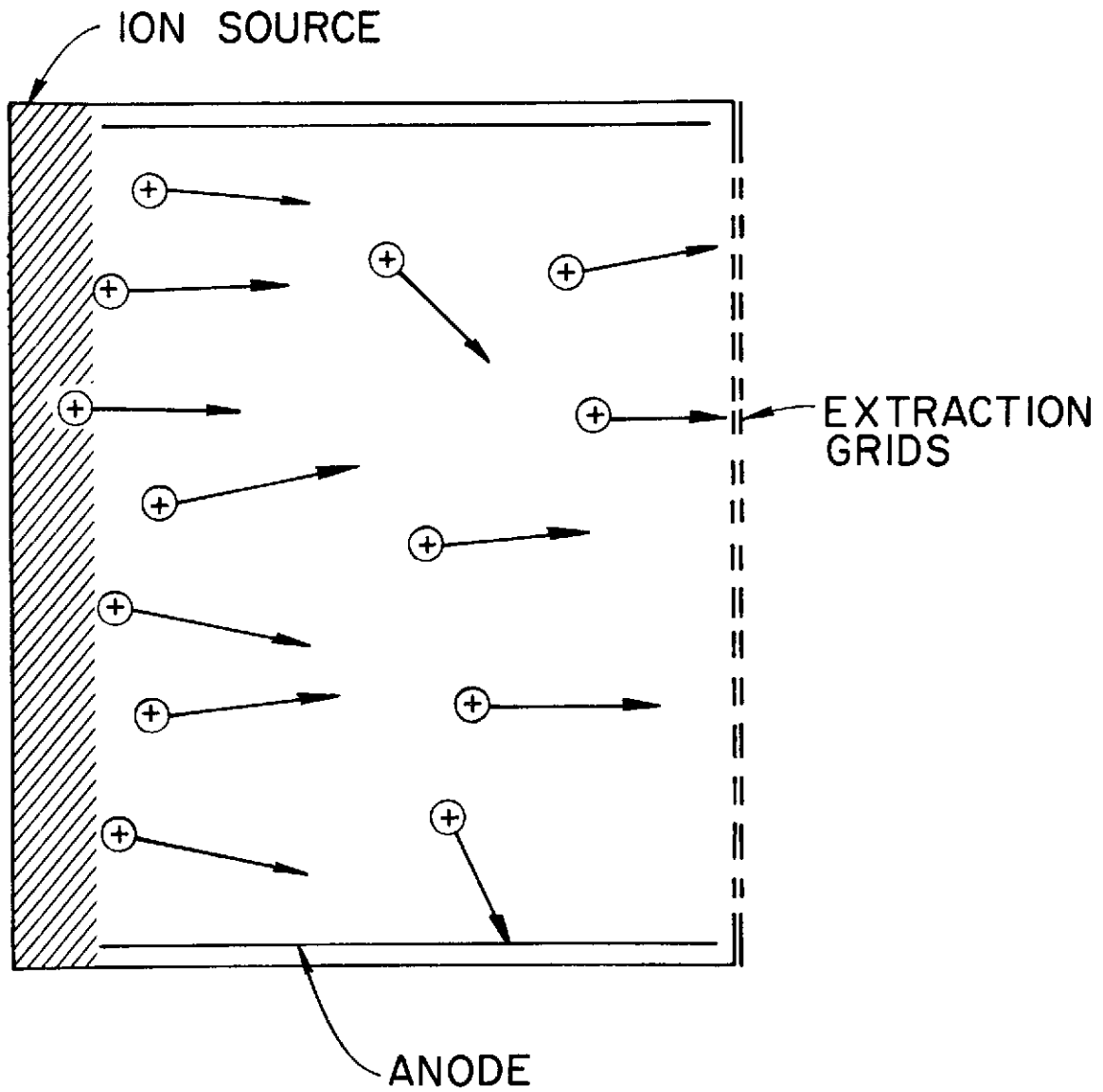
Consideration of the magnetic field configuration illustrated in Figure 18 suggests that a magnetic bottle exists in the region between the cathode and center magnet pole pieces. This bottle tends to trap the primary electrons which leave the baffle aperture as well as some of the Maxwellian electrons which originate from the ionizing collisions which occur inside the confinement region. Due to this electron containment a high concentration of energetic primaries and Maxwellians would be expected to exist in this region. Since the Debye length is very small the concentration of ions should be very high also. Physically this implies that as the neutral atoms drift through the porous rear anode they enter the high energy density region confined by the bottle and many become ionized. This argument suggests that the discharge chamber might be modeled by a cylindrical region with a planar ion source at one end and a set of extraction grids at the other. The magnetic field which exists in the chamber is predominantly axial and tends

to inhibit electron flow to the anode. This model of the discharge chamber is depicted in Figure 29.

After the formation of the ion at the source, there are three possible methods of extinction. These are: (1) the ion drifts to the screen electrode where it either recombines or is extracted, (2) the ion recombines on the anode surface, or (3) the ion becomes a double ion as the result of an inelastic collision with an electron. Due to the rather long distance between the ion source and the screen electrode, it appears that the probability of the second and third events occurring is quite high. That is, there is a good chance that the ion formed at the source will either be lost to the anode or become doubly ionized.

Due to the high probability that an ion will be lost to the anode, one would expect the discharge losses to be rather high. This is indeed the case with the CMF thruster. As was stated above, the effect of the magnetic field in the region between the cathode and center magnet pole pieces is to confine the electrons. Some electrons will be scattered out of this region and it seems reasonable that the electron energy and density existing in the remainder of the discharge chamber would be relatively low. As a result, the probability of a neutral atom becoming ionized in this region of the chamber is reduced. The data presented in Table I indicate that the electron energies and densities averaged along the CMF thruster centerline are somewhat less than those existing in a conventional thruster. Also, for approximately the same input power the propellant utilization in the CMF thruster was only about 70% of that in the SERT II.

Although the region confined by the magnetic bottle has not been probed, plasma measurements made elsewhere in the discharge chamber tend to support the theory outlined above. Figure 30 presents a comparison between the electron number density measured in the CMF and SERT II thrusters. The CMF data indicate a general trend for the electron densities to increase in the direction of the rear anode. It is also evident that the magnitude of the plasma density is somewhat less than that of the SERT II throughout the rest of the discharge chamber.



CMF THRUSTER DISCHARGE CHAMBER MODEL

FIGURE 29

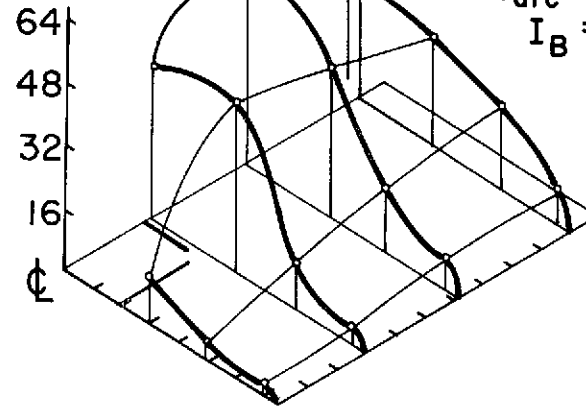
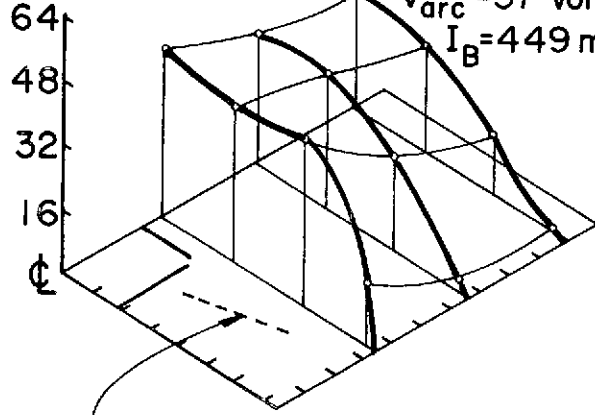
CMF THRUSTER

$\dot{m}_T = 730 \text{ ma}$   
 $\dot{m}_C = 85 \text{ ma}$   
 $I_{\text{arc}} = 3.9 \text{ amps}$   
 $V_{\text{arc}} = 37 \text{ volts}$   
 $I_B = 449 \text{ ma}$

SERT II THRUSTER

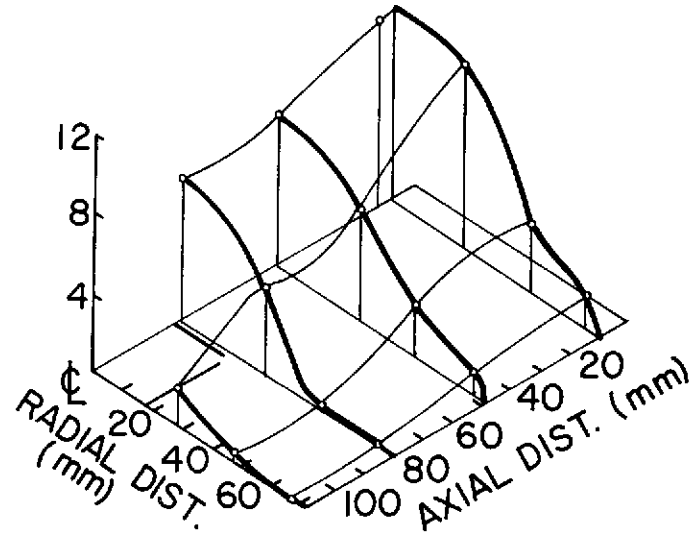
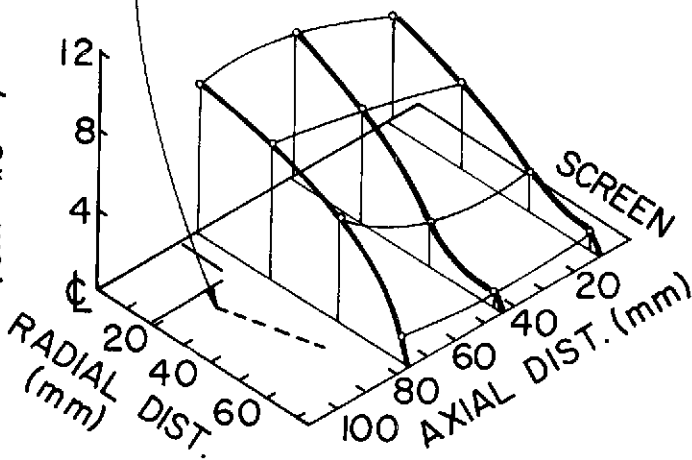
$\dot{m}_T = 734 \text{ ma}$   
 $\dot{m}_C = 34 \text{ ma}$   
 $I_{\text{arc}} = 4.3 \text{ amps}$   
 $V_{\text{arc}} = 36 \text{ volts}$   
 $I_B = 632 \text{ ma}$

MAX. ELEC. DENS.  
 $(\text{cm}^{-3} \times 10^{-16})$



REAR ANODE

PRI. ELEC. DENS.  
 $(\text{cm}^{-3} \times 10^{-10})$



CMF AND SERT II PLASMA DENSITY COMPARISON  
 FIGURE 30

### Ion Beam Profile Theory

Since many of the ions formed at the planar source mentioned previously are lost to the anode one would expect the ion number density to be reduced at the outer periphery of the discharge chamber. This effect is confirmed by Langmuir probe measurements taken inside the chamber and Faraday probe measurements of the ion beam profile.

Another factor which can influence the beam profile significantly is the presence of double ions in the discharge chamber. Due to the higher concentration of ions and electrons in the center of the discharge chamber, doubly charged ions are preferentially produced in this region. This distorts the single ion current densities at the center of the discharge chamber and decreases the ion beam flatness parameter. Since double ions are produced predominantly by a second ionization of singly charged ions this effect is more pronounced in the CMF thruster. In this thruster a single ion produced at the rear of the thruster must traverse a significant distance before it reaches the extraction grids. Hence there is a significant probability that the second ionization can occur during this traversal.

### The Effect of Double Ions on Performance Data

The flat performance curves observed in the cusped field thruster require some justification. The following theoretical development is intended to show that small double ion fractions result in an apparent increase in propellant utilization and an apparent reduction in discharge power (ev/ion) which causes the performance curve based on measured data to be flattened out.

The ion beam current for the case where both doubly and singly ionized species are present is given by the expression

$$I_{B_{+,++}} = qn_{+}v_{+}A_{0} + 2qn_{++}v_{++}A_{0} \quad , \quad (5)$$

where  $q$  is the electronic charge,  $n_{\beta}$  and  $v_{\beta}$  are the number density and

velocity of specie  $\beta$ , and  $A_0$  in the open area of the grids. In the expression above the number densities are taken as the average value existing at the accelerator electrode. If there are no double ions present the current is given by

$$I_{B_+} = qn_{o_+} v_+ A_0 \quad , \quad (6)$$

where  $n_{o_+}$  is the average ion number density when there are no double ions present. Since double ions are generally created from single ions, the specie conservation equation can be written as

$$n_{o_+} = n_+ + n_{++} \quad . \quad (7)$$

Defining the beam current correction factor  $\alpha$  as the ratio of the beam current when both species are present to the single ion beam current, one obtains

$$\alpha \equiv \frac{I_{B_{+,++}}}{I_{B_+}} = \frac{1 + 2\sqrt{2} n_{++}/n_+}{1 + n_{++}/n_+} \quad . \quad (8)$$

Where the relation  $v_{++} = \sqrt{2} v_+$ , which describes the relative velocity of double and single ions in the beam, has been used to simplify the results. Note that  $\alpha$  is given in terms of the ratio of double to single ions existing in the beam. In order to relate this ratio to the density ratio existing in the discharge chamber one must consider the continuity equation. Between two extraction grids one can neglect single and double ion production and the conservation of mass (or charge) of a given specie may be expressed as

$$\frac{\partial n}{\partial t} + \nabla \cdot (n\vec{v}) = 0 \quad . \quad (9)$$

For one-dimensional steady flow this reduces to

$$nv = \text{constant} \quad . \quad (10)$$

Applying the continuity equation to the single and double ions results in the relationship

$$\frac{n_{++}^* v_{++}^*}{n_+^* v_+^*} = \frac{n_{++} v_{++}}{n_+ v_+} , \quad (11)$$

where starred symbols refer to discharge chamber conditions at the screen grid and the remaining symbols to the beam conditions. The development of Appendix A shows that in the discharge chamber  $v_{++}^* = \sqrt{2} v_+^*$ . Using this result and the relation  $v_{++} = \sqrt{2} v_+$  the expression above becomes

$$\frac{n_{++}^*}{n_+^*} = \frac{n_{++}}{n_+} , \quad (12)$$

and this can be combined with Equation 8 to yield an equation for  $\alpha$  in terms of discharge chamber double ion fraction. Figure 31 presents a plot of the beam current correction factor as a function of the ratio of double to single ions existing in the discharge chamber.

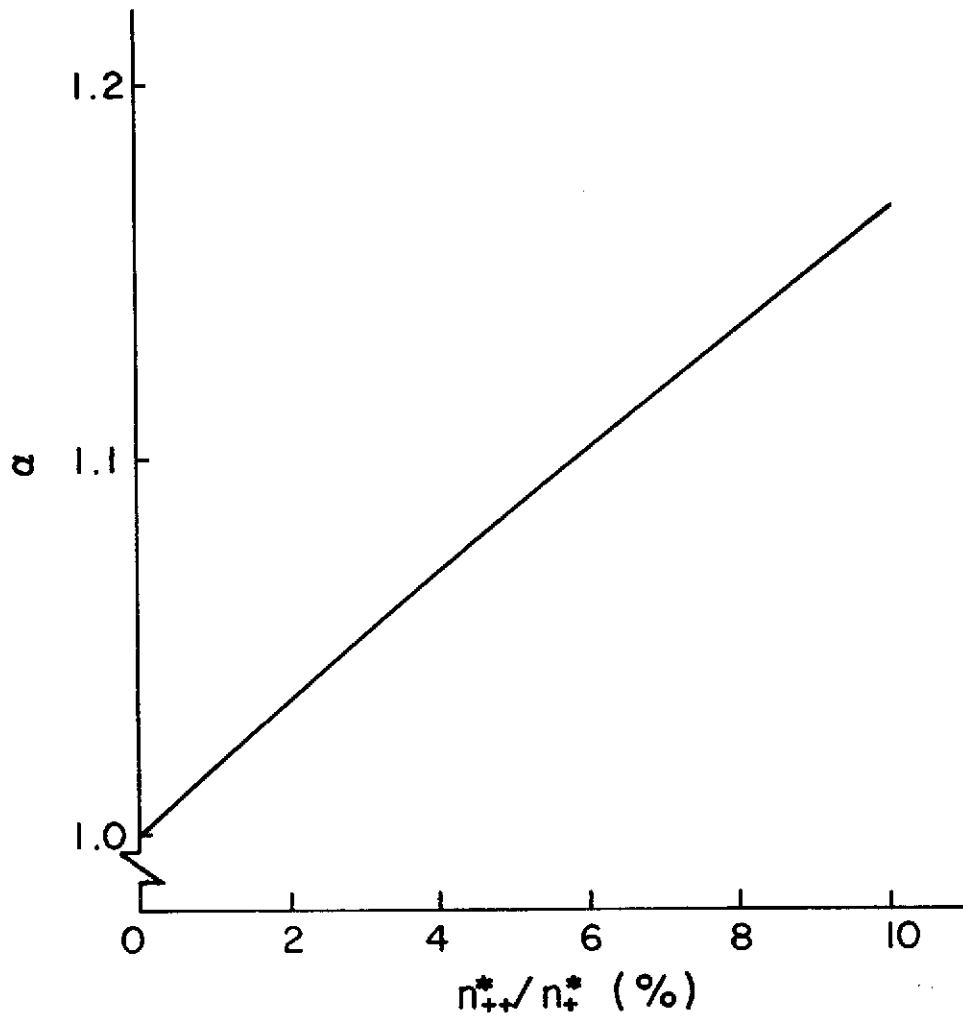
Since the measured beam current is used in the calculation of the discharge losses and the propellant utilization, both of these values will be affected by the presence of double ions. The discharge losses and propellant utilization calculated from the measured beam current can be corrected for the presence of double ions by the relation

$$P_{D_{\text{corrected}}} = \alpha P_D , \quad (13)$$

and

$$\eta_{u_{\text{corrected}}} = \frac{1}{\alpha} \eta_u . \quad (14)$$

From Figure 31 it is apparent that even relatively modest double ion fractions can significantly affect the calculated performance. For instance, if the beam contained 6% double ions the effect would be to increase the utilization and decrease the discharge losses by about 10%. Clearly, the presence of even small double ion fractions has the effect of flattening out the performance curve and the effect is more pronounced at higher propellant utilization efficiencies (i.e., larger double ion fractions).



BEAM CURRENT CORRECTION FACTOR

FIGURE 31

### The Effects of Reducing the Thruster Length

In Reference 2 it is shown that the baseline discharge losses are directly proportional to the ratio of the total area of the primary electron region to the open area of the screen grid. For a cylindrical primary electron region this ratio is given by

$$\frac{A_{\text{total}}}{A_{\text{open}}} = \frac{2\pi R^2 + 2\pi R d}{\pi R^2 \Omega} \quad , \quad (15)$$

where R is the thruster radius, d is the length of the primary electron region, and  $\Omega$  is the screen grid open area fraction. For the CMF thruster a 50% reduction in the length d would reduce the area ratio about 27%. One could then expect a similar reduction in the baseline discharge losses. Decreasing d also reduces the magnetic field fringing between the front and center magnet pole pieces which might be expected to improve the radial uniformity of the plasma density thereby improving ion beam flatness.

It is shown on page 72 that the production of double ions by both primary and Maxwellian electrons is a strong function of the volume to surface area ratio of the primary electron region. That this is an important parameter can be explained on the basis that the production of ions is proportional to the volume of the region while the loss of ions is related to the surface area confining this volume. For a cylindrical region this ratio becomes

$$\frac{V}{A_{\text{total}}} = \frac{\pi R^2 d}{2\pi R^2 + 2\pi R d} \quad (16)$$

For the CMF thruster a 50% reduction in d would reduce the volume to surface area ratio about 30%. A significant reduction in the presence of double ions would then be expected as a result.

### Conclusions

The addition of a center magnet pole piece and a porous screen rear anode to a standard SERT II discharge chamber has produced a

thruster whose operation is very stable over a wide range of propellant utilization. The thruster can be throttled at least over a 2 to 1 range in total propellant flow rate at a cost of 50 ev/ion at 85% utilization. However, the ion beam current density profile of this thruster has been improved only slightly and the baseline discharge losses are significantly higher than those of the SERT II thruster. The typical high flow rate performance curve for this thruster design is essentially linear and propellant utilization efficiencies of over 100% are easily obtained.

As a result of the experimental studies conducted on the CMF thruster, a fairly comprehensive discharge chamber theory has evolved. The theory seems to explain adequately the performance characteristics of the thruster in terms of the substantial probability for ions produced in the magnetic bottle formed at the rear of the discharge chamber to either be lost to the anode or to become doubly ionized. This high probability is directly related to the length of the discharge chamber and the theory developed would predict that shortening the distance between the ion source and extraction grids would reduce both the production of double ions and ion recombination on the anode surface. This in turn should result in reduced discharge losses and a more uniform ion beam profile.

THE PENNING IONIZATION MECHANISM IN AN  
ELECTRON-BOMBARDMENT ION THRUSTER

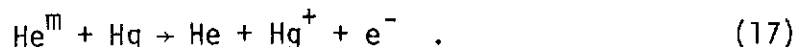
(J. Graf)

Introduction

Large increases in the ionization rate of a given atomic specie can be effected through the addition of a second specie which has a metastable level above the ionization potential of the first. This phenomenon is known as the Penning effect, and ionization is effected by a metastable specie two atom which collides with a specie one atom to produce a specie one ion and a ground state specie two atom. Since argon and helium have metastable levels above the ionization potential of mercury a collision between either argon or helium metastables and a mercury atom should theoretically result in a mercury ion. Since the cross section for this reaction is of order  $10^{-14}$  cm<sup>2</sup>, which is two orders of magnitude above the cross section for mercury ion production by electron bombardment, it was hoped the Penning interaction would supplement mercury ion production by electron bombardment and hence increase the ion production rate significantly.

Theory

During the Penning interaction in a mercury bombardment thruster, an excited helium or argon atom for example transfers its energy to the mercury atom. The amount of energy transferred (19.8 ev for helium and 11.53 ev for argon) is higher than the first ionization potential of the mercury (10.43 ev) and so ionization is possible. For the case of helium which will be used as an example here because of the availability of cross section data the process is described by



The metastable state is one which does not readily radiate to ground level via emission of a quanta of radiation and it therefore has

a long radiative lifetime (on the order of  $10^{-1}$  sec). If the time for Penning interaction were much less, then this would be the dominant de-excitation mode. For helium this interaction time is defined by the equation

$$t_i = \frac{\lambda_{\text{Penning}}}{v_{\text{He}}} = \frac{1}{n_{\text{Hg}} \sigma v_{\text{He}}}, \quad (18)$$

where  $\lambda_{\text{Penning}}$  is the mean free path for the Penning interaction,  $v_{\text{He}}$  is the helium velocity,  $n_{\text{Hg}}$  is the mercury density and  $\sigma$  is the Penning cross section. Using the average thermal velocity of helium at 500°K, a Penning cross section of  $1.4 \times 10^{-14}$  cm<sup>2</sup> and a mercury density of  $10^{18}$  atom/m<sup>3</sup> the interaction time,  $t_i$  is  $4.4 \times 10^{-4}$  sec. Thus, during its existence, the metastable has a high probability to collide with and ionize a mercury neutral.

To estimate the effect of the metastable helium on the mercury ion population, one must first calculate the metastable density. The steady state, metastable mass balance for an elemental volume in the plasma is

$$\begin{aligned} \text{Creation} & \qquad \qquad \qquad \text{Destruction} \\ \alpha_1 n_{\text{He}} n_e + \beta_1 n_{\text{He}}^{\text{excit}} &= \alpha_3 n_{\text{Hg}} n_{\text{He}}^m + \alpha_4 n_{\text{Hg}}^+ n_{\text{He}}^m \\ & \qquad \qquad \qquad + \alpha_5 n_{\text{He}} n_{\text{He}}^m + \alpha_6 n_{\text{He}}^m n_{\text{He}}^m \\ & \qquad \qquad \qquad + \alpha_7 n_e n_{\text{He}}^m + \beta_2 n_{\text{He}}^m \end{aligned} \quad (19)$$

$\alpha_1$  = rate coefficient for neutral helium-electron collision

$\alpha_3$  = rate coefficient for metastable helium-mercury atom collision

$\alpha_4$  = rate coefficient for metastable helium-mercury ion collision

$\alpha_5$  = rate coefficient for metastable helium-helium atom collision

$\alpha_6$  = rate coefficient for metastable helium-helium metastable collision

$\alpha_7$  = rate coefficient for metastable helium-electron collision

$\beta_1$  = rate coefficient for metastable helium production from excited states

$\beta_2$  = rate coefficient for metastable helium-wall collision

Most work done on the production of metastable helium has combined the cross section of excitation due to direct electron bombardment with that due to step-wise metastable production from a higher energy state. Thus, rate coefficients  $\alpha_1$  and  $\beta_1$  can be combined into a third coefficient,  $\alpha_2$ , the rate coefficient for total metastable production

$$\alpha_1 n_{\text{He}} n_e + \beta_1 n_{\text{He}}^{\text{excit}} = \alpha_2 n_{\text{He}} n_e \quad (20)$$

(The coefficient  $\beta_1$  is a function of electron density since the neutral helium is excited initially by electron impact.)

Assuming an infinite plasma, one can neglect de-excitation due to the presence of the wall ( $\beta_2 = 0$ ). This is not strictly valid as the Penning interaction length is on the order of the thruster dimension, approximately 0.71 meters/collision. For this preliminary study, however, the above assumption will be retained. In order to estimate the mercury production rate from metastable interactions an electron and ion density of  $10^{17} \text{ m}^{-3}$  and a neutral mercury density of  $10^{18} \text{ m}^{-3}$  will be assumed.

Figure 32, taken from Massey and Burhop<sup>15</sup>, shows that the maximum cross section for production of  $2^3\text{S}$  helium metastables (19.8 ev) occurs at an electron energy of about 40 ev--approximately the energy of a primary electron in the thruster chamber. Helium has another metastable level,  $2^1\text{S}$ , at 20.6 ev, which, according to Biondi<sup>16</sup>, decays rapidly, via electron collision, to the  $2^3\text{S}$  state

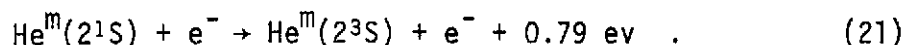
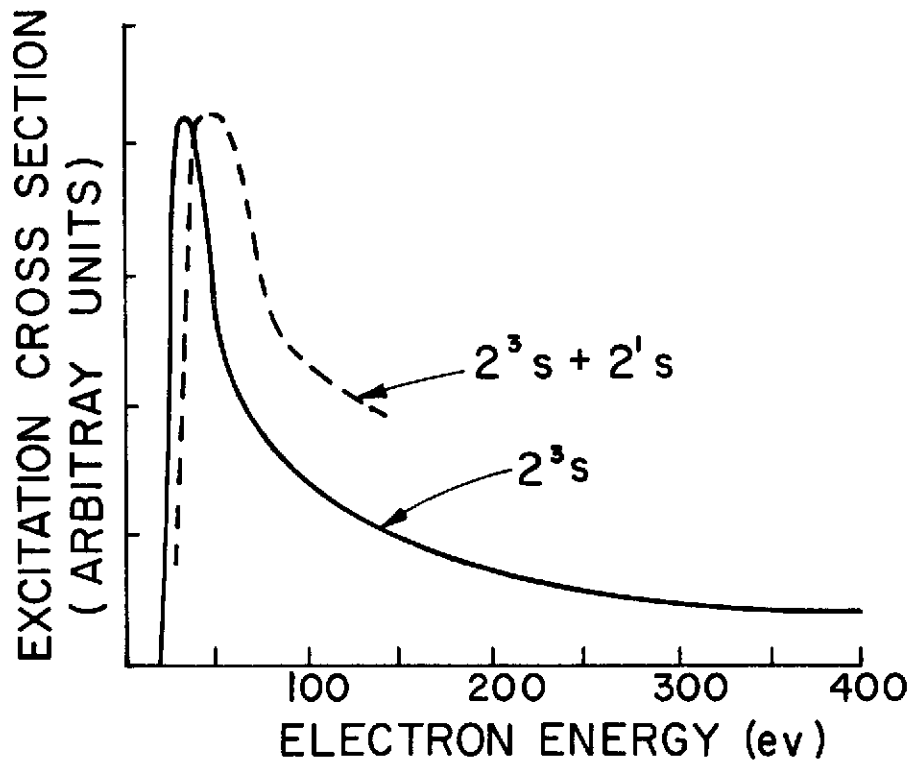


Figure 32 also shows that the production of the  $2^1\text{S}$  metastable is not at a maximum at the thruster operating voltage. For these two reasons, the assumption will be made that only the  $2^3\text{S}$  (19.8 ev) metastables need be considered. The maximum numerical experimental cross section ( $\alpha_2$ ) associated with Figure 32 was determined initially by Maier-Leibnitz<sup>17</sup> and found to be  $5 \times 10^{-18} \text{ cm}^2$ . Other experimenters found the cross section to be  $4(\pm 3) \times 10^{-18} \text{ cm}^2$  (Schultz and Fox<sup>18</sup>),



HELIUM METASTABLE PRODUCTION CROSS SECTIONS

FIGURE 32

$2.6(\pm 0.4) \times 10^{-18} \text{ cm}^2$  (Fleming and Higginson<sup>19</sup>) and  $3(\pm 0.7) \times 10^{-18} \text{ cm}^2$  (Holt and Krotkov<sup>20</sup>). The order of magnitude agreement is sufficient for this rough analysis.

The neutral helium density in the discharge chamber,  $n_{\text{He}}$  can be calculated from simple kinetic theory, assuming helium is lost through the thruster grid system at the supply rate and that the loss rate is determined by the sharp edged orifice expression for free molecular flow

$$n_{\text{He}} = \frac{4\dot{m}_{\text{He}}}{\bar{v}_0 A} \quad (22)$$

$\dot{m}_{\text{He}}$ , the helium atom flow rate is assumed to be 100 ma equivalent ( $6.25 \times 10^{17}$  atom/sec) and  $A$ , the open area of a SERT II grid system, is  $.0124 \text{ m}^2$ . the average velocity of the neutral helium,  $\bar{v}_0$ , is given by the kinetic theory expression which at the thruster temperature of  $500^\circ\text{K}$  has the indicated numerical value.

$$\bar{v}_0 = \sqrt{\frac{8kT}{\pi m_{\text{He}}}} = 1.63 \times 10^3 \text{ m/sec} \quad (23)$$

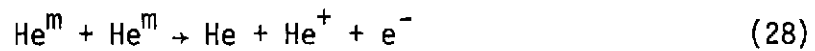
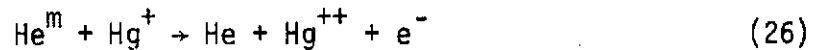
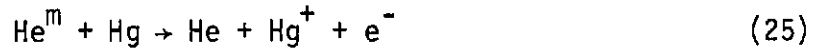
Substituting these values into Equation 22, the neutral helium density is determined to be  $1.24 \times 10^{17} \text{ m}^{-3}$ .

The rate coefficients ( $\alpha$ ) are defined to be the product of the associated cross section and the relative velocity of two colliding species,  $v_r$ , which for the case of a colliding electron and heavy particle is essentially the electron velocity. The relative velocity between two heavy particles can be determined from the equation<sup>21</sup>

$$v_r = \sqrt{\frac{8kT}{\pi m^*}} \quad (24)$$

where  $m^*$  is the reduced mass. It has been shown previously that the maximum production of  $2^3\text{S}$  metastables occurs at about 40 ev. Thus, for this rough analysis the electron energy will be assumed to be 40 ev where the electron velocity is  $3.75 \times 10^6 \text{ m/sec}$ . This corresponds to a rate coefficient for metastable production,  $\alpha_2$ , of  $1.875 \times 10^{-15} \text{ m}^3/\text{sec}$ .

The right hand or destruction side of Equation 19 is much more complicated. Metastable helium can be destroyed by collisions with mercury neutrals and ions, helium neutrals and metastables and electrons in accordance with the following equations:



The cross section for the Penning effect coefficient,  $\alpha_3$ , has been determined by Biondi<sup>16</sup> to be  $1.4(\pm 0.3) \times 10^{-14} \text{ cm}^2$ . The author has found no mention of process 26 in the literature; theoretically however the 19.8 ev metastable should be capable of ionizing the mercury a second time (18.75 ev ionization potential). Thus, for this rough analysis, the cross section will be assumed to be that of process 25, ( $\sigma_4 = 1.4(\pm 0.3) \times 10^{-14} \text{ cm}^2$ ).

The cross section for helium neutral and metastable collisions is small, partly due to excitation transfer, i.e., a metastable atom transferring energy directly to another atom without radiative losses. Biondi<sup>16</sup> calculated a value of  $9.6(\pm 0.1) \times 10^{-21} \text{ cm}^2$  but it is not believed that this is the 2<sup>1</sup>S metastable neutral cross section. Allison et al<sup>22</sup> repeated the calculation for 2<sup>3</sup>S metastables and found  $\sigma_5 = 2 \times 10^{-20} \text{ cm}^2$ .

Much work has been done on the metastable - metastable cross section and they agree on the order of magnitude,  $10^{-14} \text{ cm}^2$ . Specifically, the value found by Hurt<sup>23</sup> was  $\sigma_6 = 1.2 \times 10^{-14} \text{ cm}^2$ . This value, although of the order of  $\sigma_3$ , will not have a large effect in the chamber due to the low helium metastable density compared to that of mercury. However, much energy could be lost in the region of metastable production due to this

process. Geometries which spread out the metastable production region may prove to lower this loss if, in fact, it is significant.

The final process, metastable de-excitation by electron collision can, according to Loeb<sup>24</sup>, result in a helium neutral or ion. Bates et al<sup>25</sup> calculated this interaction coefficient by inverting the Schultz-Fox<sup>18</sup> curve for the 2<sup>3</sup>S metastable production. The coefficient was found to be  $\alpha_7 = 8.4 \times 10^{-16} \text{ m}^3/\text{sec}$ .

Using these cross sections and heavy particle velocities corresponding to a wall temperature of 500°K one calculates the following rate coefficients:

$$\alpha_3 = 2.3 \times 10^{-15} \text{ m}^3/\text{sec}$$

$$\alpha_4 = 2.3 \times 10^{-15} \text{ m}^3/\text{sec}$$

$$\alpha_5 = 4.6 \times 10^{-21} \text{ m}^3/\text{sec}$$

$$\alpha_6 = 2.75 \times 10^{-15} \text{ m}^3/\text{sec}$$

$$\alpha_7 = 8.4 \times 10^{-16} \text{ m}^3/\text{sec}$$

Collecting the interaction coefficients and the various densities, substituting into Equation 19 and solving the resulting quadratic, the helium metastable density was found to be  $n_{\text{He}}^{\text{m}} = 8.81 \times 10^{15} \text{ m}^{-3}$ . Thus, the metastable density is two orders of magnitude below the neutral helium density. When combined with the neutral mercury density and the Penning coefficient,  $\alpha_3$ , the mercury ion production rate due to helium metastables is  $\alpha_3 n_{\text{He}}^{\text{m}} n_{\text{Hg}} = 2.03 \times 10^{19} \text{ m}^{-3} \text{ sec}^{-1}$ .

When this rate is compared to the neutral mercury-electron interaction ion rate at 40 ev, it is found to be three orders of magnitude lower, namely,

$$\alpha_8 n_{\text{Hg}} n_e = 2.25 \times 10^{22} \text{ m}^{-3} \text{ sec}^{-1}.$$

Remembering that this analysis did not include the interaction of the metastables and the wall, one concludes the metastables should have little effect on the rate of ion production. For the metastable

produced ions to have an effect the Penning production rate must be of the order of the mercury-electron production rate. This implies a helium mass flow rate that is four orders of magnitude higher ( $\dot{m}_{\text{He}} = 1.02 \times 10^6 \text{ ma}$ ).

### Experiment

To confirm the preceding theory, a Kaufman thruster was modified to permit the introduction of the seeding gas through the hollow cathode. When helium was used, high cathode flow rates ( $> 1 \text{ amp eq.}$ ) were required to sustain the keeper discharge. In addition, the discharge was found to be unstable and shorting was observed between the grids. (The shorting was a result of high test chamber pressure due to the high helium flows.) As there was great difficulty in sustaining the arc discharge, no reliable data could be recorded.

When argon was used rather than helium, the thruster operation was found to be stable. The argon flow rate was also very high ( $> 1 \text{ amp eq.}$ ) and any attempt to reduce it extinguished the arc. This resulted of course in poor utilization efficiency, and the observed baseline discharge power of 316 ev/ion was greater than that observed with no argon flow.

Since the above configuration did not provide any satisfactory results, a third feed tube was installed to facilitate helium or argon distribution with the main mercury flow, throughout the discharge chamber. The cathode operated on its own independent mercury reservoir and this design permitted accurate measurement of all flows. With this configuration, stable thruster operation could be established and the Penning gas could then be introduced in amounts from trace flow rates up to a few amps equivalent. The test results and performance data obtained with argon are shown in Table II while those obtained with helium are presented in Table III. The utilization efficiency was calculated using the sum of the Penning gas flow and both mercury flows.

### Conclusion

The results displayed in Tables II and III show no improvement in the performance characteristics of the thruster when either helium or argon are introduced into the discharge chamber. This confirms the theoretical prediction that the metastables have no substantial effect upon the mercury ion population.

Table II

Mercury-Argon Operating Conditions and Performance Data

Mercury Flow Rates Cathode - 30 ma Main -700 ma	Keeper Current 0.3 a				
	Run Number	1	2	3	4
Argon Flow Rate (ma)	0	57.8	422	>870	>870
Arc Current (a)	4.27	4.25	4.26	4.20	4.25
Arc Voltage (v)	37.7	38.5	37.9	38.3	38.1
Keeper Voltage (v)	11.2	11.4	11.3	11.4	11.1
Beam Current (ma)	609	609	614	610	628
Impingement Current (ma)	2.4	2.4	2.4	2.4	2.5
Beam Ion Cost (ev/ion)	269.8	274.2	268.5	269.3	263.1
Propellant Utilization (%)	83	77	53	--	--

Table III

Mercury-Helium Operation Conditions and Performance Data

Mercury Flow Rates Cathode - 30 ma Main -700 ma	Keeper Current - 0.3 a				
	Run Number	1	2	3	4
Helium Flow Rate (ma)	0	82.2	233	500	>10 <sup>3</sup>
Arc Current (a)	4.22	4.24	4.24	4.23	4.24
Arc Voltage (v)	38.8	38.9	38.9	38.9	38.9
Keeper Voltage (v)	11.8	11.9	11.9	11.9	11.8
Beam Current (ma)	609	616	615	615	617
Impingement Current (ma)	2.6	2.6	2.6	2.6	2.6
Beam Ion Cost (ev/ion)	274.7	273.5	274.0	273.4	273.1
Propellant Utilization (%)	83	76	64	50	--

DOUBLE ION PRODUCTION IN MERCURY  
ELECTRON-BOMBARDMENT THRUSTERS

Introduction

Up until the past few years concentrations of doubly ionized mercury in electron bombardment ion thrusters were considered small when primary electron energies were below about 35 ev because of the relatively low cross sections for double ionization of neutral mercury at these energies<sup>26</sup>. Subsequently investigation of plasma within thrusters have included spectroscopic and mass spectrometer measurements which suggest the double ion densities are considerably higher at these low energies than analysis based on this reaction would suggest<sup>27,28</sup>. An alternative reaction which might account for the higher than anticipated double ion densities is



This reaction can be significant in mercury bombardment thrusters if the singly charged ion densities are sufficiently high. Bombarding electrons which could be important in this reaction are the monoenergetic primary electrons and those with a Maxwellian energy distribution. If one assumes ionization from various excited states is negligible double ion concentrations resulting from the above reaction as well as direct double ionization of neutral mercury can be calculated and the results can be compared with experimental measurements.

Theory

Neglecting ionization of excited neutrals and volume recombination of double ions, the generation rate of single ions  $R_g^+$  in a volume  $V$  of uniform atomic density  $n_o$ , Maxwellian electron density  $n_m$  and distribution function  $f(E)$ , and primary electron density  $n_p$  and energy  $\xi_p$  is given by

$$R_g^+ = n_o V \left[ n_p \sigma_o^+ (\xi_p) v_p(\xi_p) + \int_0^\infty 4\pi n_m \sigma_o^+ (E) f(E) c^3(E) dc \right], \quad (31)$$

where  $v_p = \sqrt{\frac{2\varepsilon_p}{m}}$  is the speed of primary electrons,  $c(E) = \sqrt{\frac{2E}{m}}$  is the speed of Maxwellian electrons at energy  $E$ , and  $\sigma_0^+(E)$  is the cross section for single ionization from the neutral ground state by an electron of this energy. The first and second terms of Equation 31 corresponds respectively to single ion production via primary electron bombardment and Maxwellian electron bombardment. The Maxwellian distribution function<sup>29</sup>  $f(E)$  is given by

$$f(E) = \left(\frac{m}{2\pi kT}\right)^{3/2} \exp\left(\frac{-E}{kT}\right), \quad (32)$$

where  $m$  and  $T$  are the electron mass and temperature and  $k$  is the Boltzmann constant.

Single ions are assumed lost from the volume only as a result of migration through the surface of area  $A$  which bounds the volume and through ionization to the doubly ionized state. Since double ionization is effected again by both primary and Maxwellian electrons the singly ionized ions loss rate  $R_\ell^+$  is given by the equation

$$R_\ell^+ = n_+ v_+ A + n_+ V \left\{ n_p \sigma_+^{++}(\varepsilon_p) v_p(\varepsilon_p) + \int_0^\infty 4\pi n_m f(E) \sigma_+^{++}(E) c^3(E) dE \right\} \quad (33)$$

where  $n_+$  is the single ion density,  $\sigma_+^{++}(E)$  is the cross section for double ionization from the singly ionized state by an electron of energy  $E$ , and  $v_+$  is the single ion velocity across the surface confining the plasma, determined by the modified Bohm criterion<sup>30</sup>. The fact that  $v_+$  is not altered because of the presence of the double ions in the plasma is discussed in Appendix A.

$$v_+ = \sqrt{\frac{kT}{m} \left(1 + \frac{n_p}{n_m}\right)} \quad (34)$$

In the steady state the production and loss rates are equal and one can therefore combine Equations 31 and 33 and solve for the single ion to neutral density ratio in terms of measured and calculable thruster parameters

$$\frac{n_+}{n_0} = \left\{ \frac{\frac{n_p}{n_m} \sigma_0^+(\xi_p) v_p(\xi_p) + \int_0^\infty 4\pi\sigma_0^+(E) f(E) c^3(E) dc}{\frac{v_+ A}{V n_m} + \frac{n_p}{n_m} \sigma_+^{++}(\xi_p) v_p(\xi_p) + \int_0^\infty 4\pi\sigma_+^{++}(E) f(E) c^3(E) dc} \right\} . \quad (35)$$

In a similar manner one can determine the double ion generation rate  $R_g^{++}$  due to both direct ionization of neutrals and ionization of single ions, by both primary and Maxwellian electrons.

$$R_g^{++} = n_0 V \left\{ n_p \sigma_0^{++}(\xi_p) v_p(\xi_p) + \int_0^\infty 4\pi n_m \sigma_0^{++}(E) f(E) c^3(E) dc \right\} \\ + n_+ V \left\{ n_p \sigma_+^{++}(\xi_p) v_p(\xi_p) + \int_0^\infty 4\pi \sigma_+^{++}(E) f(E) c^3(E) dc \right\} \quad (36)$$

The loss rate for double ions is assumed to be due only to migration across the bounding surface of area  $A$  and is given by

$$R_{\ell}^{++} = n_{++} v_{++} A . \quad (37)$$

The double ion velocity  $v_{++}$  necessary to assure a stable sheath is larger by the factor  $\sqrt{2}$  than that given by Equation 34 as discussed in Appendix A.

When Equations 32, 35, 36 and 37 are combined, an expression for the ratio of doubly ionized to neutral atoms can be obtained which is a function of atom and electron densities, temperatures and energies; the volume to surface area ratio of the plasma interaction region; and the cross sections for the various reactions. The following equation shows how these parameters appear in the final result; for simplicity Equation 32, the distribution function expression, has not been substituted.

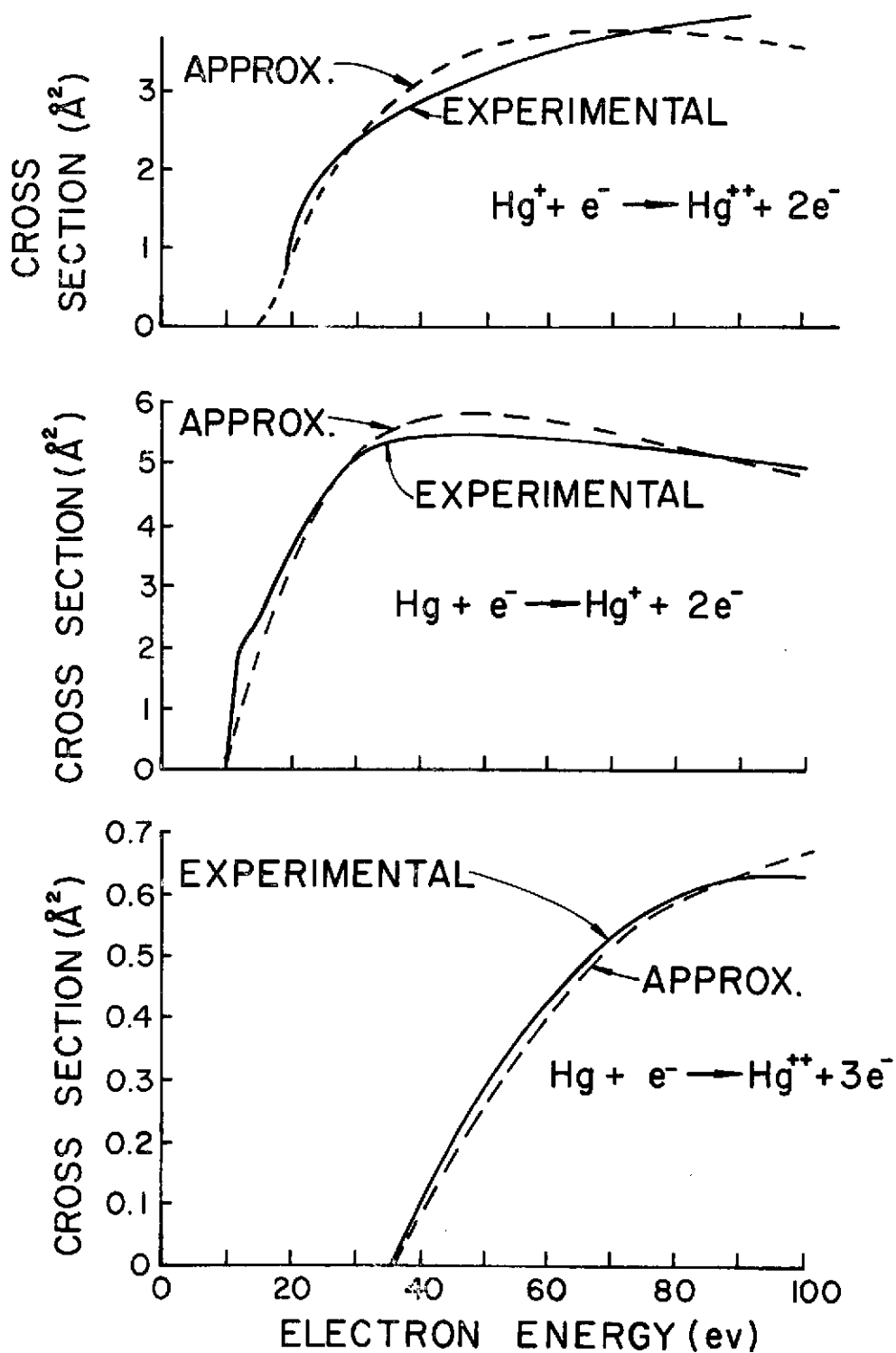
$$\frac{n_{++}}{n_0} = \frac{Vn_m}{Av_{++}} \left[ \frac{n_p}{n_m} \sigma_0^{++} v_p + \int_0^\infty 4\pi\sigma_0^{++} f c^3 dc + \right. \\ \left. \frac{\left\{ \frac{n_p}{n_m} \sigma_0^+ v_p + \int_0^\infty 4\pi\sigma_0^+ f c^3 dc \right\}}{\left\{ \frac{v_+ A}{Vn_m} + \frac{n_p}{n_m} \sigma_+^{++} v_p + \int_0^\infty 4\pi\sigma_+^{++} f c^3 dc \right\}} \left\{ \frac{n_p}{n_m} \sigma_+^{++} v_p + \int_0^\infty 4\pi\sigma_+^{++} f c^3 dc \right\} \right] \quad (38)$$

This equation can be solved readily on the computer once the cross section variation with electron energy is specified.

The experimental electron bombardment cross sections for the formation of single and doubly charged ions from neutral ground state mercury are available from References 26, 31 and 32, and those for ionization from the singly to doubly ionized state are given in References 33 and 34. These cross sections were approximated using a Gryzinski type expression and the extent of the agreement between these approximate cross sections and the measured ones is presented as Figure 33.

### Results

Figure 34 presents typical double ion concentrations determined from Equation 38 as a function of primary electron energy. The solid line represents what is considered a base operating condition with the volume to area ratio typical of a 30 cm dia. thruster. The other curves show the effect of varying the indicated parameter. Comparison of the dashed and solid lines shows for example a somewhat uniform reduction in double ion concentration occurs over the primary electron energy range when the Maxwellian electron temperature is reduced from 7 ev to 4 ev. The curve identified by a centerline corresponds to a 15 cm dia. thruster with otherwise similar conditions to those of the solid line. The smaller thruster is observed to exhibit much smaller double ion fractions than the 30 cm dia. one. This suggests why the presence of double ions in

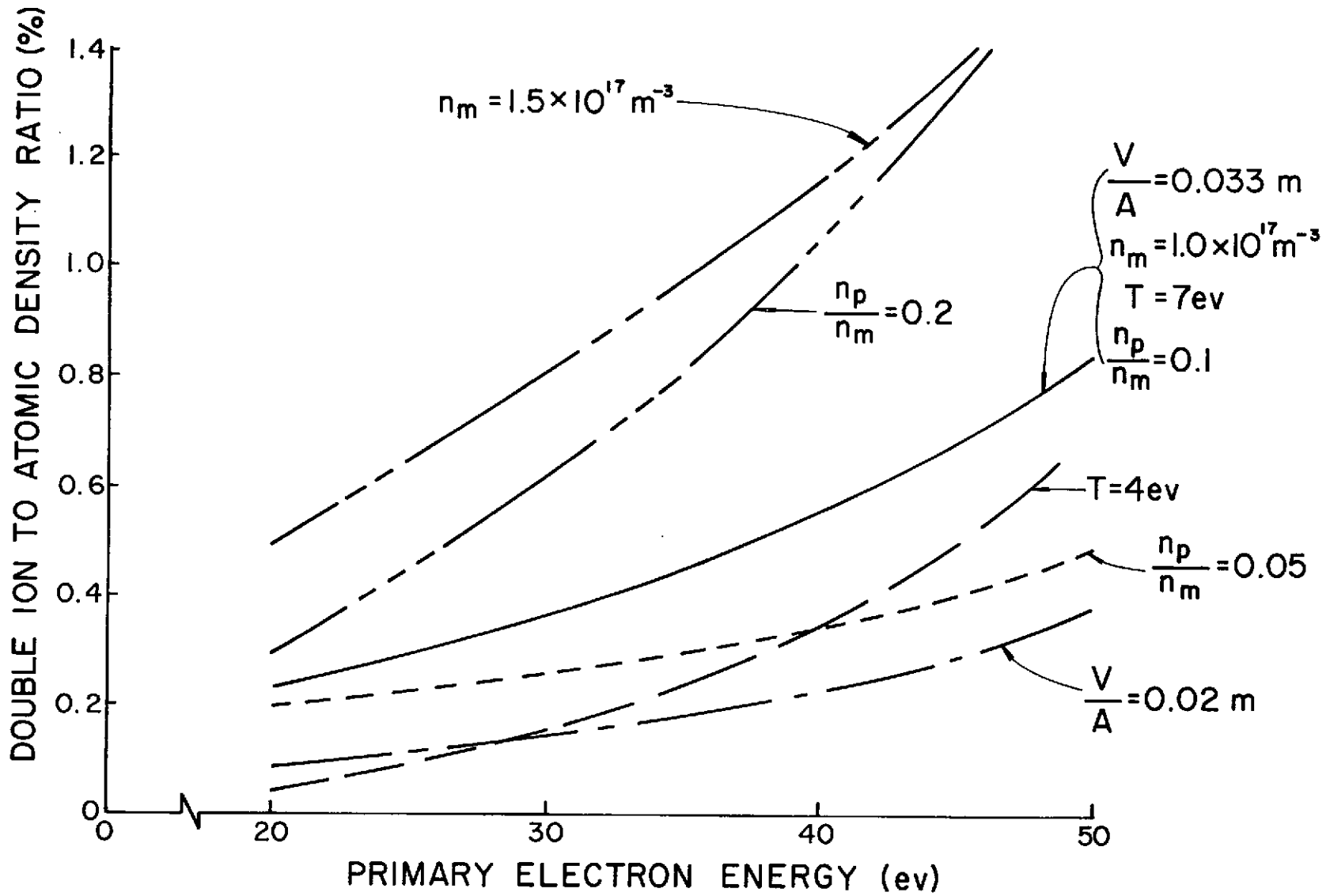


IONIZATION CROSS SECTIONS

FIGURE 33

FIGURE 34

THEORETICAL DOUBLE ION FRACTIONS



thrusters became much more evident recently when active development of larger thrusters began. One observes a variation in primary-to-Maxwellian electron density ratio results in a profound effect at high primary electron energies and as one might expect a smaller effect at energies at and below 20 ev. A 50% increase in Maxwellian and primary electron densities is observed to bring about a 100% increase in double ion fraction over the entire range of primary electron energies. A review of these results also shows that the dominant mechanism for production of double ions is the two step process involving ionization of singly ionized mercury into the doubly ionized state.

The concentration of single ions can be calculated from Equation 35. Results of this calculation are presented in Figure 35 for the same input parameters as Figure 34. The calculated single ion fractions are observed to fall into the range generally considered to be reasonable for thruster plasmas.

#### Comparison with Experimental Results

Milder and Sovey<sup>27</sup> have measured double ion fractions ( $n_{++}/n_0$ ) using a spectroscope on an operating 30 cm diameter ion thruster. Assuming the plasma properties suggested in their paper (Maxwellian electron density of  $10^{17} \text{ m}^{-3}$  and temperature of 7 ev and primary electron density of  $5 \times 10^{15} \text{ m}^{-3}$ ) and volume to surface area ratio appropriate to the 30 cm dia. thruster (0.033 m) their data lend themselves to direct comparison with results of this analysis. Figure 36 presents this comparison as a function of primary electron energy; the Milder-Sovey thruster center-line double ion fractions are shown as solid data symbols confined by error bars and the theoretical results are shown as the solid line. The significant discrepancy which is evident from this figure would be eliminated if the Maxwellian electron density were  $1.5 \times 10^{17} \text{ m}^{-3}$  and the primary to Maxwellian electron density ratio were increased to 0.15 as indicated by the dotted line. Such an adjustment of variables can be argued as necessary to bring the single ion to atomic density ratios

THEORETICAL SINGLE ION FRACTIONS  
 FIGURE 35

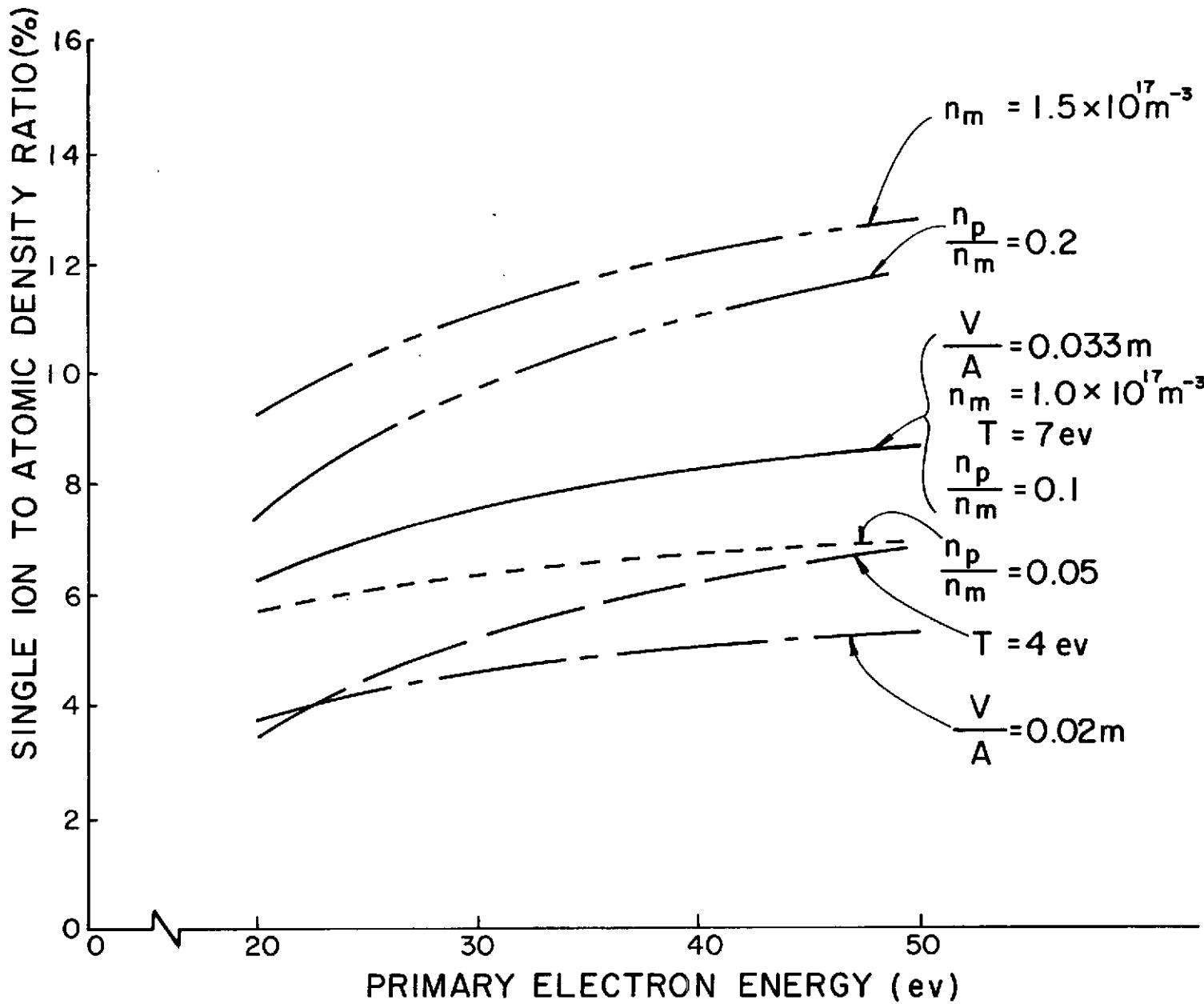
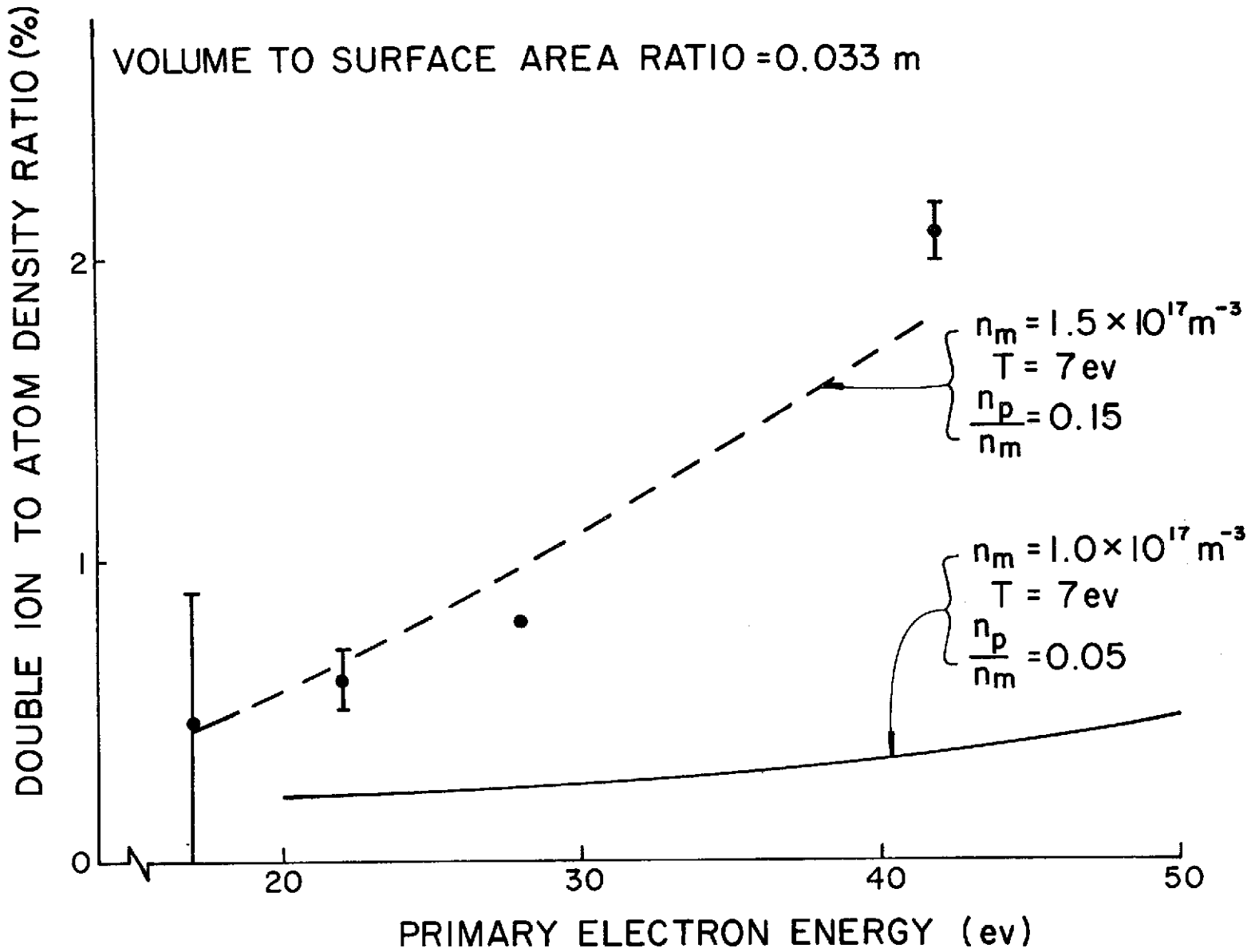


FIGURE 36

DOUBLE ION FRACTION - THEORY/EXPERIMENT COMPARISON



(Figure 35) nearer to the 10% values considered typical of ion thruster discharge chambers. Additional improvement in the agreement between these theoretical results and the data of Reference 27 may be possible if ionization routes through metastable and resonance excited atomic states are considered.

## THERMAL FLOW METER

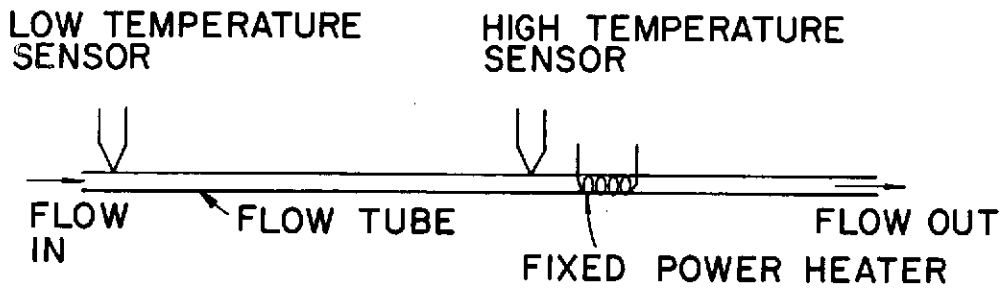
### Introduction

In the course of conducting experimental studies of mercury bombardment thrusters, considerable time is consumed in waiting to obtain accurate mercury flow rate information. In addition, mercury flow measurement techniques presently in use involve a measurement of mass or volume of mercury, and they therefore provide integrated flow rate information which implies an average flow rate. It is very difficult to determine flow rate trends from such information. These problems could be alleviated if a continuously indicating, accurate flow meter were available. The thermal flow meter described herein, which is based on the concept suggested by Laub<sup>35</sup>, does indicate mercury flow rates continuously over the range of interest for ion thruster testing with acceptable accuracy.

### Theory of Operation

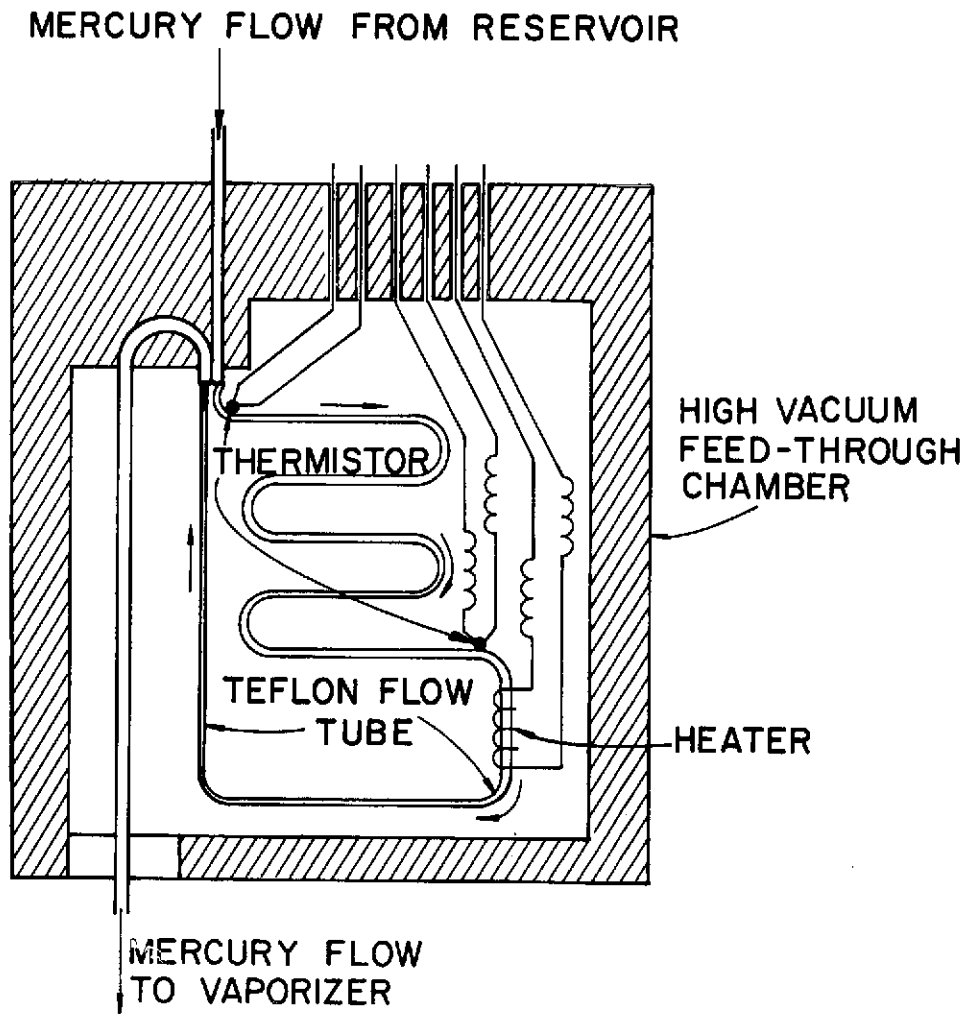
The basic concept on which this device operates is illustrated in Figure 37. As liquid mercury passes through the flow tube toward the vaporizer and thruster, it is heated slightly by the fixed power heater. Mercury entering and leaving the flow meter is maintained at ambient temperature by a heat sink. The proximity of the high temperature sensor to the heater and the fact that the temperatures at opposite ends of the tube are held at ambient values implies a temperature difference between the two sensors shown in the figure. These sensors (thermistors) are connected into a bridge circuit which exhibits an output proportional to the temperature difference which they sense, and this output can be related to flow rate.

A simple one-dimensional theoretical model of this flow meter concept has been developed<sup>2</sup>, and it has been used to design such a device. The flow meter, described previously in Reference 2, consists of a 0.3 mm i.d. teflon flow tube fitted with a 60 milliwatt heater and 1.1 mm dia. glass bead, 10 K $\Omega$  thermistors all of which is enclosed in a vacuum isolation chamber. The flow tube is fitted within a vacuum feed-through



THERMAL FLOW METER SCHEMATIC

FIGURE 37



FLOW METER CONCEPTUAL ARRANGEMENT

FIGURE 38

in the manner suggested by Figure 38.

The output from the device is obtained through the basic bridge circuit shown as Figure 39. Initial tests were made with 6.8 K $\Omega$  resistors as the components  $R'_{ref}$  in this figure, and it was observed that the output of the device drifted with ambient temperature fluctuations. The reason for this may be understood by considering the following:

1) The resistance of a thermistor may be assumed to vary with temperature in accordance with the equation

$$R = R_0 e^{-\alpha T} \quad (39)$$

where  $R_0$  and  $\alpha$  are constants. Hence the resistance  $R_{ref}$  at an ambient temperature  $T_a$  is

$$R_{ref} = R_0 e^{-\alpha T_a} \quad (40)$$

and the resistance  $R_{meas}$  some  $\Delta$  degrees hotter than  $T_a$  is

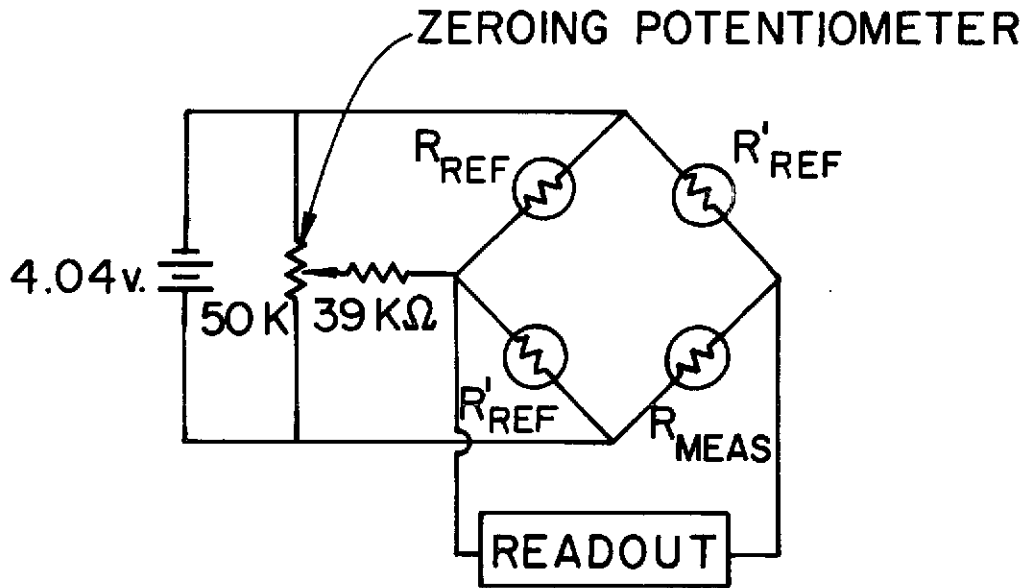
$$R_{meas} = R_0 e^{-\alpha(T_a + \Delta)} \quad (41)$$

2) The output of the bridge circuit is given to first order by the equation:

$$\frac{E_{out}}{E_{battery}} = \frac{R_{ref}}{R_{ref} + R'_{ref}} - \frac{R'_{ref}}{R_{meas} + R'_{ref}} \quad (42)$$

3) Substitution of Equations 40 and 41 into 42 yields an expression for output voltage ( $E_{out}$ ) which is a function of  $T_a$  for  $R'_{ref}$  constant. This implies the observed drift.

If one substitutes thermistors which sense the ambient temperature for the resistors  $R'_{ref}$ , and if all four thermistors are assumed to be identical ( $R_0$  and  $\alpha$  identical for each) then the combination of Equations 40, 41 and 42 yields



FLOW METER BRIDGE CIRCUIT SCHEMATIC

FIGURE 39

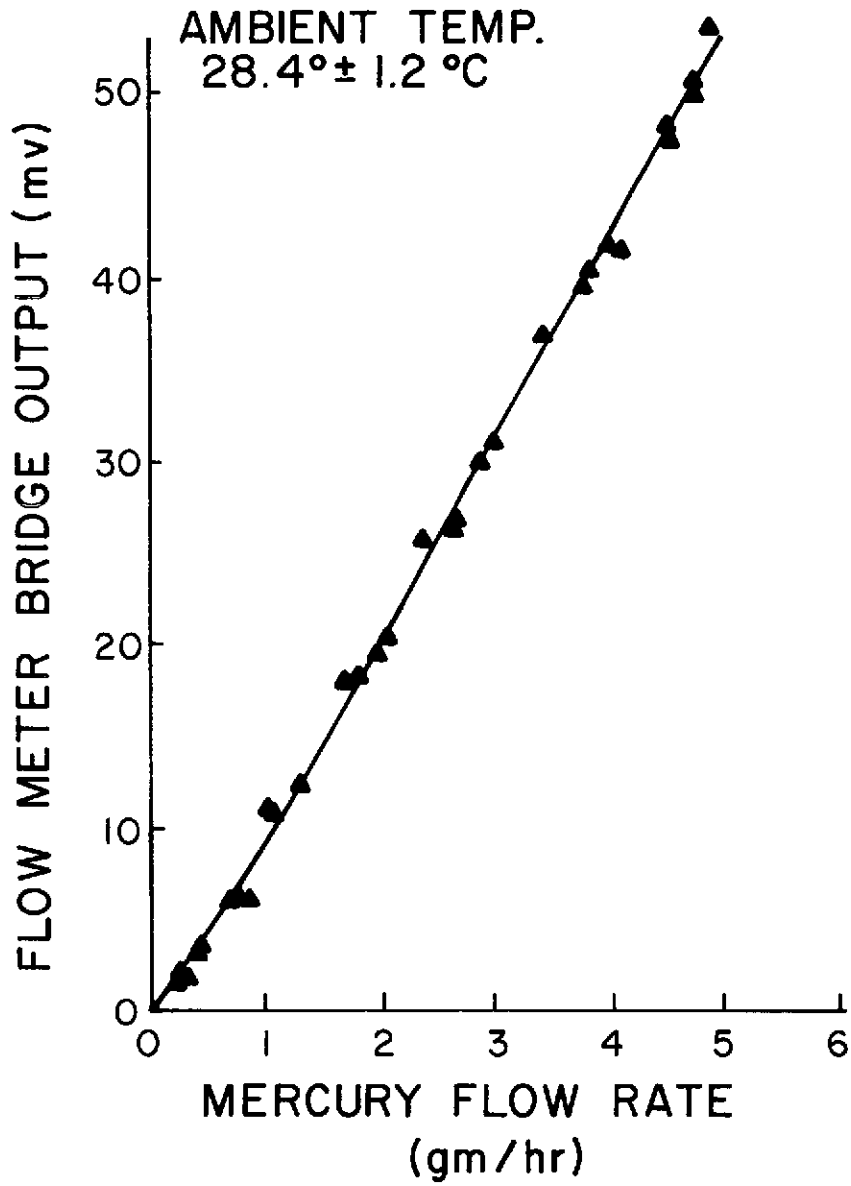
$$\frac{E_{\text{out}}}{E_{\text{battery}}} = \frac{1}{2} - \frac{1}{1 + e^{-\alpha\Delta}} \quad . \quad (43)$$

This equation is independent of  $T_a$  and hence no drift should be observed. Substitution of thermistors into the bridge circuit for the  $R'_{\text{ref}}$  components in the experimental system did result in a reduction in drift, but it did not eliminate it completely. Presently four matched thermistors are being purchased to eliminate possible drift because of variation in the constants  $R_0$  and  $\alpha$  among the thermistors.

### Experimental Performance

The flow meter using unmatched thermistors has been calibrated by installing it in the line between a 0.9 mm dia. bore glass flow tube and the main vaporizer of a thruster and measuring the time required for the mercury meniscus to fall between two scribe marks confining a known volume of mercury while the flow meter output remained essentially constant. The resulting calibration curve for the thermal flow meter is presented as Figure 40. It shows a nearly constant sensitivity of about 10 mv/gm/hr over a 0.2 to 5.0 gm/hr flow rate range, and it appears higher flow rates could be measured. It is apparent from the curve that the flow meter performs well at somewhat higher flow rates than had been considered in the initial design. This suggests the conduction through the mercury may be higher than had been anticipated and that the somewhat higher mercury flow velocities are necessary to achieve significant convection alterations of the otherwise linear conduction temperature profile. By increasing the sensitivity of the readout equipment the flow meter appears to perform satisfactorily at low flow rates (< 0.3 gm/hr.). The scatter in the data points of Figure 40 is considered to be due to variations in ambient temperature and scatter in flow rate measurements obtained from the flow tube.

The linear relationship between flow rate and bridge output voltage shown in Figure 40 is noteworthy. It occurs because the mercury temperature near the flow meter heater is inversely proportional to flow rate



FLOW METER CALIBRATION CURVE

FIGURE 40

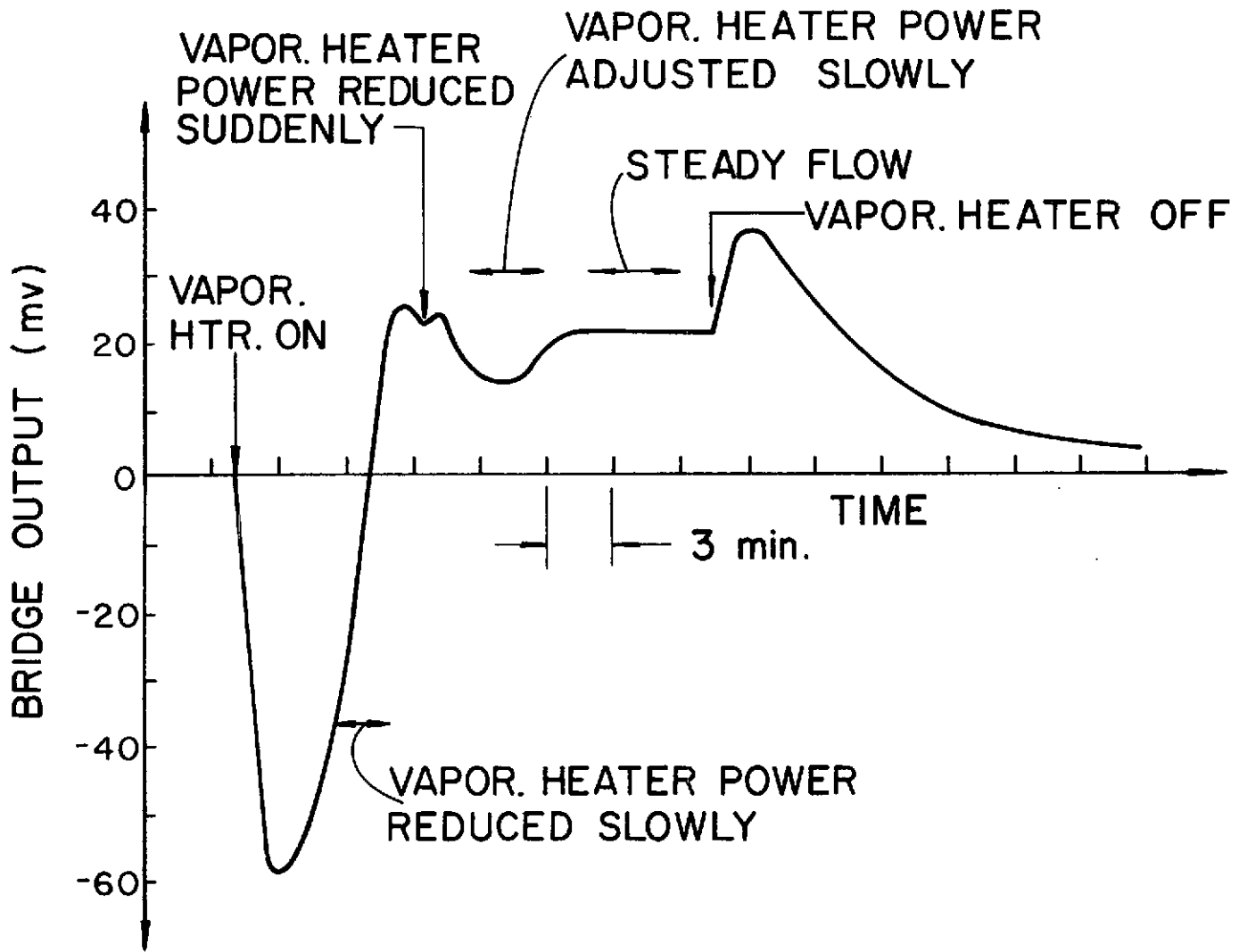
while the bridge output (Equation 43) can be set up so, to first order, its output is inversely proportional to temperature. These facts combine to effect a bridge output which is directly proportional to flow rate.

Several months of operating experience with the flow meter have demonstrated that it is very useful as a tool for indicating flow rate trends. This usefulness is illustrated in Figure 41 which displays flow meter output as a function of time for a flow rate initiation - stabilization - termination cycle. After the flow meter heater had been allowed to stabilize and the zeroing potentiometer (Figure 39) had been adjusted to indicate zero output at the existing no-flow condition, the vaporizer was energized. The figure shows a large negative flow rate associated with expansion of the mercury occurs immediately after the vaporizer heater is energized. This is followed by the establishment of a positive flow rate about six minutes after vaporizer energization. After a period of vaporizer heater current adjustment which was necessary to achieve the desired flow rate, stabilization at a steady flow rate is observed (about 15 minutes after vaporizer heatup began). Because of the one minute time constant associated with the flow meter, the indicated flow rate is in good quantitative agreement with the true flow rate only in this steady state region. When the vaporizer heater is de-energized an increase in flow rate, associated with contraction of the mercury as it cools, is observed. Subsequently the output drops to zero exponentially as the flow meter temperatures stabilize back to their no-flow values.

Figure 42 displays flow meter output as a function of time while the thruster is operating. Two interesting details are apparent from this figure. They are: 1) the tiny blip identified with high voltage arcing which is observed occasionally and 2) the increase in flow rate observed when the level of mercury is raised in the flow tube thereby increasing the pressure in the feed system. These are interesting because they indicate 1) normal high voltage arcing does not disrupt

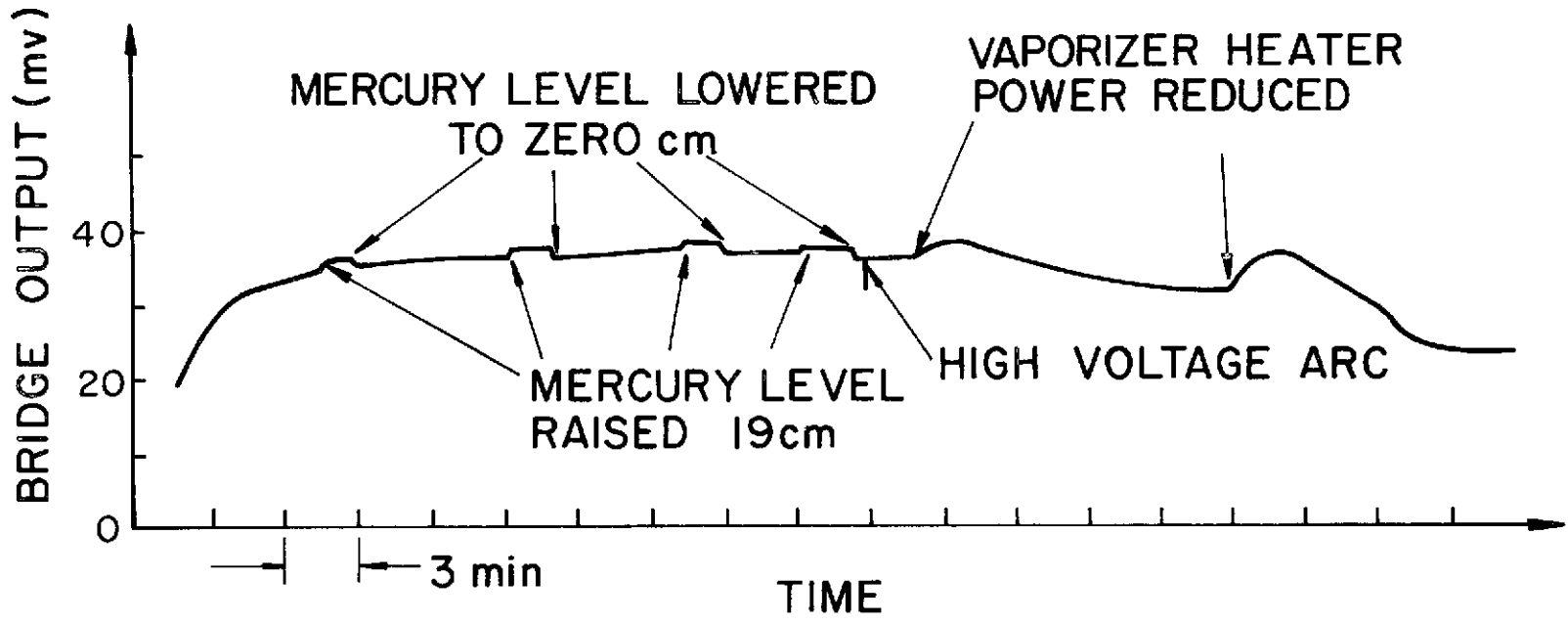
TYPICAL FLOW METER OUTPUT OVER VAPORIZER HEATUP-COOLDOWN CYCLE

FIGURE 41



EFFECTS OF PRESSURE CHARGES AND HIGH VOLTAGE ARCING ON FLOW METER

FIGURE 42



flow meter operation significantly (no isolator was installed in the feed line for these tests) and 2) changes in the mercury supply pressure can alter the associated flow rate. This later phenomenon is considered to be a result of vapor at the liquid mercury-vaporizer interface which affects the rate of heat transfer to the mercury and hence its rate of vaporization and transfer through the porous vaporizer plate.

APPENDIX A

ION VELOCITIES TOWARD BOUNDARIES FOR PLASMAS  
CONTAINING DOUBLY CHARGED IONS

The basic Bohm criterion<sup>36</sup> which determines, in a Maxwellian plasma, the ion velocity necessary to assure a stable plasma sheath at a boundary has been modified by Masek<sup>30</sup> to account for the presence of a mono-energetic electron group in addition to the Maxwellian group. In view of the small but significant double ion concentrations being measured in ion thrusters it is appropriate to determine if any additional modification is needed to account for this.

The one-dimensional Poisson equation that applies in the sheath region is

$$\frac{d^2V}{dx^2} = 4\pi e(2n_{++}(x) + n_+(x) - n_m(x) - n_p(x)) \quad (A1)$$

where  $V$ , the negative of the potential in the sheath is taken as zero at the boundary,  $e$  is the electronic charge,  $x$  is the position variable, and  $n_{++}$ ,  $n_+$ ,  $n_m$  and  $n_p$  are the double ion, single ion, Maxwellian electron, and monoenergetic electron densities respectively. The Maxwellian and primary electron densities are given by<sup>30</sup>

$$n_m(x) = n_m(0) \exp\left(\frac{-eV}{kT}\right) \quad (A2)$$

$$n_p(x) = n_p(0) \left(1 - \frac{V}{E_p}\right) \quad (A3)$$

where  $n_m(0)$  and  $n_p(0)$  are the electron densities at the plasma-sheath interface,  $T$  is the Maxwellian group temperature,  $k$  is the Boltzmann constant and  $E_p$  is the monoenergetic group energy. The singly charged ion density, as in the original analysis<sup>36</sup>, is given by the expression for conservation of current density

$$n_+ = n_+(0) \left[ \frac{E_+}{E_+ + V} \right]^{1/2} \quad (A4)$$

where  $n_+(0)$  is the ion density at the plasma-sheath interface and  $E_+$  is the ion energy (in eV) at the interface. Similarly the double ion density is given by

$$n_{++} = n_{++}(0) \left[ \frac{E_{++}}{E_{++} + V} \right]^{1/2} \quad (A5)$$

where  $E_{++}$  represents the voltage through which the double ion fell to achieve the energy it has at the interface (multiplying  $E_+$  by twice the electronic charge yields the double ion energy).

Substituting Equations A2 through A5 into A1 one obtains

$$\begin{aligned} \frac{d^2V}{dx^2} = 4\pi e \left[ 2n_{++}(0) \left( \frac{E_{++}}{E_{++} + V} \right)^{1/2} + n_+(0) \left( \frac{E_+}{E_+ + V} \right)^{1/2} - n_m(0) \exp\left(\frac{-eV}{kT}\right) \right. \\ \left. - n_p(0) \left( 1 - \frac{V}{E_p} \right) \right]. \end{aligned} \quad (A6)$$

Multiplying Equation A6 by  $dV/dx$ , integrating and solving for the constant of integration to satisfy the boundary condition  $\frac{dV}{dx} = 0$  at  $V = 0$  yields

$$\begin{aligned} \left( \frac{dV}{dx} \right)^2 = 8\pi e \left[ 4n_{++}(0) E_{++} \left( \sqrt{1 + \frac{V}{E_{++}}} - 1 \right) + 2n_+(0) E_+ \left( \sqrt{1 + \frac{V}{E_+}} - 1 \right) \right. \\ \left. + n_m(0) \left( \frac{kT}{e} \right) \left( \exp\left(-\frac{eV}{kT}\right) - 1 \right) + n_p(0) \left( \frac{V^2}{2E_p} - V \right) \right]. \end{aligned} \quad (A7)$$

Near the plasma-sheath interface

$$\begin{aligned} \frac{V}{E_+} \ll 1, \quad \frac{V}{E_{++}} \ll 1 \\ V \ll \frac{kT}{e} \ll E_p. \end{aligned} \quad (A8)$$

The terms in Equation A7 pertaining to the ions and Maxwellian electrons may be expanded in a series and higher order terms, determined by Equations

A8 may be neglected and this equation becomes

$$\begin{aligned} \left(\frac{dV}{dx}\right)^2 \approx & 8\pi e \left[ 4n_{++}(0) E_{++} \left( \frac{V}{2E_{++}} - \frac{1}{8} \left[ \frac{V}{E_{++}} \right]^2 \right) + 2n_+(0) E_+ \left( \frac{V}{2E_+} - \frac{1}{8} \left[ \frac{V}{E_+} \right]^2 \right) \right. \\ & \left. + \frac{kT}{e} n_m(0) \left( -\frac{eV}{kT} + \frac{1}{2} \left[ \frac{eV}{kT} \right]^2 \right) + n_p(0) \left( \frac{V^2}{2E_p} - V \right) \right]. \end{aligned} \quad (A9)$$

Recalling that charge neutrality exists at the plasma-sheath boundary the equation

$$2n_{++}(0) + n_+(0) = n_m(0) + n_p(0) \quad , \quad (A10)$$

may be incorporated into Equation A9 to yield

$$\left(\frac{dV}{dx}\right)^2 \approx 8\pi e \left[ -\frac{n_{++}(0)}{2E_{++}} - \frac{n_+(0)}{4E_+} + \frac{n_m(0)e}{2k} + \frac{n_p(0)}{2E_p} \right] V^2. \quad (A11)$$

In order for  $\frac{dV}{dx}$  to be real, one must require

$$\frac{n_m(0)}{n_+(0)} \left( \frac{e}{kT} \right) + \frac{n_p(0)}{n_+(0)} \left( \frac{1}{E_p} \right) \geq \frac{n_{++}(0)}{n_+(0)} \left( \frac{1}{E_{++}} \right) + \frac{1}{2E_+} \quad (A12)$$

The second term of Equation A12 is of order  $[0.1 e/kT]$  since  $E_p \gg e/kT$  and this term may therefore be neglected. For sufficiently small double ion fractions the third term is also small and one obtains from Equation A12 the required energy of the single ions

$$E_+ \geq \left( \frac{kT}{2e} \right) \left( \frac{n_+(0)}{n_m(0)} \right) \approx \left( \frac{kT}{2e} \right) \left( \frac{n_p(0) + n_m(0)}{n_m(0)} \right). \quad (A13)$$

This is the same as the result obtained by Masek for no double ions, and it corresponds to an ion velocity of

$$v_+ \geq \sqrt{\frac{kT}{m_+} \left( \frac{n_p(0) + n_m(0)}{n_m(0)} \right)}. \quad (A14)$$

How small the ratio  $n_{++}(0)/n_+(0)$  must be is determined by the magnitude

of  $E_{++}/E_+$ . In order to determine the magnitude of this ratio consider  $n_+(0)$  small compared to  $n_{++}(0)$  in Equation A11 and the criterion becomes

$$E_{++} \geq \frac{n_{++}(0)}{n_m(0)} \left( \frac{kT}{e} \right) \quad (A15)$$

Since  $n_{++}(0) = \frac{n_p(0) + n_m(0)}{2}$  for charge neutrality at the interface the condition becomes

$$E_{++} \geq \left( \frac{kT}{2e} \right) \left( \frac{n_p(0) + n_m(0)}{n_m(0)} \right) \quad (A16)$$

Equations A13 and A16 taken together suggest  $E_{++}/E_+$  is of order unity and therefore that the third term of Equation A12 could be neglected until the  $n_{++}(0)/n_+(0)$  reaches a value of the order of 10%.

Equation A16 which sets a limit on the doubly charged ion velocity to assure a stable sheath for the case of negligible single ion density yields a value of

$$\begin{aligned} v_{++} &\leq \sqrt{\left( \frac{2kT}{m_{++}} \right) \left( \frac{n_p(0) + n_m(0)}{n_m(0)} \right)} \\ &= \sqrt{2} v_+ \end{aligned} \quad (A17)$$

REFERENCES

1. Byers, D. C. and J. F. Staggs, "SERT II Flight-Type Thruster System Performance," AIAA Paper No. 69-235, March 3-5, 1969.
2. Wilbur, P. J., "Experimental Investigation of a Throtttable 15 cm Hollow Cathode Ion Thruster," CR-121038, December 1972, NASA.
3. Rawlin, V. K., "Studies of Dished Accelerator Grids for 30-cm Ion Thrusters," AIAA Paper No. 73-1086, October 31 - November 2, 1973.
4. Kaufman, H. R., "Ion-Thruster Propellant Utilization," NASA TN D-6591, December 1971.
5. Harbour, P. J. et al, "Physical Processes Affecting the Design and Performance of Ion Thrusters with Particular Reference to the 10-cm, RAE/Culham T4 Thruster," AIAA Paper No. 73-1112, Oct. 31 - Nov. 2, 1973.
6. Wilbur, P. J., "An Experimental Investigation of a Hollow Cathode Discharge," NASA CR-120847, December 1971.
7. Strickfaden, W. B. and Geiler, K. L., "Probe Measurements of the Discharge in an Operating Electron Bombardment Engine," AIAA Journal, Vol. 1, No. 8, p. 1815, August 1963.
8. Free, B. A., "Economic Tradeoff Studies for Electric Propulsion Missions on Communications Satellites," AIAA Paper No. 71-683, June 14-18, 1971.
9. Wintucky, E. G., "High Voltage Ignition of Mercury Discharge Hollow Cathodes," AIAA Paper No. 73-1140, Oct. 31-Nov. 2, 1973.
10. Wilbur, P. J., "Correlation of Ion and Beam Current Densities in Kaufman Thrusters," Journal of Spacecraft and Rockets, Vol. 10, No. 9, September 1973, pp. 623-624.
11. Knauer, W., R. L. Poeschel, and J. W. Ward, "The Radial Field Kaufman Thruster," Journal of Spacecraft and Rockets, Vol. 7, No. 3, March 1970, pp. 248-251.
12. King, H. J., et al, "2½ KW Low Specific Impulse, Hollow Cathode Mercury Thruster," AIAA Paper No. 69-300, March 3-5, 1969.
13. Wilbur, P. J., "Performance of a 15 cm Ion Thruster with Dished Grids," Proceedings of Conference on Electric Propulsion of Space Vehicles held at Abingdon, Berks, England, April 10-12, 1973.
14. Poeschel, R. L. and W. Knauer, "A Variable Magnetic Baffle for Hollow Cathode Thrusters," AIAA Paper No. 70-175, Jan. 19-20, 1970.

15. Massey, H., and E. Burhop, Electronics and Ionic Impact Phenomena, The Clarendon Press, Oxford, 1969.
16. Biondi, M., Phys. Rev., 88, p. 660 1952.
17. Maier-Leibnitz, Z., Physik, 95, p. 499, 1936.
18. Schulz, G., and R. Fox, Phys. Rev., 106, p. 1179, 1957.
19. Fleming and Higginson, Proc. Phys. Soc., 84, p. 531, 1964.
20. Holt, H. and R. Krotkov, Phys. Rev., 144, p. 82, 1966.
21. Vincenti, W., and C. Kruger, Introduction to Physical Gas Dynamics, John Wiley and Sons, Inc., N. Y. 1965.
22. Allison, D. C., et al, Proc. Phy. Soc., 89, pt. 1, p. 41-4, 1966.
23. Hurt, W., J. Chem. Phys., 45, p. 2713-4, 1966.
24. Loeb, L., Basic Processes of Gaseous Electronics, U. of Calif. Press, L. A., 1961.
25. Bates, D., K. Bell, and A. Kingston, Proc. Phy. Soc., 91, p. 280, 1967.
26. Bleakney, W., "Probability and Critical Potentials for the Formation of Multiply Charged Ions in Mercury Vapor by Electron Impact," Phys. Rev. 35, pp. 139-148, January 1930.
27. Milder, N. L. and J. S. Sovey, "Characteristics of the Optical Radiation from Kaufman Thrusters," NASA TN D-6567, November 1971.
28. Pawlik, E. V., et al, "Ion Thruster Performance Calibration," AIAA Paper No. 72-475, April 1972.
29. Holt, E. H. and R. E. Haskell, Foundations of Plasma Dynamics, The Macmillan Company, New York, 1965.
30. Masek, T. D., "Plasma Properties and Performance of Mercury Ion Thrusters," AIAA Paper No. 69-256, March 3-5, 1969.
31. Brode, Robert B., "The Quantitative Study of the Collisions of Electrons with Atoms," Rev. Modern Physics, Vol. 5, No. 4, Oct. 1933, pp. 257-279.
32. Harrison, Harry, "The Experimental Determination of Ionization Cross Sections of Gases under Electron Impact," Catholic University Press, 1956.
33. Kupriyanov, S. E. and Z. Z. Latypov, "Ionization of Positive Ions by Electrons," J. Exptl. Theo. Physics (U.S.S.R.), V. 45, 815-816, September 1963.

34. Latypov, Z. Z., S. E. Kupriyanov, and N. N. Tunitskii, "Ionizing Collisions of Electrons with Ions and Atoms," J. Exptl. Theo. Physics (U.S.S.R.), V. 46, pp. 833-834, March 1964.
35. Laub, J. H., "An Electric Flow Meter," Electrical Engineering, V. 66, No. 12, p. 1216, December 1947.
36. Bohm, D., "Minimum Ionic Kinetic Energy for a Stable Sheath," The Characteristics of Electrical Discharges in Magnetic Fields, A. Guthrie and R. K. Wakerling, eds., McGraw-Hill Books Co., Inc., 1949, pp. 77-86.

*DO NOT PRINT*

DISTRIBUTION LIST

	Number of Copies
National Aeronautics and Space Administration Washington, D. C. 20546 Attn: RPE/Mr. James Lazar Mr. Daniel H. Herman, Code SL	1 1
National Aeronautics and Space Administration Lewis Research Center 21000 Brookpark Road Cleveland, Ohio 44135 Attn: Research Support Procurement Section W. E. Park, MS 500-312 Technology Utilization Office, MS 3-19 Report Control Office, MS 5-5 Library, MS 60-3 N. T. Musial, MS 500-113 Spacecraft Technology Division, MS 54-1 Mr. W. Plohr Mr. E. Davison Mr. R. Finke Mr. D. Byers Mr. B. Banks Mr. P. Thollot Mr. W. Kerslake Electromagnetic Propulsion Division, MS 301-1 Mr. W. E. Moeckel Dr. H. R. Kaufman	1 1 1 2 1 1 1 1 1 1 1 10 1 1
National Aeronautics and Space Administration Marshall Space Flight Center Huntsville, Alabama 35812 Attn: Mr. Ernst Stuhlinger (M-RP-DIR) Mr. C. H. Guttman	1 1
Research and Technology Division Wright-Patterson AFB, Ohio 45433 Attn: (APIE-2) R. Johnson (ADTN) Lt. David A. Fromme	1 1
National Aeronautics and Space Administration Scientific and Technical Information Facility P. O. Box 33 College Park, Maryland 20740 Attention: NASA Representative RQT-2448	10